40 CFR Part 191
Subparts B and C
Compliance Recertification Application 2026
for the
Waste Isolation Pilot Plant

Appendix TFIELD-2026
Transmissivity Fields

United States Department of Energy
Waste Isolation Pilot Plant

Carlsbad Field Office
Carlsbad, New Mexico

Compliance Recertification Application 2026
Appendix TFIELD-2026

TABLE OF CONTENTS

TFIELD-1.0 Introduction 0

TFIELD-2.0 Background and Hydrogeologic Data 0

TFIELD-2.1 Culebra Hydrogeologic Setting 1
TFIELD-2.2 Geologic Boundaries 2
TFIELD-2.2.1 Rustler Halite Margins 3
TFIELD-2.2.2 Salado Dissolution 8
TFIELD-2.3 Confinement and Recharge in the Culebra 8
TFIELD-2.3.1 Surface Drainage Basins 8
TFIELD-2.3.2 Culebra Confinement 9
TFIELD-2.4 Hydrogeologic Summary 11

TFIELD-3.0 T-Field Conceptual Model Refinement 12

TFIELD-4.0 Base T-Field Construction 12

TFIELD-5.0 T-Field Calibration 12

TFIELD-5.1 Model Calibration Targets 15
TFIELD-5.1.1 WIPP Testing Model Calibration Targets 15
TFIELD-5.1.2 Evaluation of Mills Ranch Pumping Response and Pumping Calibration 17
TFIELD-5.1.3 Single-Well Formation Performance Measurements of Transmissivity 23
TFIELD-5.2 Calibration Setup and Configuration 25
TFIELD-5.2.1 Selection of Pilot Point Locations 25
TFIELD-5.2.2 Creation of Parameter Zones 26
TFIELD-5.2.3 Transmissivity Parameters 26
TFIELD-5.2.4 Storativity Parameters 30
TFIELD-5.2.5 Horizontal Anisotropy Parameters 33
TFIELD-5.2.6 Spatial Distribution of Recharge 34
TFIELD-5.2.7 Estimated Mills Ranch Pumping Rates 34
TFIELD-5.2.8 Model Initial and Boundary Conditions 36
TFIELD-5.2.9 Observations and Residuals 38
TFIELD-5.2.10 MODFLOW Numerical Model 38
TFIELD-5.3 Calibration Process 39

TFIELD-5.3.1 Selection of Best-Calibrated Fields....43
TFIELD-5.4 Calibrated Results....45
TFIELD-5.4.1 Steady-state Freshwater Heads....46
TFIELD-5.4.2 Simulated Multi-Well Pumping Tests....47
TFIELD-5.4.3 Simulated Mills Ranch Pumping Event....48
TFIELD-5.4.4 Final Transmissivity Fields....49
TFIELD-5.4.5 Final Storativity Values....55
TFIELD-5.4.6 Final Anisotropy Ratios....57
TFIELD-5.4.7 Final Recharge Values....59
TFIELD-5.4.8 Model Diagnostics....60
TFIELD-6.0 TFIELD Summary....62
TFIELD-7.0 References....63

LIST OF TABLES

Table TFIELD-1. Freshwater Head Observations Used as Steady-state Calibration Targets....16
Table TFIELD-2. Summary of Transient Pumping Test Observations Used as Calibration Targets....17
Table TFIELD-3. Wells with Drawdown Observations Impacted by Mills Ranch Pumping....19
Table TFIELD-4. Variogram Parameters for the Grid-Scale....26
Table TFIELD-5. Variogram Parameters for Pilot Point Multipliers....27
Table TFIELD-6. Summary Table of Hydraulic Conductivity Parameterization....29
Table TFIELD-7. Summary of Specific Storage Parameters Used in the Model (lower and upper limits define the range of plausible values)....32
Table TFIELD-8. Summary Table of Anisotropy Parameters....33
Table TFIELD-9. Summary Table of Recharge Parameters....36
Table TFIELD-10. Coefficients derived by fitting the multivariate equation (Equation TFIELD.10) to the observed hydraulic heads and to assign Boundary Conditions....38
Table TFIELD-11. 100 Selected T-Field Realizations....44

LIST OF FIGURES

Figure TFIELD-1. Generalized Stratigraphy Near the WIPP 2
Figure TFIELD-2. Conceptual Model of the WIPP Culebra Dolomite. Transmissivity Decreases Eastward with Increasing Overburden and Halite and Increases Westward due to Fracturing from Salado Dissolution. Halite is Present Above (H-3) and Below (H-2) the Culebra in the East (Hart, 2008 modified from Beauheim and Holt, 1990; Holt, 1997). 3
Figure TFIELD-3. Rustler Formation Stratigraphic Nomenclature 4
Figure TFIELD-4. Rustler Halite Margins 6
Figure TFIELD-5. Top Elevation (m Above Mean Sea Level [AMSL]) of the Culebra. WIPP LWB Indicated with Blue Dashed Line. Township (T) and Range (R) Corners Indicated with Crosses. 7
Figure TFIELD-6. Closed Drainage Sub-basins Identified in Southeastern Nash Draw. White Areas are Either Outside Nash Draw or the Study Area (modified from Powers 2006). 9
Figure TFIELD-7. Culebra Confinement Map for Southern Nash Draw Study Area. White Areas are Outside the Nash Draw Geologic Study Area by Powers (2006). 11
Figure TFIELD-8. Flow Chart of Calibration Workflow 15
Figure TFIELD-9. Location of Mills Ranch Culebra Well and Neighboring Culebra Wells 18
Figure TFIELD-10. Drawdown Observations in Well SNL-17 and Pumping Periods Selected for the Mills Ranch Pumping Well (Vertical Bars). The Pink Fraction of the Bar Represents the Estimated Relative Pumping Rate. 20
Figure TFIELD-11. A Generalized Pumping in Recovery Curve from Trabucchi et al. (2018). The Left Graph Displays Residual Drawdown, s_R, used in Theis Recovery Method and Agarwal's Drawdown, s_A. 20
Figure TFIELD-12. Recovery Data for Ten Wells from the Culebra Monitoring Network Located Near Mills Ranch Well (Kuhlman and Corbet, 2017). The Inset Figure shows the Spatial Location of the Mills Ranch Well (Blue Star) and Culebra Monitoring Network Wells (Colored Circles). 21
Figure TFIELD-13. Distributions of Estimated Mills Ranch Pumping Rates for the 100 Selected Realizations 23
Figure TFIELD-14. Transmissivity Estimates from Single Well Hydraulic Tests 24
Figure TFIELD-15. Pilot Point Multiplier Locations. Pilot Point Multipliers were used Allow PEST to Explore Potential Uncertainty in Parameter Estimates Outside of Base T-field Spatial Patterns. 26
Figure TFIELD-16. Transmissivity Zone Map 29
Figure TFIELD-17. Spatial Distribution of Storativity Zones. Zone 0 is Confined; Zone 1 is a Transition Between Confined and Unconfined; Zone 2 is Unconfined; Zone 3 is Constant Head; Zone 4 is Inactive. 32
Figure TFIELD-18. Recharge Zones. Zone 1 consists of grid cells that intersect the Linear Feature Directed Southeast from the Center of the West Edge of the Model Domain. Zone 0 has No Recharge. 35

Figure TFIELD-19. Culebra Model Domain Showing Constant-Head Boundaries (Green Lines) and Initial Hydraulic Heads used in the Model Calibration. Hydraulic Heads are Assumed to Represent Steady-State Conditions during the Calibration. Red Numbers are Observed Hydraulic Heads. 37
Figure TFIELD-20. Evolution of the Total Objective Function with IES Iteration for 973 Calibrations 41
Figure TFIELD-21. Evolution of the Objective Function with IES Iteration for the Steady-state Freshwater Heads Observation Group for 973 Calibrations 42
Figure TFIELD-22. Evolution of the Total Objective Function with IES Iteration for the Multi-Well Pumping Tests for 973 Calibrations 43
Figure TFIELD-23. Normalized Objective Function for 973 Observation Groups at Iteration 5 44
Figure TFIELD-24. Histograms and Scatter Plots of the Normalized Objective Function for Primary Observation Groups. Gray symbols are All Calibrated Realizations Plotted in Normalized Objective-Function Space, the Blue Symbols are the 100 Realizations Closest to (0,0,0), i.e., the Best Fit Across All Three Observation Groups, and the Red Symbol is the Origin, Representing the Ideal Perfect Fit. 45
Figure TFIELD-25. Contour of Median Simulated Steady-state Freshwater Head (m-AMSL) in Black (5-m contour interval). Contours are Generated by Linear Interpolation Using Simulated Heads from the MF6 Regular Grid. Mean, Median, or Mode (Depending on Distribution) of Observed Steady-state Freshwater Heads for Each Well are in Red. 47
Figure TFIELD-26. Distributions of Estimated Mills Ranch Pumping Rates for each pumping Interval Across the 100 Selected Realizations, shown as Violin Plots. The Width of Each Violin Represents the Duration of the Pumping Interval, and the Vertical Spread Indicates the Variability in Estimated Pumping Rates (gpm). 49
Figure TFIELD-27. Mean Transmissivity for 100 Selected Realizations at Calibration Iteration 5 50
Figure TFIELD-28. Standard Deviation of Transmissivity Across 100 Selected Realizations at Calibration Iteration 5 51
Figure TFIELD-29. Count of High-T Zone Membership at Calibration Iteration 0 (prior) 52
Figure TFIELD-30. Count of High-T Zone Membership at Calibration Iteration 5 53
Figure TFIELD-31. Count of T Fields with Change from Low-T to High-T Between Calibration Iterations 0 to 5 54
Figure TFIELD-32. Count of T Fields with Change from High-T to Low-T Between Calibration Iterations 0 to 5 55
Figure TFIELD-33. Mean Storativity Values Across 100 Selected Realizations at Iteration 5 56
Figure TFIELD-34. Standard Deviation of Storativity Values Across 100 Selected Realizations at Iteration 5 57
Figure TFIELD-35. Mean Anisotropy Values Across 100 Selected Realizations at Iteration 5 58

Figure TFIELD-36. Standard Deviation of Anisotropy Values Across 100 Selected Realizations at Iteration 5 59
Figure TFIELD-37. Maximum Recharge (Left) and Standard Deviation (Right) Across 100 Selected Realizations at Iteration 5 60
Figure TFIELD-38. Distributions of Observed and Model-Predicted Steady-state Freshwater Heads in H-19b0 for 100 Realizations at Iteration 5 61
Figure TFIELD-39. Observed vs Simulated Drawdown at SNL-14 and H-19b0 Monitoring Locations for the SNL-14 Multi-Well Pumping Test 61
Figure TFIELD-40. Distribution of Single-Well Pumping Test Transmissivity Values in Model Element Containing H-19b0 for 100 Selected Realizations from Iteration 5 62

ACRONYMS AND ABBREVIATIONS

A	transmissivity anisotropy [dimensionless]
AMSL	above mean sea level
AP	analysis plan
CFR	Code of Federal Regulations
CRA	Compliance Recertification Application
D	diffusivity [m^2/s]
DOE	U.S. Department of Energy
EPA	U.S. Environmental Protection Agency
GLMA	Gauss-Levenburg-Marquardt algorithm
gpm	gallons per minute
IMS	Iterative Model Solution
K	hydraulic conductivity (m/s)
km	kilometer
LWB	Land Withdrawal Boundary
m	meter
m^2	square meters
M/H	mudstone/halite margin
m^2/s	square meters per second
m^3/s	cubic meters per second
m/yr	meters per year
MF6	MODFLOW 6.2
PA	performance assessment
PABC	performance assessment baseline calculation
R	recharge [m/s]
S	storativity [dimensionless]
S_s	specific storage (1/m)
SNL	Sandia National Laboratories
SSE	sum of squared errors
T	transmissivity [m^2/s]
T-fields	transmissivity fields (T, A, R, and S)
USGS	U.S. Geological Survey
UTM	Universal Transverse Mercator map projection
WIPP	Waste Isolation Pilot Plant

TFIELD-1.0 Introduction

This Appendix presents the process used to develop and calibrate the input parameter fields for the Culebra flow model. Modeling the transport of radionuclides through the Culebra Dolomite Member of the Rustler Formation (hereafter, the Culebra and the Rustler) is one component of the performance assessment (PA) conducted for the U.S. Department of Energy (DOE) Waste Isolation Pilot Plant (WIPP) Compliance Recertification Application (CRA). Transport modeling in PA requires Darcy velocities, which are generated by the Culebra groundwater flow model. Calibrated model parameters are collectively referred to as "T-fields" (transmissivity fields) but include spatially variable calibrated fields of transmissivity (*T*), storativity (*S*), anisotropy (*A*), and recharge (*R*). This appendix describes the process followed for generating T-fields for CRA-2026.

T-field development begins with the assembly of information germane to geologic and hydrologic factors potentially affecting Culebra *T* (Section TFIELD-2.0). A two-part approach was used to generate base T-fields. In the first part (Section TFIELD-3.0), a conceptual model for geologic controls on Culebra *T* was formalized and the hypothesized geologic controls were regressed against Culebra *T* estimates at monitoring wells to determine linear regression coefficients. In the second part (Section TFIELD-4.0), a method was developed for applying the linear regression model to predict Culebra *T* across the WIPP model area between the sparse observations at wells. The generation of base T-fields described in these two sections was accomplished by Hart et al. (2008). The data and approach for Sections 2.0 through 4.0 were unchanged for the calibration of the T-fields described in this Appendix.

For CRA-2026, the 1,000 base T-fields were calibrated following the process outlined in Section TFIELD-5.0, with the 100 best calibrated T-fields selected for use in PA radionuclide transport calculations, best being qualified as those fields with minimal modeled flow difference compared to measured water level and pumping test observations. Section TFIELD 5.0 summarizes the modeling assumptions, initial and boundary conditions, discretization approach, observation weighting, and application of PEST++ IES, hereafter PEST (White et al. 2020). These components were implemented in MODFLOW 6.2.2, hereafter MF6, to calibrate the T-fields through a pilot point method.

TFIELD-2.0 Background and Hydrogeologic Data

The WIPP is a deep geological repository for the disposal of defense-related transuranic (TRU) radioactive waste. Per EPA regulation 40 CFR 191, PA analysis shall estimate the cumulative releases of radionuclides, considering the associated uncertainties, caused by all significant processes and events. Among those events, a potential impact of the repository by a drilling event resulting in radionuclide release is of interest with respect to repository compliance to the environmental radiation protection standards.

The Culebra Dolomite has been identified as the most transmissive pathway for potential radionuclide release above the WIPP site. To adequately model the Culebra for PA, geologic

uncertainty needs to be quantified and incorporated into a flow modeled to describe release pathways. T-fields are used to represent this uncertainty by generating heterogenous representations of Culebra transmissivity constrained by measured geologic and hydrologic data. The objective of this section is to present relevant hydrogeologic data that translates to the Culebra model.

TFIELD-2.1 Culebra Hydrogeologic Setting

The Culebra Member is considered as a potential long-term release pathway in WIPP PA because it is the most permeable laterally continuous geologic unit above the repository level (see Figure TFIELD-1 for general stratigraphy). Disturbed repository performance scenarios (as described in Appendix PA, Section-2.2.2.2) describe the potential connection of the repository with the Culebra, transporting radionuclides to the accessible environment under natural flow conditions. As defined by 40 CFR 191.12, “accessible environment” includes (1) the atmosphere, (2) land surfaces, (3) surface waters, (4) oceans, and (5) all of the lithosphere beyond the controlled area. In the context of this appendix, the relevant portion of the accessible environment is the Culebra beyond the Land Withdrawal Boundary (LWB).

Groundwater flow and radionuclide transport in the Culebra are influenced by both depositional and post depositional processes. Although the Culebra was likely deposited uniformly over a wide area (Holt and Powers 1988), depositional variations include localized mudstone or halite layers within the Rustler Formation immediately above and below it. Post-depositional processes include the dissolution of halite from the underlying Salado Formation and precipitation of evaporates within the vugs and pores in the Culebra (see Figure TFIELD-2). Culebra T Decreases to the east (increasing overburden and halite) and increases to the west (fracturing due to underlying Salado dissolution). Halite appears both above (H-3) and below (H-2) the Culebra in the east. Primary groundwater flow direction through the Culebra is south.

Groundwater flow in the Culebra is generally from north to south at the WIPP site. Water levels in Culebra wells in Nash Draw respond more rapidly to precipitation and behave differently from Culebra wells in the immediate vicinity of the WIPP site due to the unconfined nature of the Culebra in portions of Nash Draw.

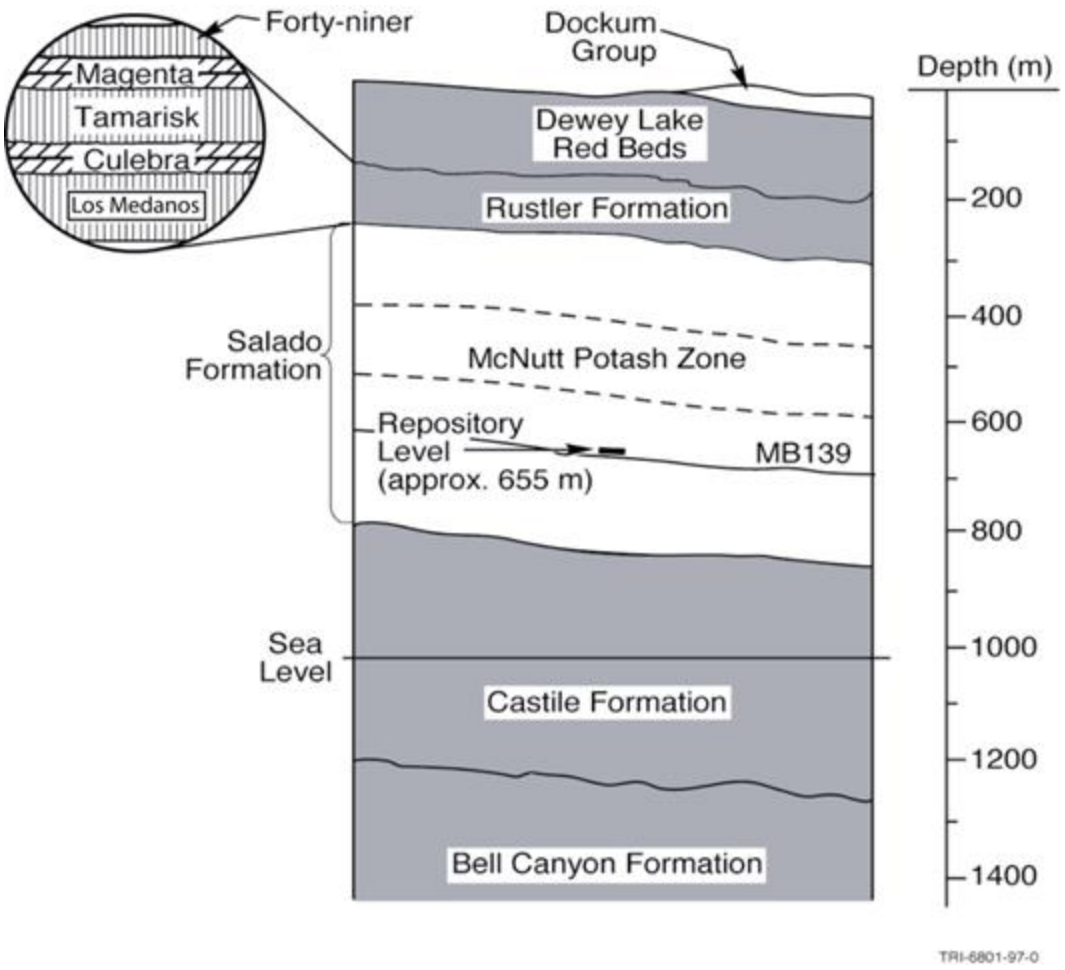


Figure TFIELD-1. Generalized Stratigraphy Near the WIPP

TFIELD-2.2 Geologic Boundaries

The locations of the Rustler halite margins (Section TFIELD-2.2.1) and the Salado dissolution margin (Section TFIELD-2.2.2) both affect the conceptual model of Culebra *T* (see Figure TFIELD-1 for general relationships between the Rustler, the Salado and the WIPP repository). The presence of halite in the non-dolomite members of the Rustler correlates strongly with estimates of Culebra *T*. Halite and anhydrite are found as pore-filling cements in the Culebra (reducing open fractures) when halite exists in layers above the Culebra, below the Culebra, or both. When halite is found either above (H3) or below (H2) the Culebra, observed Culebra *T* is low. When halite exists both above and below the Culebra, the observed Culebra *T* is extremely low.

North, south, and west of the WIPP site, Cenozoic dissolution has affected the upper Salado Formation. Where halite dissolution has occurred, the rocks overlying the Salado, including the Culebra, commonly show strain, enlarged fracture apertures, and evidence of fracturing collapse or brecciation (e.g., Beauheim and Holt 1990). All WIPP Culebra wells within the Salado

dissolution zone have been interpreted to have high *T* (Beauheim and Ruskauff, 1998; Mercer, 1983; Roberts, 2006; Roberts, 2007).

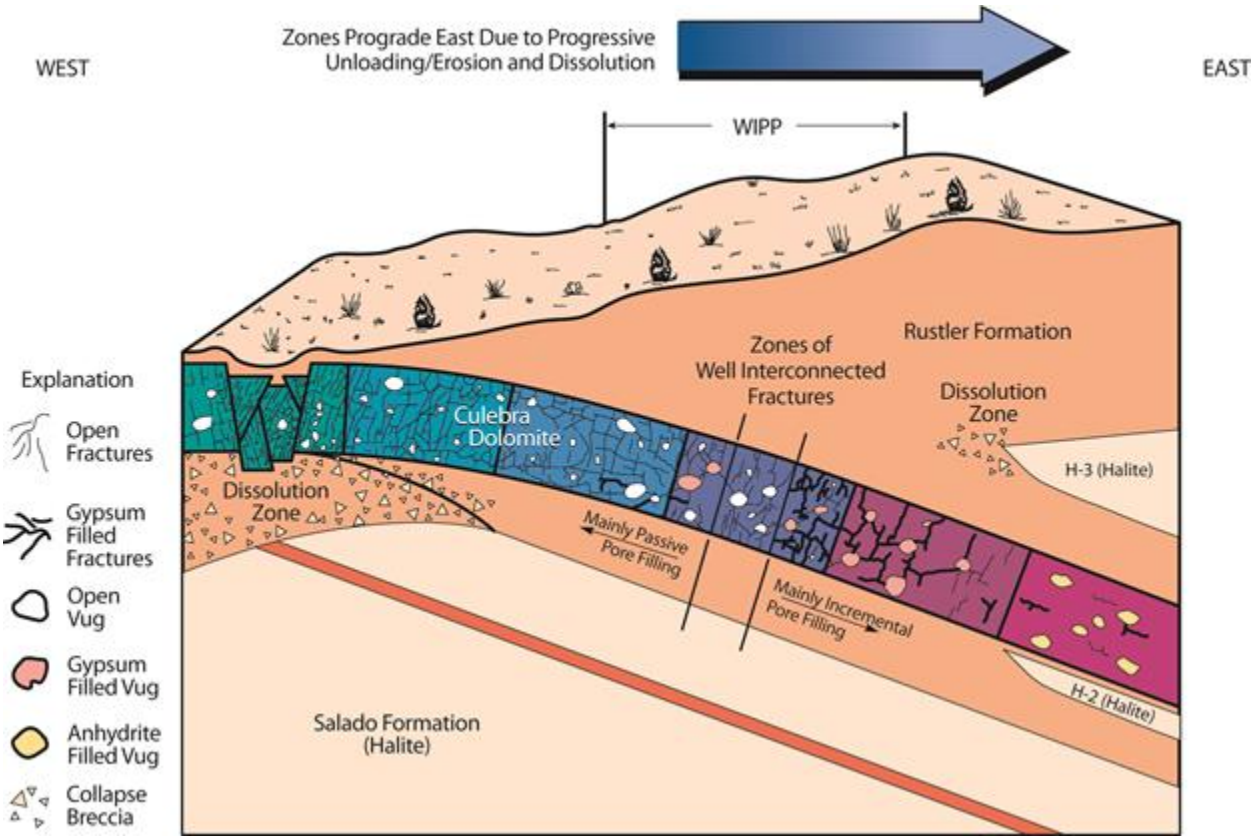


Figure TFIELD-2. Conceptual Model of the WIPP Culebra Dolomite. Transmissivity Decreases Eastward with Increasing Overburden and Halite and Increases Westward due to Fracturing from Salado Dissolution. Halite is Present Above (H-3) and Below (H-2) the Culebra in the East (Hart, 2008 modified from Beauheim and Holt, 1990; Holt, 1997).

TFIELD-2.2.1 Rustler Halite Margins

The generalized Rustler Formation stratigraphy depicted in Figure TFIELD-3 comprises two types of geologic variability. Vertical stratigraphy places older formations below younger formations at the same location in space (e.g., the Los Medaños Member is older than the Culebra Member), while facies change place two units of similar age at different spatial locations, due to changes in depositional environments (e.g., Mudstone 4 [M4] and Halite 4 [H4] of the Forty-niner Member are of the same age but occur in different locations).

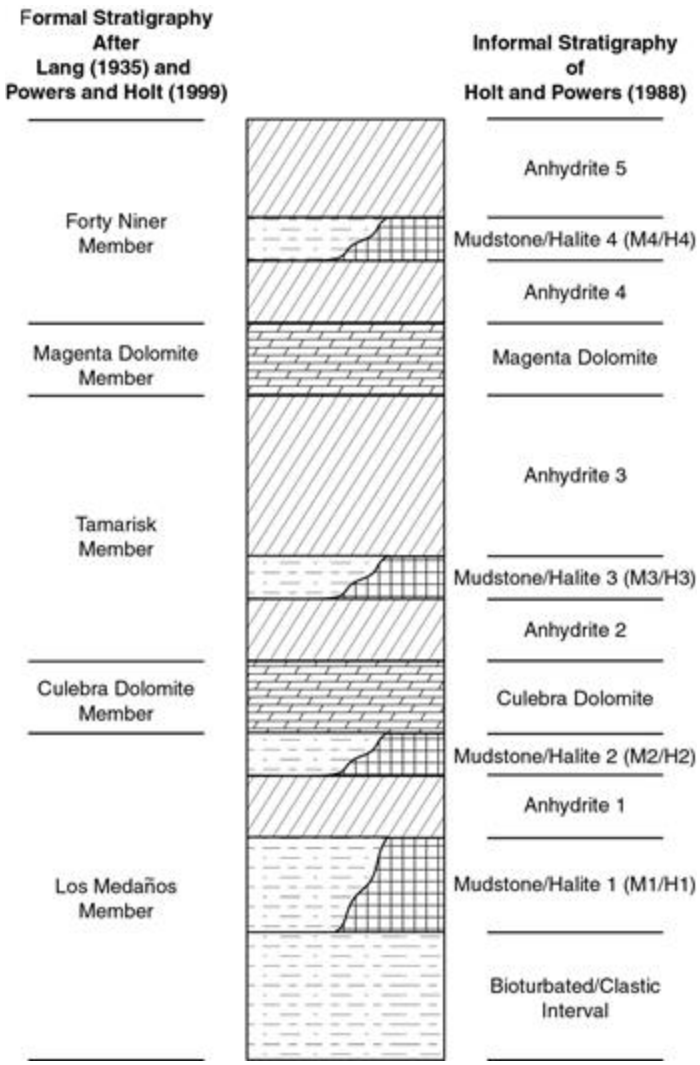
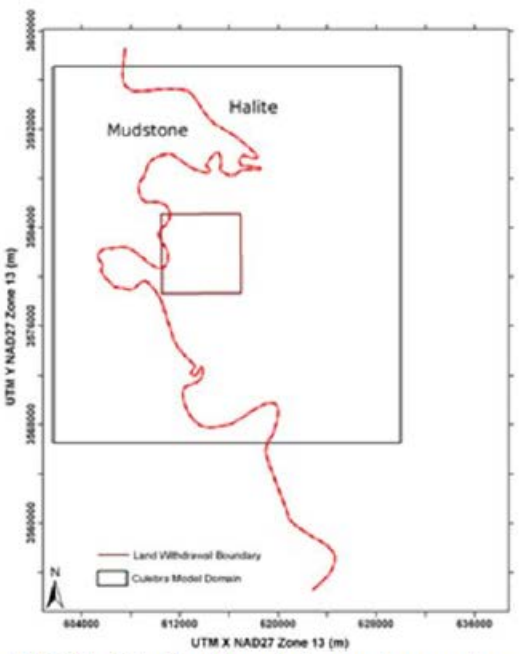


Figure TFIELD-3. Rustler Formation Stratigraphic Nomenclature

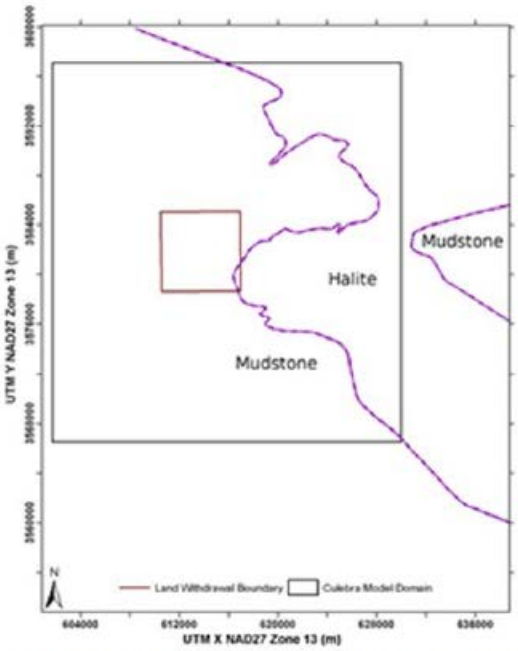
Powers (Powers 2002a and Powers 2002b) provided geologic data across the Culebra modeling domain that included maps of halite margins within the Rustler. Those margins were largely based on work by Powers and Holt (1995), supplemented by data collected from potash drillholes (Jones 1978). The observed distribution and thickness of halite in the Rustler is interpreted to reflect sedimentary structures and facies relationships established during deposition, rather than being the product dissolution alone (Holt and Powers 1988; Powers and Holt 1999; Powers and Holt 2000). Data collected during WIPP air-intake shaft geologic mapping provided the basis for the current facies-based conceptual model used at the WIPP (Holt and Powers 1988). Some minor zones adjacent to the depositional margins have been interpreted as having undergone some post-depositional dissolution of halite, specifically the halite in the Tamarisk Member, but the extent of this Rustler halite dissolution is relatively minor (Beauheim and Holt 1990).

The Rustler halite margins used in the Culebra model domain for the CRA-2026 PA are shown in Figure TFIELD-4. These margins have not changed since CRA-2019 and are identical to those defined by Powers (2007).

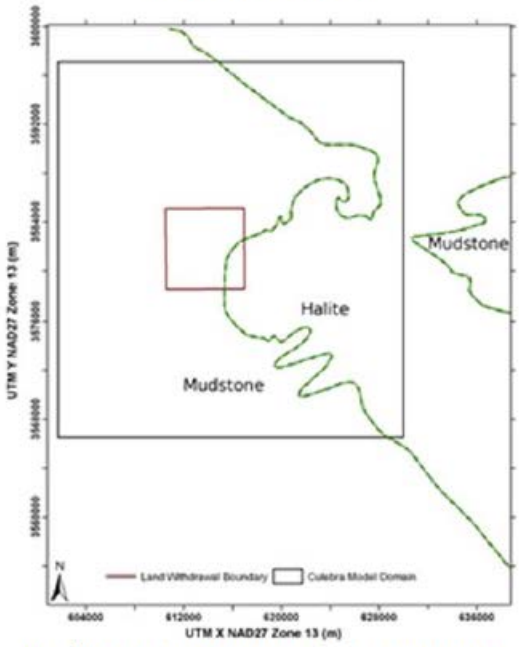
All mudstone/halite margins show similar trends (Figure TFIELD-4). Southeast of the WIPP, the margins are elongate roughly northwest to southeast. The gross trends of these margins are similar to the trend in the elevation of the top of Culebra (Figure TFIELD-5). The northwest-to-southeast trending anticlinal feature is called the Divide anticline (Holt and Powers 1988; Powers 2003). Mudstone dominates along this trend in three of the mudstone-halite units of the Rustler (i.e., all except M1/H1). Base T-field construction utilizes the mudstone/halite margins to as parameter boundaries. Similarly, T-field calibration utilizes these margins to differentiate regional-scale parameters.



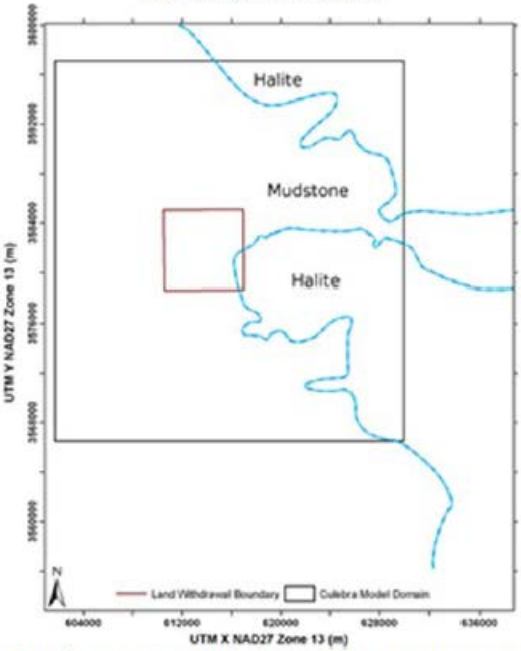
M-1/H-1 Halite Margin In the Lower Los Medaños Member



M-2/H-2 Halite Margin In the Upper Los Medaños Member



M-3/H-3 Halite Margin In the Tamarisk Member



M-4/H-4 Halite Margin In the Forty-niner Member

Figure TFIELD-4. Rustler Halite Margins

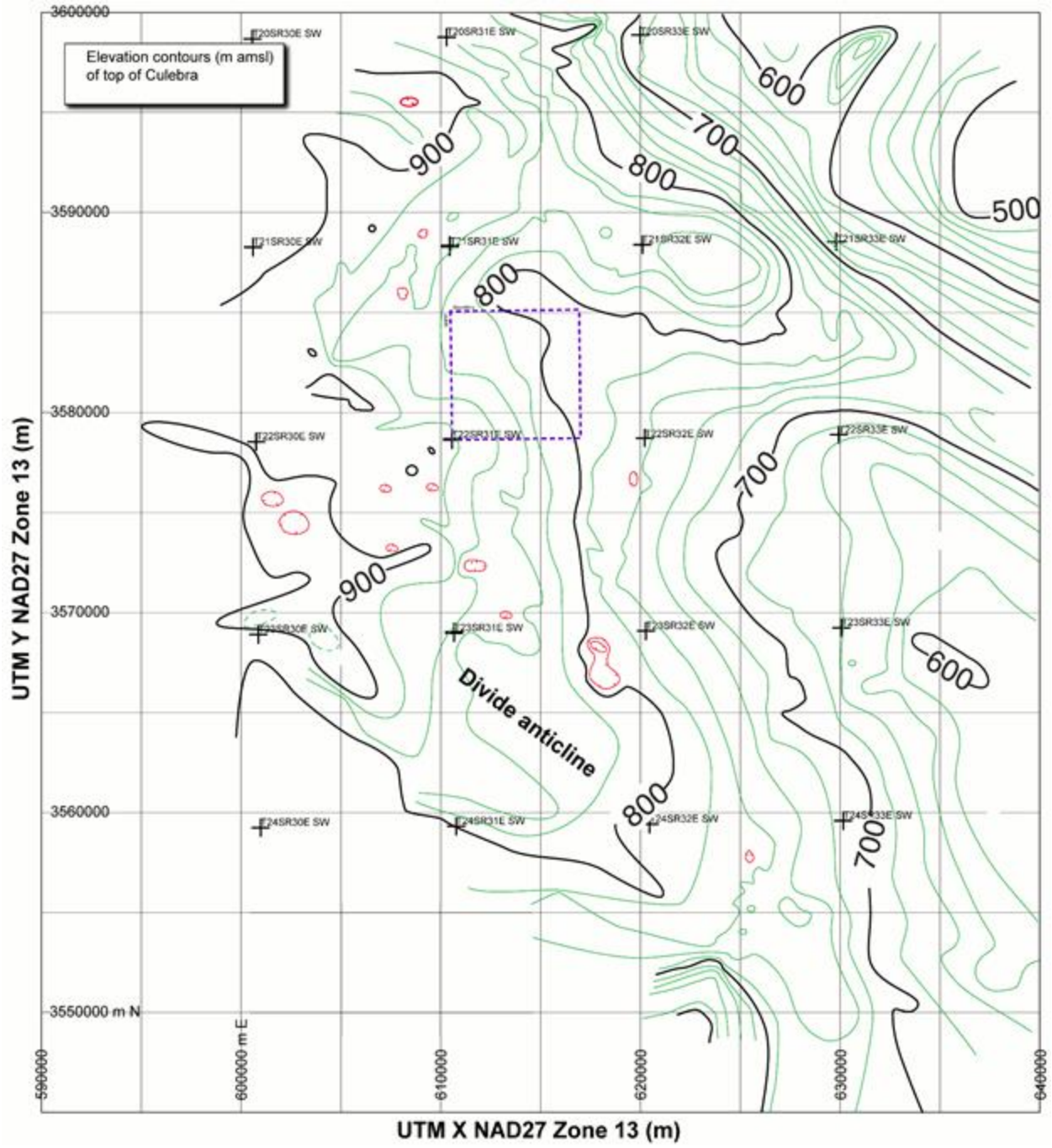


Figure TFIELD-5. Top Elevation (m Above Mean Sea Level [AMSL]) of the Culebra. WIPP LWB Indicated with Blue Dashed Line. Township (T) and Range (R) Corners Indicated with Crosses.

TFIELD-2.2.2 Salado Dissolution

A margin marking the lateral extent of dissolution of upper Salado Formation halite for was inferred from significant local changes in thickness of the interval between the Culebra and the Vaca Triste Sandstone Member of the Salado (Powers 2002a and Powers 2002b). Additional data were added south of the WIPP, with log cross sections, to delineate the margin more accurately (Powers 2003). These data are retained for CRA-2026, and the Salado dissolution line is applied to T-field calibration to differentiate regional-scale parameters.

TFIELD-2.3 Confinement and Recharge in the Culebra

The estimate of Culebra confinement is the most interpretive element for siting recharge. Powers (2006) identified drainage basins, channels, and sinkholes using surface topographic features identifiable from maps, aerial photos, and/or field reconnaissance. This work focused on locations south and west of the WIPP in the southeastern arm of Nash Draw and identified Culebra unconfined regions. The boundaries shown in Figures TFIELD-6 and TFIELD-7 that describe Culebra confinement and sub-basins associated with recharge correspond to the Culebra flow model domain in the west and south; the northern and eastern boundaries included the southeastern arm of Nash Draw and an area beyond the apparent eastern extent of the draw. The remaining portion of the Culebra flow model boundary were excluded from these graphics as the Powers (2006) study did not reach the other portions of the model domain. This section provides the geographic/geologic context to the location and position of recharge and confinement contained in the Culebra flow model.

TFIELD-2.3.1 Surface Drainage Basins

Drainage basin size and characteristics are important elements to determine how rainfall, infiltration, and runoff may contribute to recharge of near-surface Rustler hydrologic units in Nash Draw. Mapping the basins was the first step in understanding the complex geology and hydrology inside Nash Draw, which expresses itself as water-level fluctuations in some Culebra wells in and near Nash Draw.

Topographic maps, aerial photographs, and some field checking were used to define separate surface drainage basins displayed in Figure TFIELD-6; differing colors delineate the separate drainage basins (Powers 2006). The drainage basins are mainly separated by topographic divides and local lows or concentration points that can be distinguished on 7.5-minute quadrangle topographic maps. In Nash Draw's evaporite karst terrain (e.g., Powers and Owsley, 2003), collapse features, caves, and sinkholes can capture runoff, producing small internally drained basins nested within the larger watershed. These localized closed drainage basins in Nash Draw represent potential recharge locations for the Rustler. The description of these sub-basins link to the general location of recharge as applied to the Culebra flow model described in TFIELD-5.2.6.

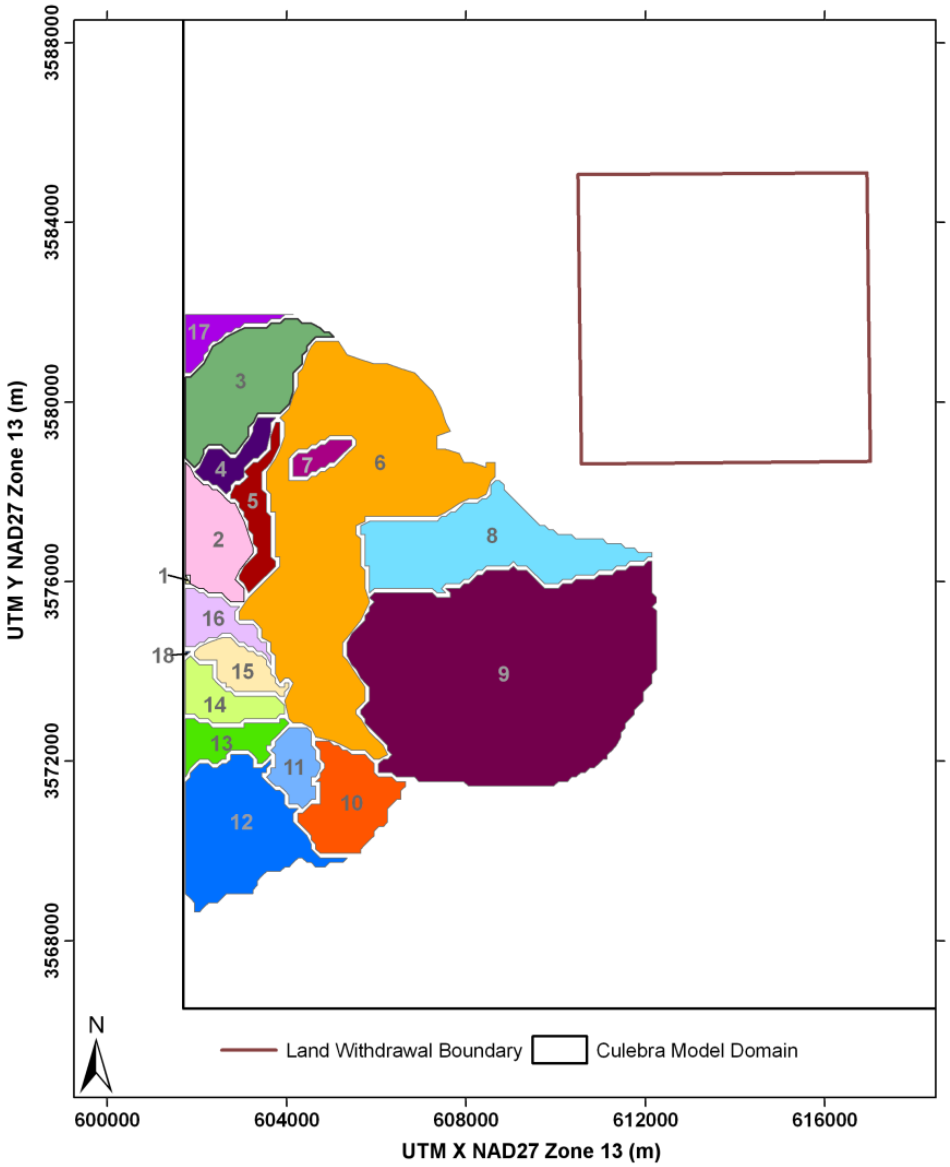


Figure TFIELD-6. Closed Drainage Sub-basins Identified in Southeastern Nash Draw. White Areas are Either Outside Nash Draw or the Study Area (modified from Powers 2006).

TFIELD-2.3.2 Culebra Confinement

Across the WIPP LWA, the Culebra can be considered confined, with little potential for direct vertical recharge for the relatively short time period covered in the WIPP Culebra model calibration (i.e., the length of multi-well pumping tests). The degree of confinement of the Culebra in the Powers (2006) study area was not directly determinable from the surface data. As a result, a variety of surface features and well data were combined to speculate areas where the Culebra is less confined compared to conditions at the WIPP site, where there are more well-test and drillhole data.

Within portions of Nash Draw, the Culebra is relatively shallow (i.e., only covered by portions of the highly fractured Tamarisk) and observed water levels show the Culebra responds to precipitation events on short time scales (1-2 days). Due to the interpretative nature of the confinement estimate, no numerical values of storativity were predicted from the Powers (2006) geologic analysis, only zones of relatively higher or lower confinement, with an intermediate transition zone. The confined area has a relatively unambiguous definition, whereas the boundary between transition and unconfined is much more subjective.

The area of the Culebra considered confined (red in Figure TFIELD-7) is defined by the interpreted margin of upper Salado halite dissolution (Powers et al. 2003). There is a significant increase in Culebra *T* values west and south of this margin (Powers 2006), and this change is attributed to changes in fracture aperture associated with strain induced by dissolution. Most of the Culebra unconfined zone (blue in Figure TFIELD-7) is in central Nash Draw. The strategy for estimating relative Culebra confinement was to select areas where the Culebra is known or believed to be very shallow (≤30 meters [m] below ground surface) and where observed recharge points (caves, sinkholes, alluvial dolines) are believed to access units below the Magenta. The transition zone (green in Figure TFIELD-7) includes areas where data from wells indicate there is some vertical isolation of the Culebra, but information is less conclusive. These confinement areas are expressed through specific storage parameters described in Section TFIELD-5.2.4.1.

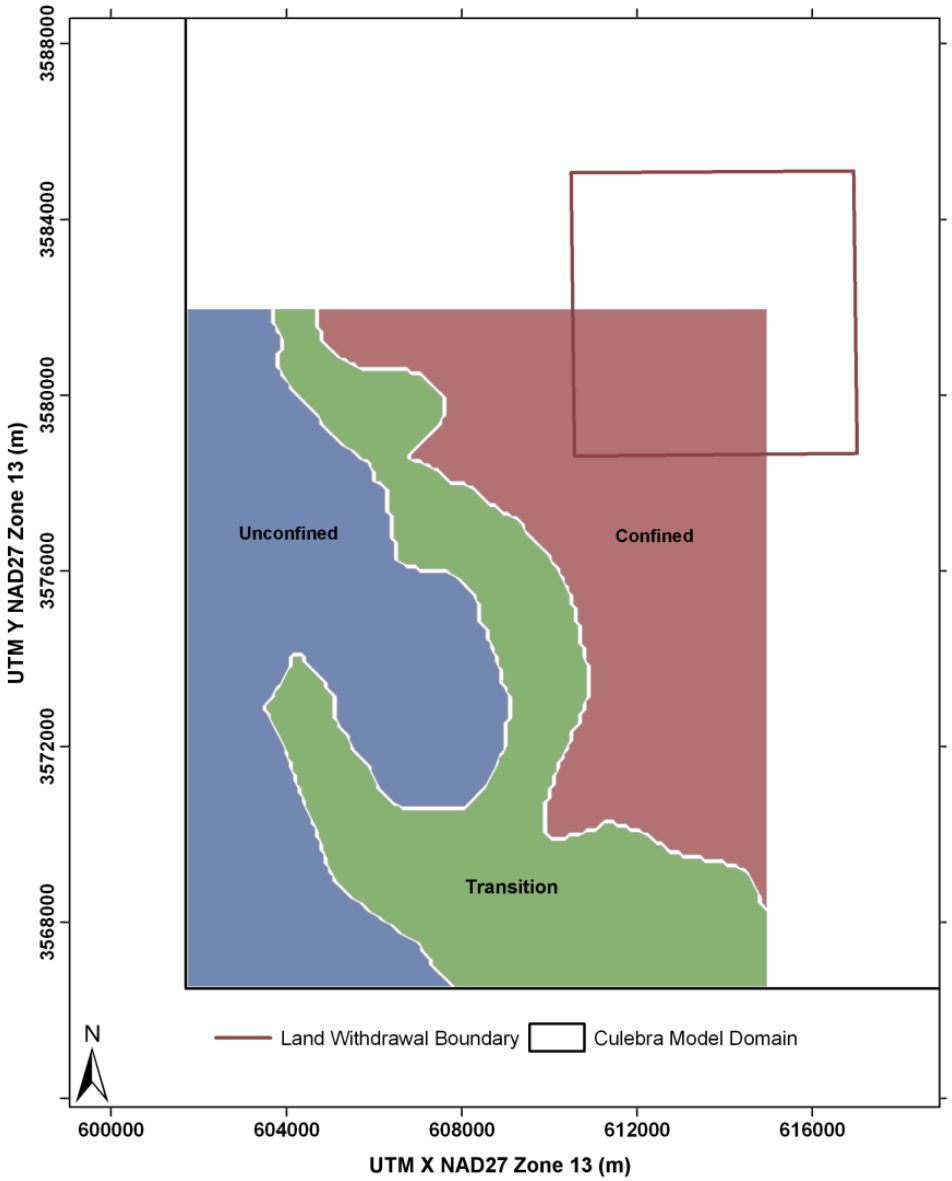


Figure TFIELD-7. Culebra Confinement Map for Southern Nash Draw Study Area. White Areas are Outside the Nash Draw Geologic Study Area by Powers (2006).

TFIELD-2.4 Hydrogeologic Summary

Geologic data used to inform the construction of base T-fields discussed in Section TFIELD-2.0 have remained unchanged from CRA-2014. The data hydrogeologic data presented here are meant to provide context to the following sections detailing the recalibration of T-fields. All data and the approach used to generate base T-fields are described in Title 40 CFR Part 191 Subparts B and C Compliance Recertification Application 2014 for the Waste Isolation Pilot Plant Appendix TFIELD-2014 Transmissivity Fields (DOE 2014).

TFIELD-3.0 T-Field Conceptual Model Refinement

The T-field conceptual model has not changed from CRA-2014 (DOE 2014).

TFIELD-4.0 Base T-Field Construction

The base T-fields utilized in the CRA-2009 Performance Assessment Baseline Calculation (PABC), were used, unchanged in CRA-2014. These same base T-fields have not changed but were recalibrated for CRA-2026.

TFIELD-5.0 T-Field Calibration

The work outlined in Section TFIELD-5.0 was performed under AP-203 (Bowman 2022). The T-field calibration process used the 1,000 calculated base T-fields from AP-114 (Hart et al. 2009) as inputs. Base T-field generation was accomplished through combined interpretations of Culebra transmissivity data in conjunction with conditional indicator simulations. Geologic and hydraulic information was used to create "soft data" that are used to define probabilities of low *T* values. Soft data include halite bounding, gypsum cements, and hydrologic diffusivity/connectivity. Conditional indicator simulations were created using the soft data combined with indicator variography of $\log_{10} T$ values from select wells. A regression model was constructed utilizing hydrologic and geologic indicators. Final base T-fields were then constructed using a combination of the Stochastic indicator results and regression coefficients.

The base T-fields that were calibrated using PEST are spatially variable fields of transmissivity (*T*) (represented in MF6 as hydraulic conductivity [*K*, m/sec] with formation thickness assumed constant), dimensionless horizontal anisotropy (*A*), storativity (*S*) (represented in MF6 as specific storage [S_s, 1/m] with formation thickness assumed constant), and vertical recharge (*R*, m/sec). The calibration of the T-fields employs a multi-scale parameterization approach that combines three spatial scale parameterizations (Bowman et al. 2023). These include a local-scale grid-based discretization (i.e., each 100-m model cell in the model domain), a medium-scale grid based on a uniform grid of pilot points (500-m grid), and a large-scale parametrization based on zonal multipliers that spanned large portions of the Culebra model domain. This approach allows the model to capture broad regional geological trends while still resolving highly localized flow pathways. The same transmissivity zones described in AP-114 were used in this task for transmissivity and anisotropy. Zones for storativity and recharge were updated for CRA-2026 based on other analyses completed in the area surrounding the WIPP site (Section TFIELD-5.2). Pilot points were selected for each parameter, and initial values were consistent with the conceptual model in AP-114 (Hart et al. 2008). A more in-depth technical description of Section TFIELD-5 of this report is given in Bowman et al. (2023).

Both steady-state and transient head calibration targets are discussed in Section TFIELD-5.1. The parameter zones, pilot point locations for each parameter, initial conditions, and boundary conditions are specified in Section TFIELD-5.2. The components of the MF6 model used as the forward model with PEST (the inverse model used to estimate the best-fit parameters), and the utilities required to pre-process and post-process the inputs and outputs from the model during

the calibration are discussed in Section TFIELD-5.3. Finally, some post-calibration analysis of the results is presented in Section TFIELD-5.4.

Additional calibration parameters beyond the T-fields include the two base pumping rates at the Mills Ranch well, which are further explained in Section TFIELD-5.1.2. Since the pumping rate for the Mills Ranch well is unknown, it was estimated in the calibration process as a multi-year transient event.

At the completion of each MF6 forward model (Langevin et al. 2017), simulated steady-state hydraulic heads and transient drawdowns were extracted for all observation locations. Extracted head values were compared against field measurements with differences calculated as residuals by PEST. The Jacobian matrix was then computed using finite difference perturbations of each adjustable parameter (Doherty 2025), providing sensitivity information to update parameter estimates inside the optimization routine. PEST iteratively minimizes the objective function (ϕ), defined as the weighted sum of squared residuals across all hydraulic head and drawdown observations, for successive iterations until reductions in ϕ are minimized. The ending of iterations indicates convergence between simulated and observed parameters.

The version of PEST (PEST++ IES) used to calibrate 2026 T-fields does not require the explicit construction of the Jacobian sensitivity matrix via finite differences. PEST instead utilizes the concept of a “prior ensemble” where the ensemble of realizations are calibrated simultaneously, and in each realization every parameter is defined probabilistically, using a gaussian distribution with a spatial correlation (White 2018). A single prior realization consists of parameter set sampled randomly from that set of prior parameter distributions. When a PEST optimization process is launched, the prior parameter ensemble is evaluated first by running each of the 1,000 forward model realizations and populating the prior observation file with the simulated values produced by each forward model run. This new optimization is contained within the internal PEST calculations, a change in the CRA-2026 calibrations since CRA-2014.

Previous versions of PEST, such as the one used in CRA-2014, required at least one forward model execution for each estimated parameter as part of the calibration. Subsequently the calibration process would have to be run multiple times on a field-by field, basis. Additionally, the number of parameter estimates (i.e. pilot points) were minimized to lower calibration run-times. The ensemble approach used by the new version of PEST allows for the calibration of a large number of parameters across the ensemble, shortening run times.

After each PEST iteration, the selected ensemble is used as the basis for another ensemble-based iteration. Each iteration generally continues to minimize the overall objective function, until no more progress is made, and the iteration process is stopped.

Two types of residuals were calculated. Actual residuals represent the direct differences between simulated and observed heads. Measured residuals incorporate both the observation noise and model-error components specified in the PEST configuration. PEST reports both the actual and measured objective function values ($\boldsymbol{\phi}$) at each iteration. However, PEST uses the

measured $\boldsymbol{\phi}$ as the criterion for assessing convergence and selecting the preferred parameter set for the ensemble. In this appendix the actual objective function ($\boldsymbol{\phi}$) is defined as

$$\boldsymbol{\phi} = \sum(\boldsymbol{r_i} \cdot \boldsymbol{w_i})^2 \qquad \text{Equation (TFIELD.1)}$$

where r_i is the actual residual for observation i and w_i is the corresponding observation weight.

Weights were constant throughout the PEST optimization process. During the PEST optimization process, the model parameters are adjusted such that the forward MF6 models (both steady-state and transient pumping tests) produce model outputs that best match historical observations.

The T-Field calibration process was performed under the project's quality-assurance run-control procedures, with all inputs and scripts maintained in a version control system on a central server (Bowman et al. 2023, Section 5.5). The calibrations required approximately two days of continuous run-time on a total of 200 processors (Intel(R) Xeon(R) Gold 6132 CPU @ 2.60GHz, Intel(R) Xeon(R) Gold 6148 CPU @ 2.40GHz) (see Section TFIELD-5.2), an approximate 99% decrease in run-time from the CRA-2014 calibrations. Figure TFIELD-8 summarizes the workflow of the calibration described above.

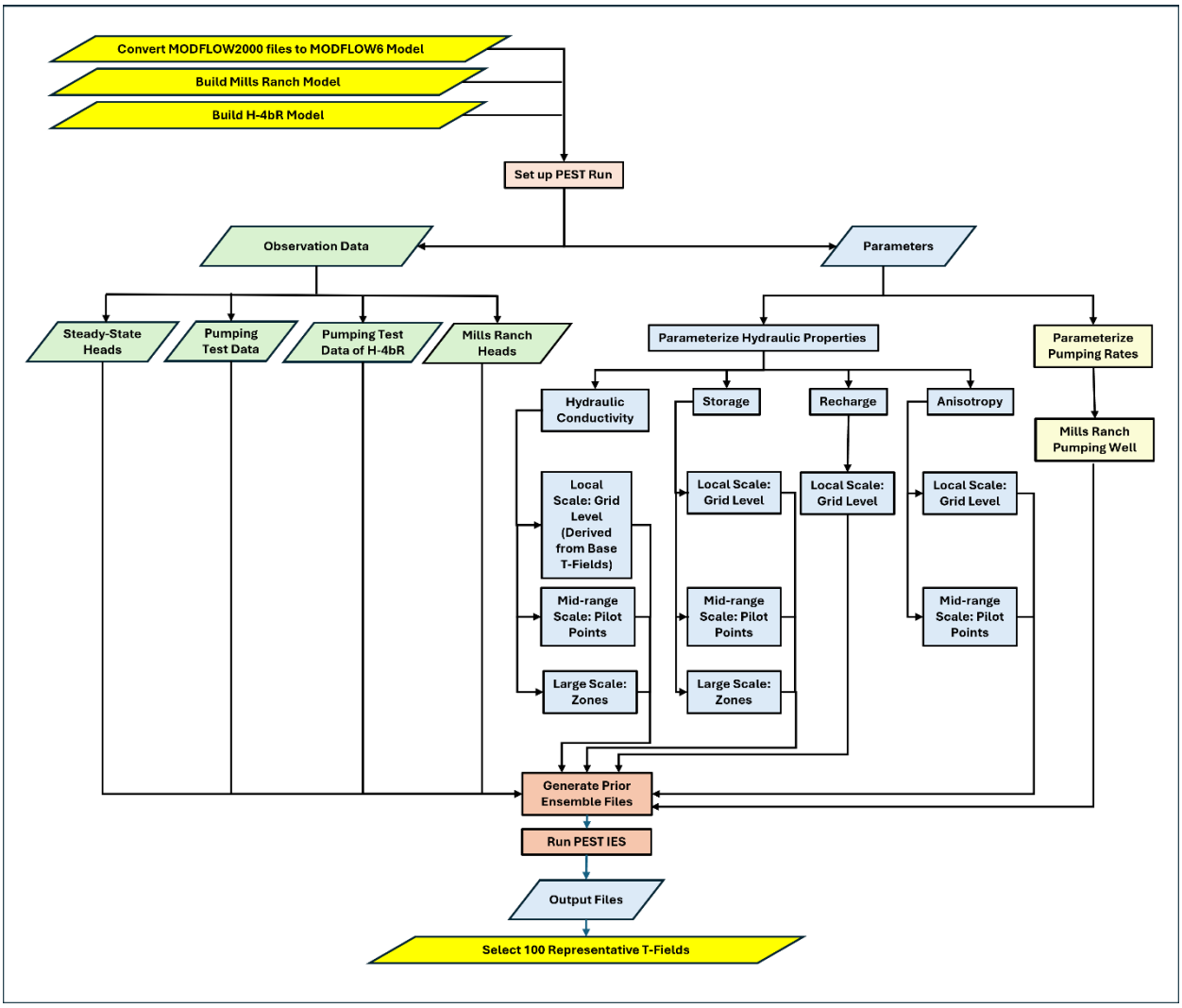


Figure TFIELD-8. Flow Chart of Calibration Workflow

TFIELD-5.1 Model Calibration Targets

TFIELD-5.1.1 WIPP Testing Model Calibration Targets

Two hydraulic head datasets were used to calibrate the Culebra flow model. The first dataset comprises 47 freshwater equivalent heads derived from pressure heads measured across the monitoring well network. This dataset, shown in Table TFIELD-1, was used as steady-state calibration targets (Farinacci and Bowman 2022). Farinacci and Bowman (2022) derived representative head targets for each well by analyzing the full distribution of freshwater equivalent heads and selecting the most appropriate measure of central tendency for that distribution. For each well, histograms and continuous distributions were generated, and the resulting distributions were qualified by type to identify the most appropriate central-tendency measure to represent the head value (e.g., using the mean for a normally distributed dataset or

the median for a skewed dataset). Measurement noise was generated from the central tendency and standard deviation and added to observation targets.

The second dataset consists of drawdown data collected during 10 independent multi-well pumping tests conducted since the 1980s (Table TFIELD-2). Each pumping test was simulated in the forward model using its own transient MF6 model with time discretization based on the duration of the individual test. A single forward-model run includes one steady-state MF6 simulation and 11 transient pumping-test simulations, with each transient simulation initialized using the steady-state heads. All MF6 simulations share the same input parameter fields. However, the pumping-test simulations incorporate the specific pumping well extraction configurations for their respective tests.

Table TFIELD-1. Freshwater Head Observations Used as Steady-state Calibration Targets

Well Name	Head target (m AMSL)
ERDA-9	925.14
AEC-7R	933.37
C-2737	921.32
H-10cR	921.07
H-11b4R	918.42
H-12R	917.91
H-15R	919.86
H-17	916.66
H-19b0	918.73
H-2b2	928.61
H-3b2	919.00
H-4bR	916.78
H-5b	939.76
H-6bR	935.63
H-7b1	914.04
H-9c	912.97
IMC-461	927.52
P-15	917.61
P-17	915.55
SNL-1	938.46
SNL-10	930.74
SNL-12	915.87
SNL-13	920.37
SNL-14	915.94

Well Name	Head target (m AMSL)
SNL-16	917.63
SNL-17a	916.26
SNL-18	936.60
SNL-19	939.25
SNL-2	936.31
SNL-3	937.45
SNL-5	936.57
SNL-8	931.70
SNL-9	930.76
USGS-4	911.13
WIPP-11	938.29
WIPP-12	933.99
WIPP-13	936.35
WIPP-19	934.64
WIPP-25	933.65
WIPP-26	922.36
WIPP-30	938.66
WQSP-1	936.57
WQSP-2	939.39
WQSP-3	934.80
WQSP-4	918.67
WQSP-5	918.17
WQSP-6	921.34

Table TFIELD-2. Summary of Transient Pumping Test Observations Used as Calibration Targets

Pumping Well(s)	Observation Wells	Total # obs.	Reference
WQSP-2	H-18, DOE-2, WQSP-1, WIPP-13	77	Beauheim and Ruskauff 1998
H-19 and H-11	WQSP-5, H-1, H-15, DOE-1, ERDA-9, WIPP-21, H-3b2	143	Beauheim and Ruskauff 1998
WQSP-1	H-18, WIPP-13	36	Beauheim and Ruskauff 1998
WIPP-11	WQSP-2, WQSP-3, WIPP-12, SNL-9, SNL-5, H-6b, SNL-3, SNL-2, SNL-1, WIPP-30, WQSP-1, WIPP-13	250	Toll and Johnson 2006b; Roberts 2006
H-11	H-4b, H-12, H-14, H-15, H-17, DOE-1, CB-1, P-15, P-17, H-3b2	130	Beauheim 1989
WIPP-13	WIPP-19, WIPP-18, H-2b2, H-6b, WIPP-12, WIPP-25, DOE-2, WIPP-30, P-14	167	Beauheim 1987b
SNL-14	H-9c, H-4b, SNL-13, SNL-12, H-15, H-17, C-2737, ERDA-9, H-19b0, H-3b2, H-7, H-11b4	252	Toll and Johnson 2006a; Roberts 2006
P-14	D-268, H-18, WIPP-26, H-6b, WIPP-25	82	Beauheim and Ruskauff 1998
H-3	DOE-1, H-2b2, H-1, H-11b2	69	Beauheim 1987a
H-9bR	H-4bR, Engle, SNL-12, SNL-14, SNL-17	220	Bowman 2014
Mills Ranch	C-2737, ERDA-9, H-2b2, H-4bR, H-9bR, H-15R, H-16, H-17, H-19b0, SNL-12, SNL-10, SNL-13, SNL-14, SNL-17, WIPP-19	22832	Kuhlman and Corbet 2017

TFIELD-5.1.2 Evaluation of Mills Ranch Pumping Response and Pumping Calibration

In mid-2013, WIPP well monitoring programs began observing significant declines in Culebra water levels and monitored pressure in many of the wells located southwest of the WIPP LWB. It was determined that these water level fluctuations were due to pumping and recovery from a well completed in the Culebra and located at the Mills Ranch (Thomas et al. 2017). The pumping rate and production data for the Mills Ranch well during these events were not available for this analysis.

A methodology was developed to incorporate data from wells in the WIPP monitoring well network affected by Mills Ranch pumping (Figure TFIELD-9) into the T-fields recalibration (Bowman et al. 2023). The methodology treats the Mills Ranch variable pumping rate as a fitting parameter. The Culebra response to this pumping was used to estimate initial pumping rates (60 gpm for both pumping parameters) for the Mills Ranch well as part of the calibration process. Unlike planned multi-pad pumping tests used as model calibration targets, the

pumping rate was variable in time, with alternating periods of pumping and recovery. The motivation for including Mills Ranch pumping, even though pumping rates were unknown, was because the pumping event perturbed water levels in Culebra wells over a much larger portion of the monitoring network than previous planned pumping events.

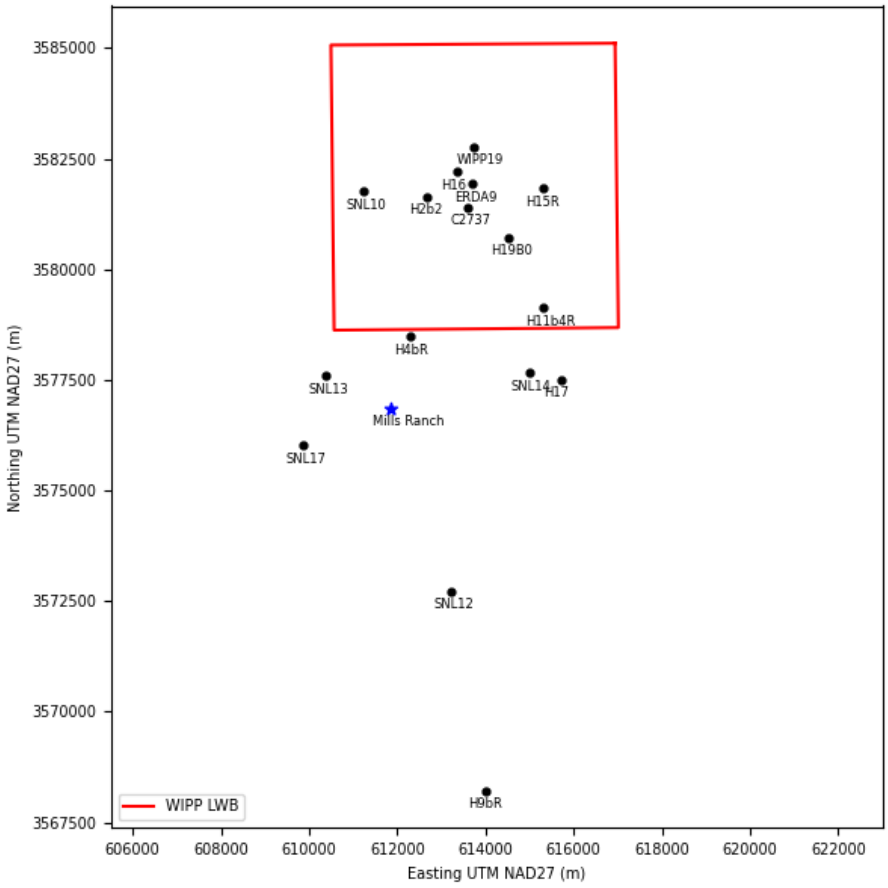


Figure TFIELD-9. Location of Mills Ranch Culebra Well and Neighboring Culebra Wells

TFIELD-5.1.2.1 Mills Ranch Pumping Event Propagated Drawdown

The Mills Ranch pumping event generated large changes in water levels in the Culebra. Wells that were impacted are given in Table TFIELD-3, where water levels declined as much as 20 meters in several wells. For this analysis, the hydraulic response to Mills Ranch pumping is treated as a large scale, multiyear, multi well pumping test, even though the pumping itself was unplanned. The event was opportunistically documented because pressure instrumented monitoring wells recorded the propagated drawdown. Although the pumping conditions were not controlled, the resulting time series data are considered reliable for calibration because the pressure transducers provided continuous, high-resolution measurements and captured clear, repeatable hydraulic responses. These characteristics make the dataset suitable for transient T-field calibration, comparable in utility to planned pumping tests. The 15 wells with measurable

drawdown from the static water level before pumping started on August 22nd, 2013 were included as calibration targets.

The MF6 transient model included 152 stress periods of varying duration, spanning from August 8, 2013, through December 31, 2017. These stress periods encompassed 76 intervals during which the Mills Ranch well was actively pumping. The transient simulation was initialized with steady state heads, consistent with the approach used for the planned multi well pumping test models described in the previous section.

Table TFIELD-3. Wells with Drawdown Observations Impacted by Mills Ranch Pumping

C-2737	H-15R	SNL-13
ERDA-9	H-16	SNL-14
H-2b2	H-17	SNL-17
H-4bR	H-19b0	WIPP-19
H-9bR	SNL-12	SNL-10

TFIELD-5.1.2.2 Estimation of the Mills Ranch Pumping Rate

After several years of nearly continuous pumping with only short recovery periods, the wells affected by Mills Ranch pumping showed a notably longer recovery in water levels during late 2015 to early 2016. A representative example is well SNL-17, where water levels began recovering on November 29, 2015, and continued until February 6, 2016, before drawdown characteristic of Mills Ranch pumping returned (Figure TFIELD-10). During pumping, water levels typically follow a characteristic drawdown curve that declines rapidly at early time with a decreasing rate at later times. When pumping stops, water levels begin to recover, producing characteristic recovery curve that inclines rapidly at early time with a decreasing rate that approaches static formation pressure. As this recovery curve reflects the aquifer's response under a non-pumping scenario, its shape provides an uninterrupted reference for interpreting periods of unknown pumping rate.

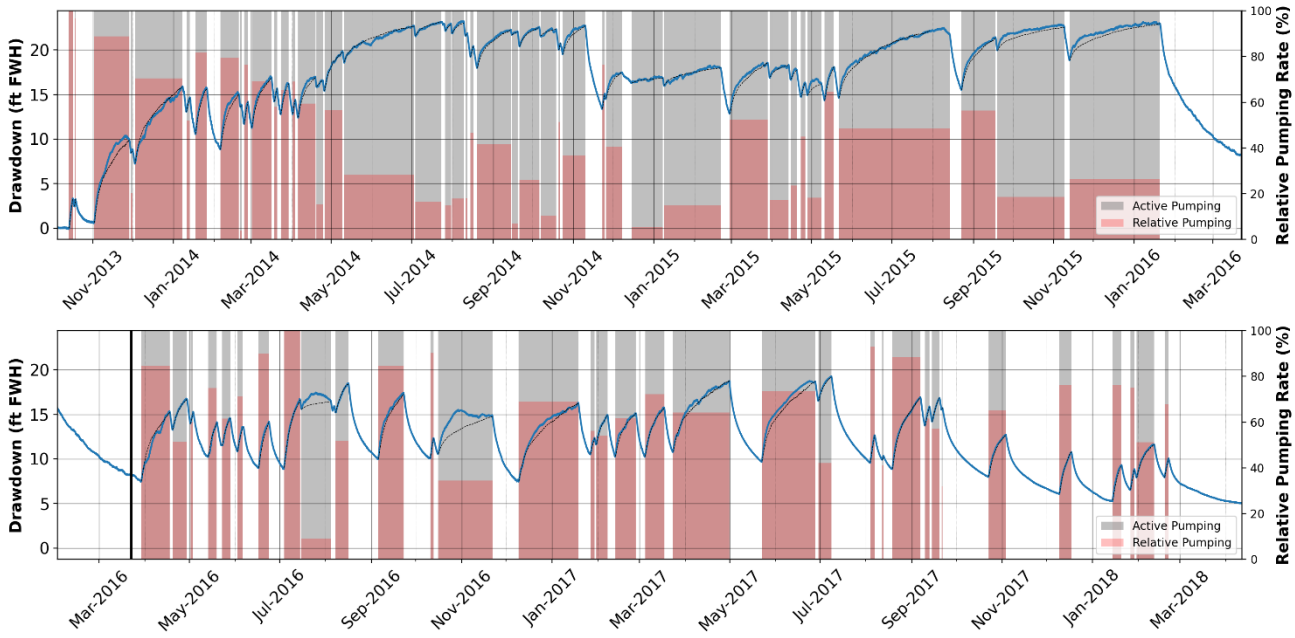


Figure TFIELD-10. Drawdown Observations in Well SNL-17 and Pumping Periods Selected for the Mills Ranch Pumping Well (Vertical Bars). The Pink Fraction of the Bar Represents the Estimated Relative Pumping Rate.

Using the residual drawdown method, also known as the Theis recovery method, the observed recovery response $s_R(t)$ is compared to the theoretical drawdown that would have occurred if pumping had continued, s(t - tp). The ratio of these values scales directly with pumping rate. Figure TFIELD-11 provides a generalized schematic of a pumping and recovery test given by Trabucchi et al. (2018). This quantitative relationship allows unmeasured pumping rates to be estimated as relative pumping rates.

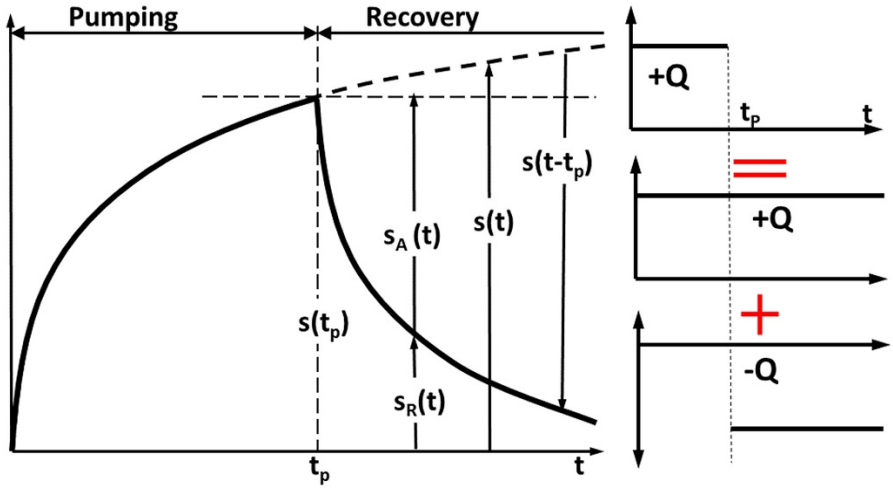


Figure TFIELD-11. A Generalized Pumping in Recovery Curve from Trabucchi et al. (2018). The Left Graph Displays Residual Drawdown, s_R, used in Theis Recovery Method and Agarwal's Drawdown, s_A.

Well SNL-17 was selected over the other wells that also responded to pumping event because it had the quickest response to the start of pumping and recovered quickest, even though drawdown response was not the largest (Kuhlman and Corbet, 2017). Figure TFIELD-12 shows the recovery for 10 affected wells inferred from the change in head measured by pressure transducers (Kuhlman and Corbet 2017). The inset figure shows the spatial location of the Mills Ranch well (blue star) and Culebra monitoring network wells (colored circles).

Observed data in SNL-17 (Figure TFIELD-12) show many clear periods of drawdown and recovery. Wells further from the Mills Ranch pumping well have a more muted response and may not clearly show a response to changes in pumping rate. Periods of pumping produced drawdown curves exhibiting a convex downward, progressively flattening shape; the recovery curve exhibits a convex downward approach to equilibrium, mirroring the late time shape of the drawdown curve. These periods were determined through manual inspection of the SNL-17 15-minute frequency pressure transducer data.

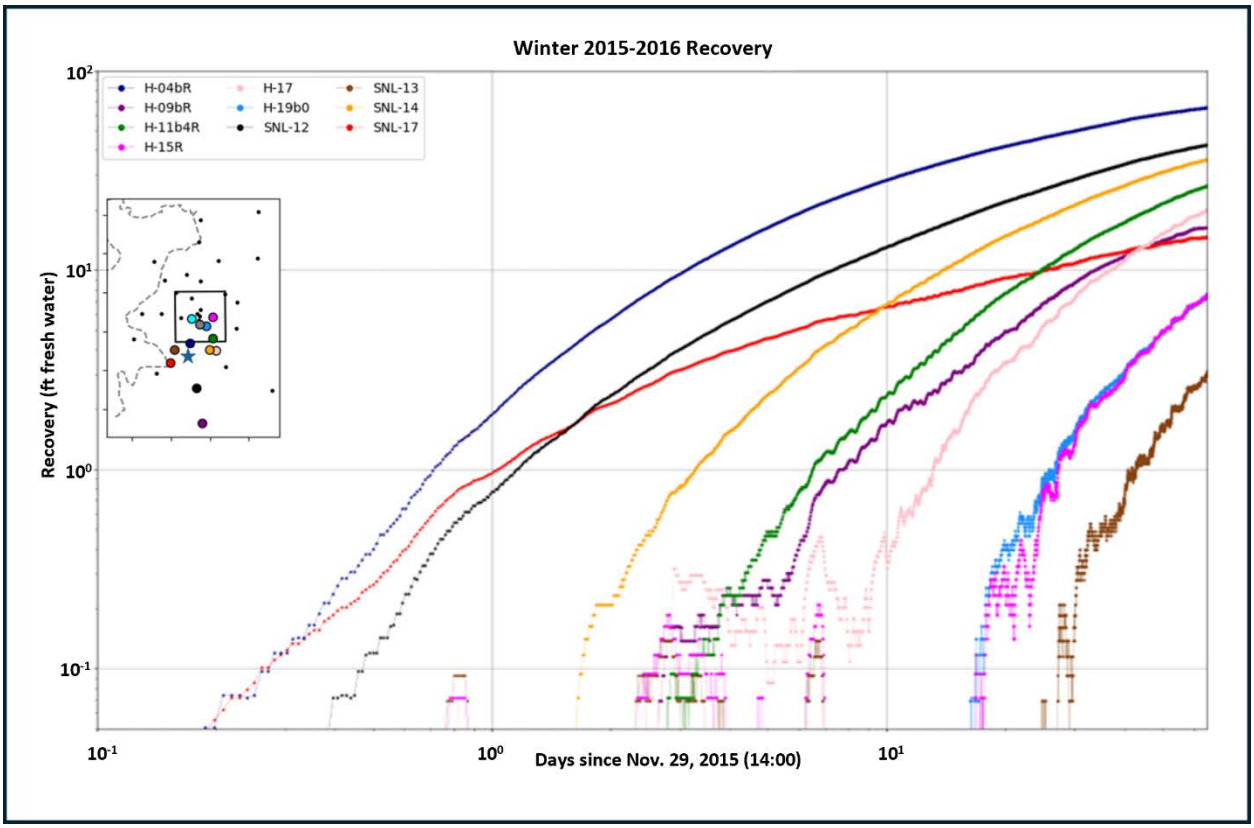


Figure TFIELD-12. Recovery Data for Ten Wells from the Culebra Monitoring Network Located Near Mills Ranch Well (Kuhlman and Corbet, 2017). The Inset Figure shows the Spatial Location of the Mills Ranch Well (Blue Star) and Culebra Monitoring Network Wells (Colored Circles).

The long recovery period (late 2015 to early 2016) was used as a characteristic response which was first inverted (i.e., recovery converted to drawdown) then scaled in drawdown and shifted in time to estimate the relative pumping rate during each on cycle of pumping in the Mills

Ranch well (Theis 1935). This approach is analogous to the Theis theory behind type curve analysis, which provided a relatively good approximation. The Theis conceptualization of flow can be described as two-dimensional, confined, with an infinite radial extent and homogeneous material properties. The main difference between the Culebra and ideal Theis behavior is the double-porosity response of the Culebra. Rather than using a Theis response to fit the data, which would not account for double-porosity effects in the Culebra, the analysis used the characteristic recovery observed from December 2015 to January 2016.

Type curve analysis assumed a "typical" curve can be shifted up or down to estimate the transmissivity ($\boldsymbol{T}$) and storativity ($\boldsymbol{S}$), as long as the radial distance to the pumping well ($\boldsymbol{r}$), the time since pumping began ($\boldsymbol{t}$), and the volumetric flow rate ($\boldsymbol{Q}$) are known. For well SNL-17, the $\boldsymbol{Q}$ for the pumping period ($\boldsymbol{Q_i}$) was unknown, but $\boldsymbol{r}$ was constant, and the formation properties were not changing with time. The drawdown ($\boldsymbol{d}$) response is defined by Theis (1935) as:

$$\boldsymbol{d} = \frac{\boldsymbol{Q}}{\boldsymbol{4\pi T}}\boldsymbol{W(u)}, \qquad \text{Equation (TFIELD.2)}$$

$$\text{where } \boldsymbol{u} = \frac{\boldsymbol{r^2 S}}{\boldsymbol{4Tt}} \qquad \text{Equation (TFIELD.3)}$$

and

$$\boldsymbol{W(u)} = \boldsymbol{-0.5772 - \ln(u) + u - \frac{u^2}{2\cdot 2!} + \frac{u^3}{3\cdot 3!} - \cdots} \qquad \text{Equation (TFIELD.4)}$$

It was assumed that this relationship between $\boldsymbol{Q}$ and $\boldsymbol{d}$ should remain valid for other potentially non-Theis responses. It was also assumed that $\boldsymbol{Q}$ remained low enough that flow to the well was linear (e.g., if flowrates become too large, flow near the well can become turbulent).

Observed drawdown at SNL-17 during each of the pumping periods at Mills Ranch were then used to estimate the relative pumping rate (relative to the “unit” pumping rate represented by the recovery period).

$$\boldsymbol{Q_i} = \boldsymbol{Q}\frac{\boldsymbol{d_i}}{\boldsymbol{d_{rec}(\tau)}} \qquad \text{Equation (TFIELD.5)}$$

where $\boldsymbol{Q}$ represents an unknown “unit” or characteristic pumping rate; $\boldsymbol{Q_i}$ represents the pumping rate during the pumping interval $\boldsymbol{i}$; $\boldsymbol{d_i}$ is the measured drawdown at the end of the pumping interval $\boldsymbol{i}$ and $\boldsymbol{d_{rec}(\tau)}$ is the predicted drawdown estimated by shifting the recovery data from the late 2015 to early 2016 period, at the same number of days.

Figure TFIELD-10 shows individual pumping periods as vertical grey bars. The analysis of the recovery data was performed by estimating the scale factor (shown as the pink fraction of the

vertical bars in Figure TFIELD-10) by determining the relative drawdown ($\boldsymbol{d_i}$) between the beginning and end of the pumping interval.

The estimated relative pumping rates make physical sense where the initial pumping rate was high (November 2013) and decayed with time until about July 2014. Overall pumping rates before and after the 2015-2016 break appear to be different (Kuhlman and Corbet 2017), so two different multipliers were estimated for each pumping period inside the PEST calibration. Figure TFIELD-13 provides a violin plot of the distributions of estimated Mills Ranch pumping rates. A violin plot shows the full distribution of simulated pumping rates across the 100 selected realizations, including the median, range, and the density of values, providing a clear visualization of uncertainty and variability. Early average pumping rate estimates are similar to those of Thomas et al. (2017) (38 gpm). Following the extended shutdown from late 2015 to early 2016, the subsequent drawdown responses, as displayed in Figure TFIELD-10 for SNL-17, show markedly reduced magnitude, indicating that pumping resumed at substantially lower relative rates.

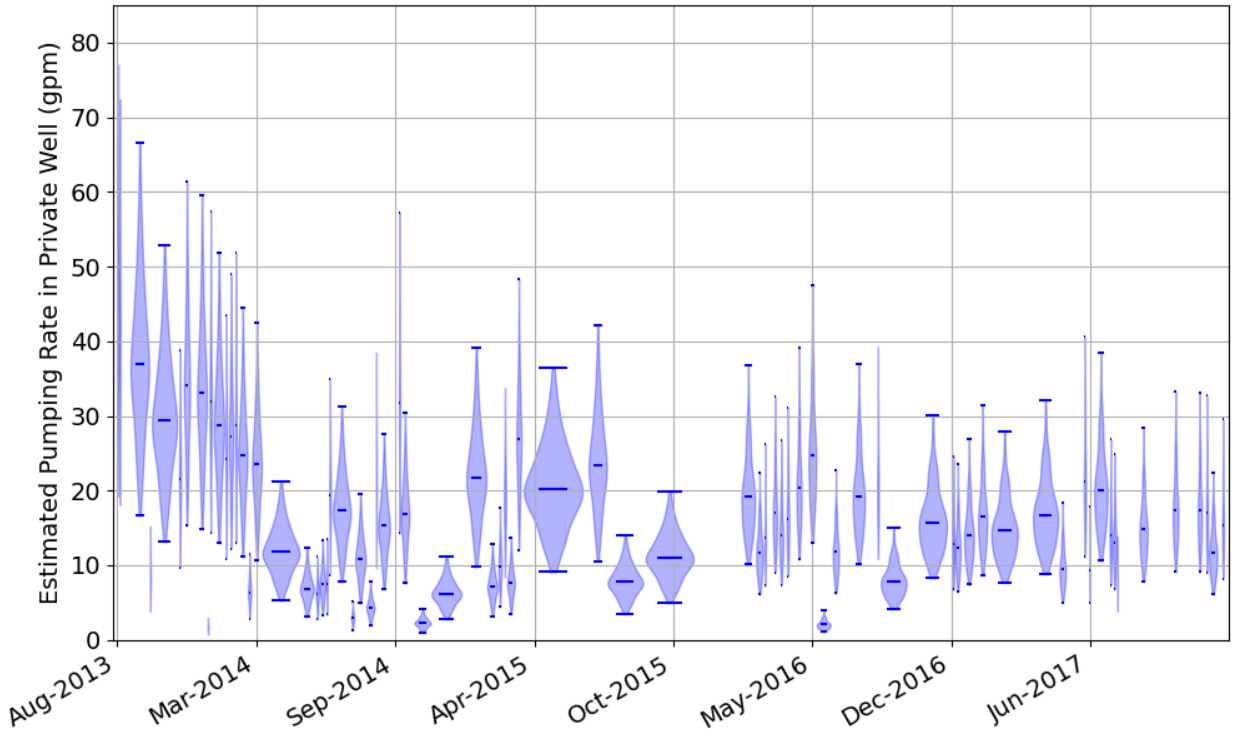


Figure TFIELD-13. Distributions of Estimated Mills Ranch Pumping Rates for the 100 Selected Realizations

TFIELD-5.1.3 Single-Well Formation Performance Measurements of Transmissivity

This subsection summarizes the transmissivity estimates obtained from single-well hydraulic tests conducted at individual Culebra monitoring wells (Figure TFIELD-14). These tests involved

pumping a well at controlled discharge rates and analyzing the resulting drawdown to derive localized transmissivity values (Bowman et al. 2023). Because these single-well tests represent conditions immediately surrounding each borehole and may not capture the full variability within a 100-m model grid cell, the measured transmissivities were incorporated with an allowance for uncertainty. Pilot-point transmissivity values at well locations were permitted to vary around the test-derived estimates according to a normal distribution applied to their log-transformed values, using a standard deviation of 0.25 $\log_{10}(m^2/s)$. This approach allows most realizations to fall within roughly half a log cycle of the measured values, providing a realistic balance between honoring the well-test data and accommodating the broader regional calibration.

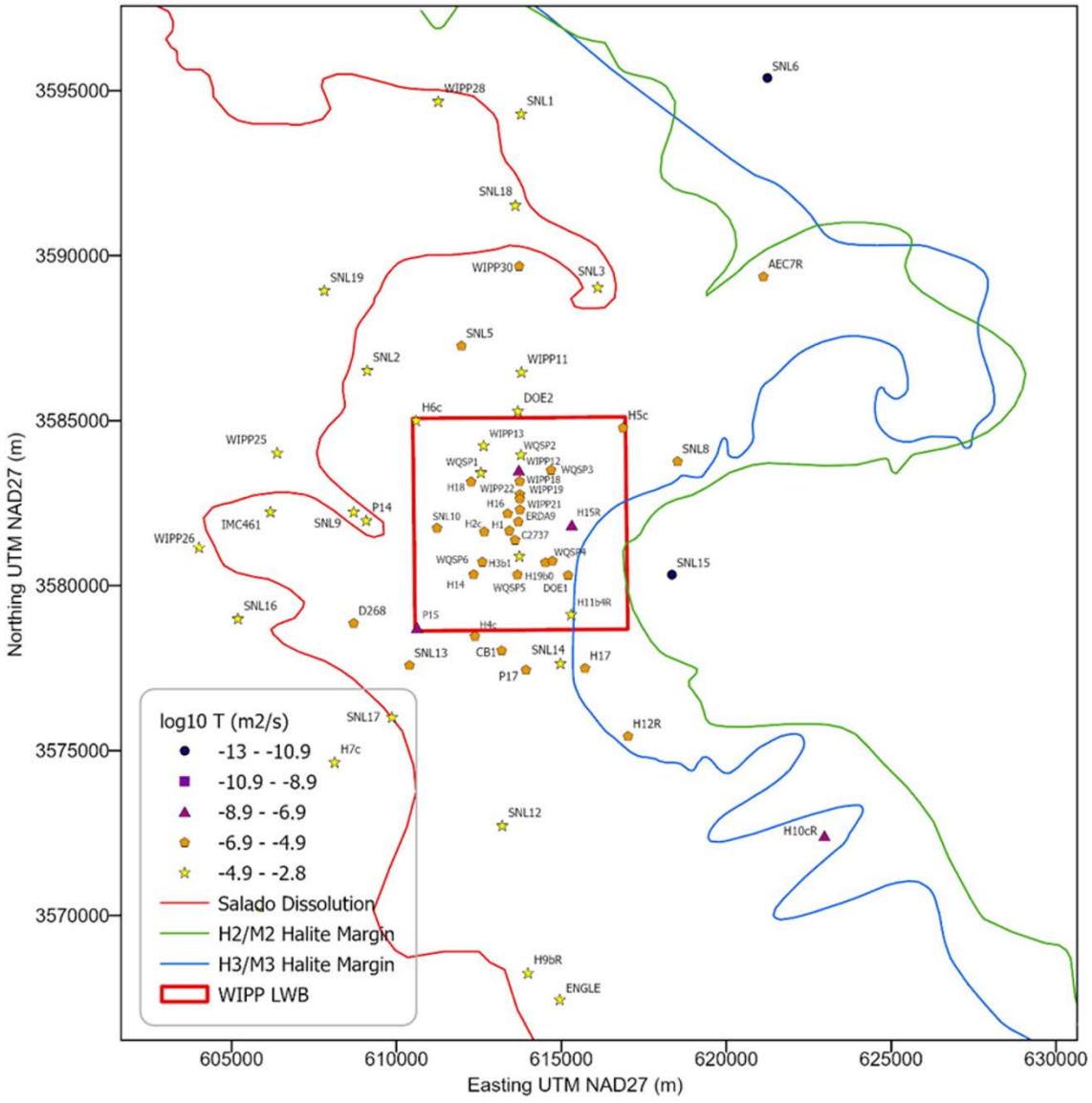


Figure TFIELD-14. Transmissivity Estimates from Single Well Hydraulic Tests

TFIELD-5.2 Calibration Setup and Configuration

Because of the stochastic nature of the base T-fields, the creation and definition of zones for parameters associated with each field followed the base T-fields defined in Hart et al. (2008). The selection of pilot point locations and initial values were the same for every calibrated base field for the CRA-2026 calibrations but differed from those of Hart et al. (2009).

The T-fields are spatially variable input parameters for MF6. The spatial variability of these fields is modified from the base T-field using a set of overlapping multipliers at different spatial scales (i.e., grid-level multipliers, pilot points, and zones). Together, these base fields and the different scales of multipliers comprise the T-fields used in MF6, which were handled differently for *T*, *A*, *R*, and *S* (Figure TFIELD-8). In this section, the parameterization designs used for the five main groups of parameters, namely transmissivity, storage, horizontal anisotropy, recharge, and the Mills Ranch pumping event, are described in detail.

TFIELD-5.2.1 Selection of Pilot Point Locations

A set of overlapping multipliers at different scales was used so that PEST would have some ability to adjust the base T-field geostatistical realizations to fit the observed data (Bowman et al. 2023). Multipliers were defined in each model element; there was a coarser grid of pilot points, and there were regional multipliers for some parameters (Figure TFIELD-8). Figure TFIELD-15 shows the intermediate scale pilot points that were spaced evenly in a 500 by 500 meters grid across the model domain, excluding the no-flow northwestern portion of the model (red region in figure). While pilot points were included in the constant-head area (blue region in the figure), the effect of adding pilot points in this area does not change the flow solution because the head value was held constant. The values at this intermediate scale were estimated at pilot point locations, then kriging was used to compute the associated values at each model element. This process ensures a level of smoothness at the finest scale (i.e., the scale of model elements – 100 m) but allows variability at a slightly larger scale.

The initial stochastic realizations for the pilot point multiplier parameters were drawn from a $\log_{10}$ multivariate normal distribution with a mean of unity and a covariance matrix described by an exponential variogram with parameters listed in Table TFIELD-4. For this analysis, an exponential variogram model was used to describe the relation between separation distance and correlation for the purposes of generating stochastic realizations of pilot point and grid-scale parameter values. The variograms for these two parameter types were selected based on expert judgement and visual inspection of the resulting parameter realizations. The goal of these spatially varying parameter sets is to facilitate minimal and plausible adjustment of the indicator geostatistical realizations to improve the reproduction of observed groundwater level conditions. In this way, the pilot point parameter variogram was selected to represent plausible patterns of lower-spatial-frequency adjustments, while the grid-scale parameter variogram was selected to represent plausible patterns of higher-spatial-frequency adjustments.

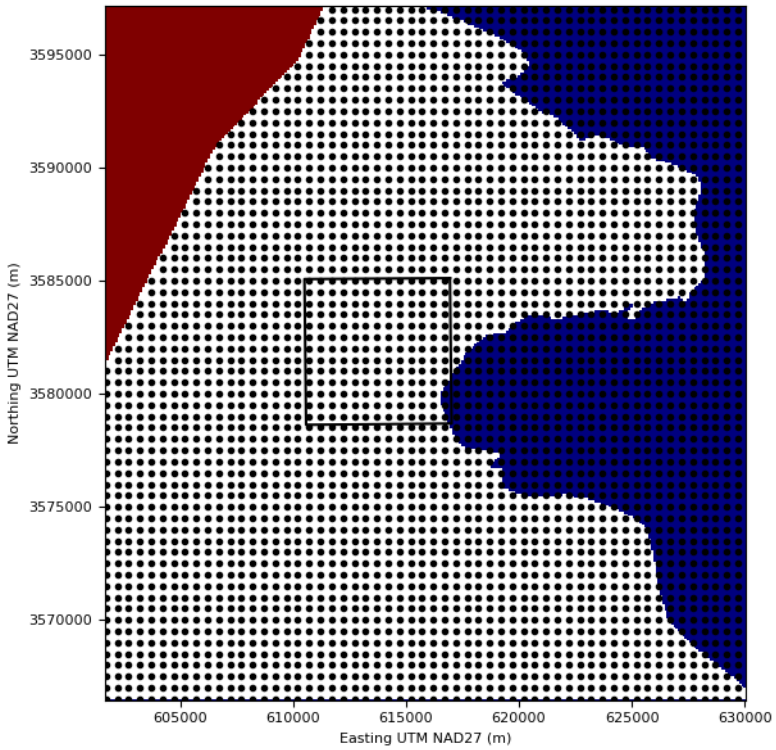


Figure TFIELD-15. Pilot Point Multiplier Locations. Pilot Point Multipliers were used Allow PEST to Explore Potential Uncertainty in Parameter Estimates Outside of Base T-field Spatial Patterns.

Table TFIELD-4. Variogram Parameters for the Grid-Scale

Parameters	Value
Model Type	Exponential
Nugget	0.0
Range	9500 m

TFIELD-5.2.2 Creation of Parameter Zones

Parameter zones (the coarsest scale) were defined for each of the calibrated parameters. These zones were defined to represent regional-scale parameters consistently with the conceptual model for Culebra flow defined in Hart et al. (2008). The parameter zones were chosen to organize common pilot point groups together in the PEST calibration.

TFIELD-5.2.3 Transmissivity Parameters

Transmissivity was subjected to three spatial scales of parameterization: grid-scale parameters, pilot points multipliers, and zonal multipliers.

Grid-scale parameters allowed for the variation of properties at the finest scale (100 m). Pilot point multipliers were included to influence the transmissivity field at an intermediate scale (500 m). Zonal multiplier parameters adjusted the transmissivity fields at the largest regional scale (10^3-10^4 m).

TFIELD-5.2.3.1 Grid-scale Hydraulic Conductivity

The base T-field geostatistical realizations for transmissivity from AP-114 (Hart et al., 2008) were used to directly populate the grid-scale elements of transmissivity. Since the model assumes a constant thickness (b=7.75 m), transmissivity is its product with hydraulic conductivity, i.e.,

$$T=Kb. \qquad \text{Equation (TFIELD.6)}$$

Initial hydraulic conductivities for each model grid cell were derived from the corresponding transmissivities in the base T-fields. Each grid-scale K was allowed to vary between 2.57E-25 m/s and 4.6E-3 m/s across the entire 1,000 transmissivity realizations. These values are also included in a spatial correlation defined by a similar variogram described in Hart et al. (2008). The variogram parameters used in this analysis are provided in Table TFIELD-4.

Because the available transmissivity measurements are too sparse to develop an empirical variogram, the variogram used in the pilot-point regularization was specified to enforce a plausible spatial correlation structure at the grid scale. This approach is standard when variograms cannot be meaningfully estimated from field data. This has the effect of preventing sharp transmissivity contrasts over short distances. Keeping the nugget (i.e., a discontinuity in the variogram at zero distance) zero avoids adding too much variability in spatial data at very short distances.

TFIELD-5.2.3.2 Transmissivity Pilot Point Multipliers

A set of intermediate-scale pilot point multipliers was also used to allow PEST to adjust the T-fields outside of the spatial patterns present in the base T-field geostatistical realizations. These initial stochastic realizations for the pilot point multipliers were drawn from a $\log_{10}$ multivariate normal distribution with a mean of unity and a covariance matrix described by an exponential variogram provided in Table TFIELD-5.

Table TFIELD-5. Variogram Parameters for Pilot Point Multipliers

Parameters	Value
Model Type	Exponential
Nugget	0.0
Range	30,000 m

TFIELD-5.2.3.3 Transmissivity Zone Multipliers

Zone-based multipliers were used to express regional-scale changes in transmissivity. These zones were consistent with the conceptual Culebra flow model defined in Hart et al. (2008), with the exception of the *T* and *A* parameter zones. In previous work, these zones were treated as stochastic zones, meaning that each zone was assigned a probability distribution so that *T* varied randomly from one realization to the next. This approach produced a mixture of higher and lower values across the 1,000 realizations to represent regional uncertainty. However, in the most recent T-field calibrations, the *T* and *A* zones were combined into a single zone because the current calibration approach, using pilot points and spatial regularization, provides sufficient spatial variability. Additional stochastic zoning would not meaningfully increase variation in the parameter fields.

As shown in Figure TFIELD-16, there are four transmissivity zones:

Zone 1 - a mixture of higher and lower transmissivity values corresponding to the stochastic zone provided in the base fields that defined the center of the model domain,

Zone 2 - a high transmissivity zone located to the west corresponding to the area of Salado

dissolution where enhanced fracture permeability has been documented,

Zone 3 - a low transmissivity zone where the Culebra is bounded above and below by halite cemented units that restrict vertical fracture development and reduce hydraulic conductivity, and

Zone 4 - the northwestern no-flow boundary, representing areas where the Culebra is hydraulically isolated and transmissivity effectively approaches zero.

Grid-scale and pilot point parameters were assigned to model grid cells in Zones 1 and 2 and multiplied by zonal multipliers. Table TFIELD-6 gives a summary of the range of hydraulic conductivities for each parameterization.

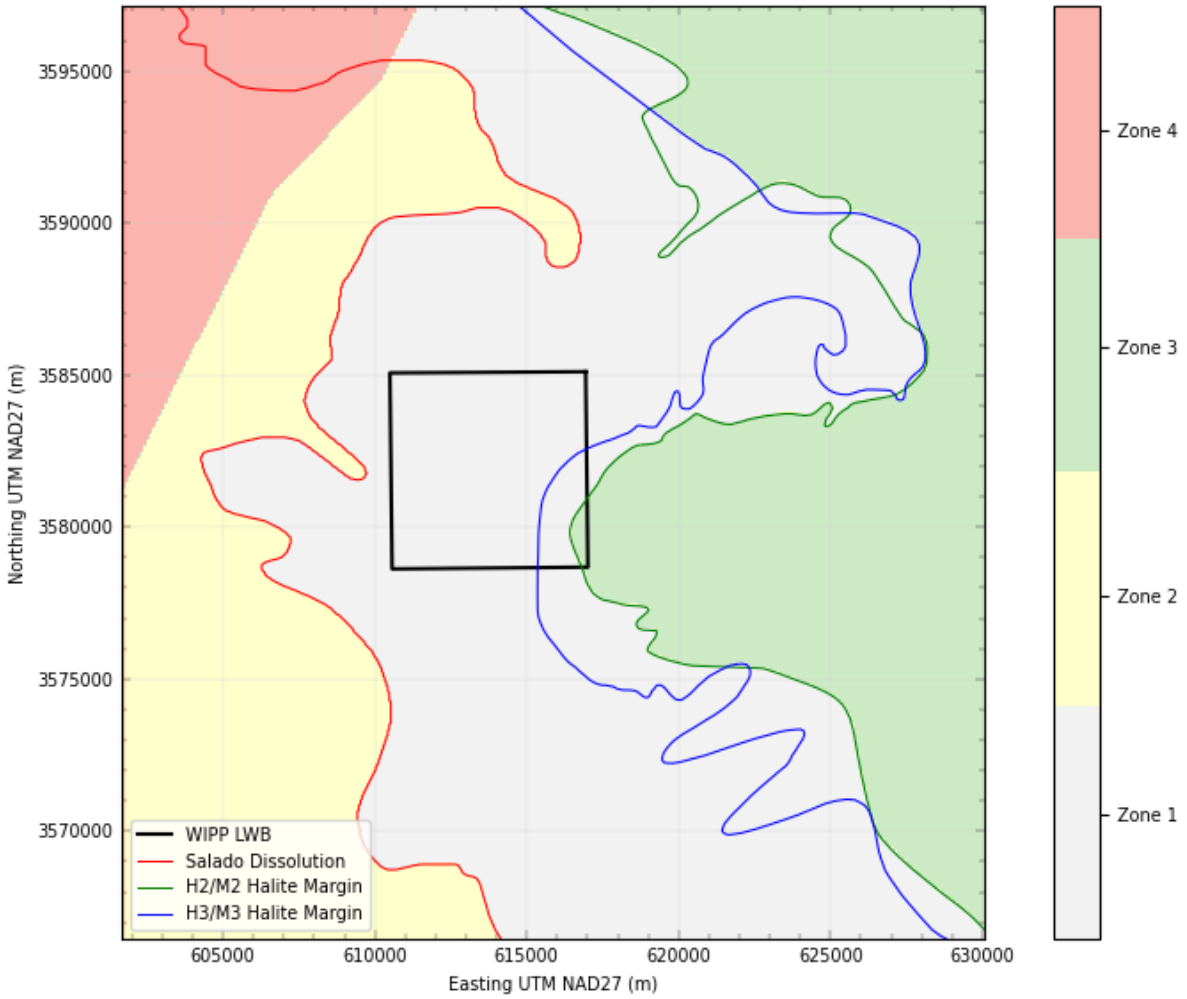


Figure TFIELD-16. Transmissivity Zone Map

Table TFIELD-6. Summary Table of Hydraulic Conductivity Parameterization.

Spatial Scale	Parameter Type	Description	Initial *K* Value (m/s)	Lower *K* Limit (m/s)	Upper *K* Limit (m/s)
Grid-Scale	Direct	Applied directly to model cells	Variable	2.57E-25	4.6E3
Pilot Point	Multiplier	Multiplied to *K* field	1.00	0.01	100.00
Zone 1	Multiplier	Multiplied to Zone 1	1.00	0.01	100.00
Zone 2	Multiplier	Multiplied to Salado Dissolution Zone	1.00	0.01	100.00
Zone 3	Multiplier	Multiplied to Halite Sandwich Zone	1.00	1.00	1.00
Zone 4	Multiplier	Multiplied to No Flow Zone	1.00	1.00	1.00

Note: During calibration, hydraulic conductivity is adjusted either directly or using a multiplier. In addition, hydraulic conductivity is adjusted at multiple spatial scales.

TFIELD-5.2.4 Storativity Parameters

Although the PA Culebra flow model is steady state, the calibration process temporarily uses the transient groundwater flow equation to reproduce pumping test drawdown data. This requires estimating storage parameters. Once calibration is complete, the final PA model solves only the steady-state equation. Similar to the transmissivity parameterization, storage parameters are derived for three spatial scales in the Culebra. These are input into the flow model as specific storage (S_s) where again b is a constant thickness (7.75 m),

$$S = S_s\, b. \qquad \text{Equation (TFIELD.7)}$$

During calibration, specific storage is adjusted at multiple spatial scales (grid-scale, pilot point and zonal multipliers).

Although portions of the Culebra may not behave as fully confined in reality (Powers et al. 2006), the entire model domain is treated as confined so that transmissivity remains constant. This assumption preserves the linearity of the groundwater-flow equation and simplifies both calibration and numerical solution. Because unconfined conditions introduce nonlinearity, the model preserves linearity by assigning higher storativity values to areas of the Culebra interpreted as unconfined, thereby approximating unconfined behavior without modifying the governing equations.

TFIELD-5.2.4.1 Grid-scale Storativity

Initial stochastic base fields were not produced for any parameters besides transmissivity. This is because hydraulic conductivity is the crucial parameter in solving the steady state groundwater flow equation. Therefore, the grid-scale storage parameters were not populated from the base T-fields. Instead, the grid-scale storage parameters were allowed to vary according to the values assigned to the different storativity zones. Initial values and ranges for S_s are shown in Table T-FIELD-7. The variogram for storativity grid-scale parameters was the same as the grid-scale transmissivity parameter (Table TFIELD-4). The shared variogram does not assume any physical correlation between storativity and transmissivity, nor does it treat them as arising from the same process. As described for the grid-scale parameters (Section 5.2.2.1 and Section 5.2.3.1), the grid-scale variogram is not a data-derived structural model of either parameter; it is a geostatistical smoothness constraint that enforces spatial continuity (exponential model, 9,500 m range, zero nugget) to permit only minimal and plausible cell-to-cell adjustment and to prevent unrealistic sharp contrasts over short distances. Specific storage values were fixed in Zones 3 and 4 due to the bounding halite to the east and the no-flow boundary to the northwest.

TFIELD-5.2.4.2 Storativity Pilot Point Multipliers

The same pilot points locations used for K were also applied to S_s. This provides comparable spatial flexibility in both parameter fields while allowing their values to be estimated independently. Pilot points ranged between 0.01 and 100 m^{-1} (Table TFIELD-5). Pilot point multipliers were applied to storativity in the constant-head zone, but they do not impact the results there, because the head is specified.

TFIELD-5.2.4.3 Storativity Zone Multipliers

Four storativity zones and one no-flow area were defined for storativity estimation. Zone 0 defines areas considered fully confined, with a western boundary generally coinciding with the Salado dissolution margin. Zone 1 is considered a confined to unconfined transition zone between Zones 0 and 2. Zone 2 in the westernmost region in the Nash Draw area, west of the Salado Dissolution boundary is interpreted as unconfined (Powers et al. 2006). The initial specific storage values for Zone 2 were comparatively larger, to better represent the unconfined nature of the zone. Zone 3 is confined and storage values are fixed, due to the constant head boundary condition.

Model grid cells in Zone 4 were inactive. A map of the storativity zones is shown in Figure TFIELD-17.

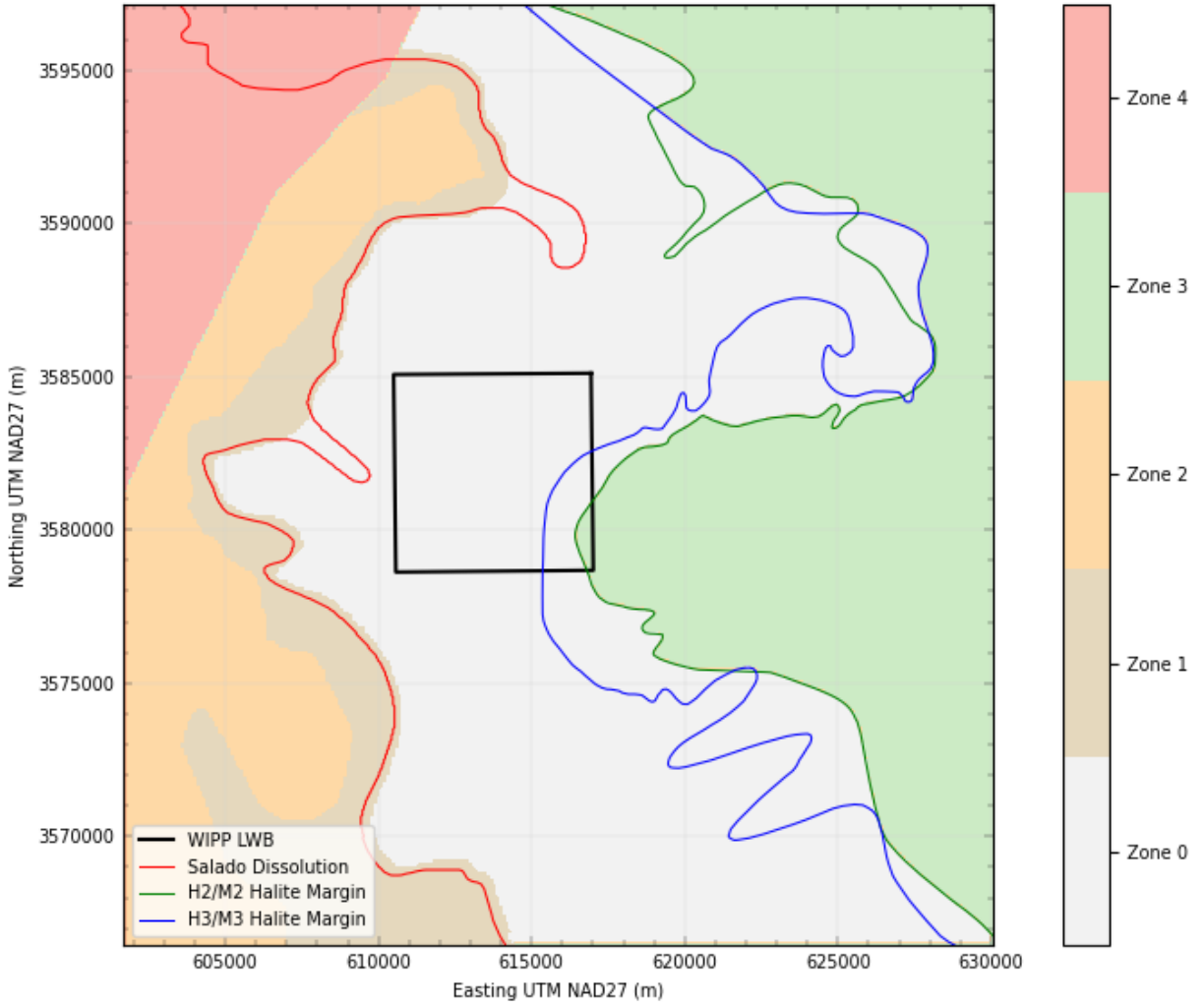


Figure TFIELD-17. Spatial Distribution of Storativity Zones. Zone 0 is Confined; Zone 1 is a Transition Between Confined and Unconfined; Zone 2 is Unconfined; Zone 3 is Constant Head; Zone 4 is Inactive.

Table TFIELD-7. Summary of Specific Storage Parameters Used in the Model (lower and upper limits define the range of plausible values)

Spatial Scale	Parameter Type	Description	Initial Value (m^{-1})	Lower Limit (m^{-1})	Upper Limit (m^{-1})
Pilot Point	Multiplier	Multiplied to S_s field	1.00	0.01	100.00
Zone 0	Direct	Applied to Confined Zone	1.3E-06	4.1E-09	4.1E-06
Zone 1	Direct	Applied to Transition Zone	1.3E-05	1.3E-09	4.1E-02
Zone 2	Direct	Applied to Unconfined Zone	4.1E-03	4.1E-06	4.1E-02
Zone 3	Direct	Applied to Constant Zone	1.3E-06	1.3E-08	1.6E-06
Zone 4	Direct	Applied to No-Flow Zone	N/A	N/A	N/A

TFIELD-5.2.5 Horizontal Anisotropy Parameters

The horizontal anisotropy ratio (the ratio of hydraulic conductivity in the *y*-direction to the hydraulic conductivity in the *x*-direction) fields were subjected to the same three levels of parameterization as transmissivity and storativity.

TFIELD-5.2.5.1 Grid-Scale Horizontal Anisotropy

The grid-scale anisotropy ratios were initialized at 1 (isotropic conditions). During calibration, they were allowed to vary between 0.25 and 3.98 and were interpolated using the same variogram structure applied to the grid-scale transmissivity field (Table TFIELD-4). The anisotropy ratio was given a wide range of geologically reasonable values, to account for anisotropy arising from the fractured nature of the Culebra.

TFIELD-5.2.5.2 Horizontal Anisotropy Pilot Point Multipliers

Pilot points were distributed throughout the model domain, except in the inactive zone, and were interpolated using the same variogram structure used for transmissivity pilot points. Pilot-point values were initialized at 1.0 and allowed to vary between 0.01 and 100 to provide sufficient calibration flexibility. After kriging, these pilot-point values contributed to the grid-scale anisotropy field, which was ultimately constrained to fall within the geologically reasonable grid-scale range of 0.25 to 3.98.

TFIELD-5.2.5.3 Horizontal Anisotropy Zonal Multipliers

Because grid scale anisotropy ratios are derived directly from the transmissivity field, the same zonation used for transmissivity was also applied to anisotropy (Figure TFIELD-16). Consequently, anisotropy ratios were fixed at 1 in both the constant-head and inactive zones (Zones 3 and 4).

The *T* values in the north-south (*y*) direction were calculated by multiplying the transmissivity (*T*) value for the east-west (*x*) direction (given in the T-field) by the anisotropy value (*A*) at a given cell:

$$T_y = T_x A. \qquad \text{Equation (TFIELD.8)}$$

A summary table of the parameter specifications is provided in Table TFIELD-8.

Table TFIELD-8. Summary Table of Anisotropy Parameters

Spatial Scale	Parameter Type	Description	Initial Value	Lower Limit	Upper Limit
Grid-Scale	Direct	Applied to A field	1.00	0.25	3.98
Pilot Point	Multiplier	Multiplied to A field	1.00	0.01	100.00
Zone 1	Multiplier	Multiplied to Stochastic Zone	1.00	0.32	3.20

Spatial Scale	Parameter Type	Description	Initial Value	Lower Limit	Upper Limit
Zone 2	Multiplier	Multiplied to Salado Dissolution Zone	1.00	0.32	3.20
Zone 3	Multiplier	Multiplied to Constant Zone	1.00	1.00	1.00
Zone 4	Multiplier	Multiplied to No Flow Zone	1.00	1.00	1.00

TFIELD-5.2.6 Spatial Distribution of Recharge

The conceptualization of Culebra flow and transport initially presented in Holt (1997) and later updated (Hart et al. 2008); indicates that a groundwater divide exists southwest of the WIPP site (in CRA-2004, a boundary of the model domain existed here). Hart et al. (2008) represented this possible groundwater divide by a line of recharge cells extending northwest to the southeast in the southwestern-most portion of the model domain. Consistent with this representation, model grid cells intersecting the groundwater divide line were assigned to Zone 1, while all the other model cells were assigned to Zone 0. The recharge parameters only contained grid-scale parameterization.

TFIELD-5.2.6.1 Grid-Scale Recharge

Recharge in Zone 0 was fixed at 10^{-30} m/s (effectively 0) and initialized at 10^{-15} m/s in Zone 1. Recharge in Zone 0 was set to a very small value consistent with areas of possible recharge delineated by Powers (2006). During calibration, recharge values were allowed to vary between 10^{-19} and 10^{-10} m/s. Three model grid cells to the far west of Zone 1 were fixed at 10^{-19} m/s so that recharge would increase towards the east. See Figure TFIELD-18 for a map of the recharge zone.

TFIELD-5.2.7 Estimated Mills Ranch Pumping Rates

Because the actual pumping rate at the Mills Ranch well is not documented, two pumping-rate multipliers were estimated to represent the unknown pumping conditions before and after the recovery period between late 2015 and early 2016. These multipliers were applied to two corresponding base pumping rates, one for the early period and one for the late period. The time-varying pumping rate for each stress period was constructed using the expression:

$$\boldsymbol{Q_i = Q \frac{d_i}{d_{rec}(\tau)}} \qquad \text{Equation (TFIELD.9)}$$

where Q is the unknown base ("unit") pumping rate (m^3/s), Q_i is the pumping rate applied during stress period time interval i; d_i is the measured drawdown at the end of interval i, $d_{rec}\ (t)$ is the predicted drawdown obtained by shifting the 2015-2016 recovery data forward in time by t days, the duration of interval i. This formulation scales the base pumping rate according to the

ratio of observed drawdown to the characteristic recovery response. An initial value of 3.785 × 10^{-3} m^3/s (60 gallons per minute [gpm]) was assigned to both base pumping rate parameters

For each of the 76 stress periods, the pumping rate was calculated by applying: (1) the appropriate base pumping rate (early or late), (2) the pumping-rate multiplier estimated by PEST, and (3) the drawdown-to-recovery ratio $d_i/d_{rec}(t)$. This approach enabled reconstruction of a realistic pumping-rate history in the absence of direct pumping records for the Mills Ranch well.

A summary table of recharge parameters is provided in Table TFIELD-9.

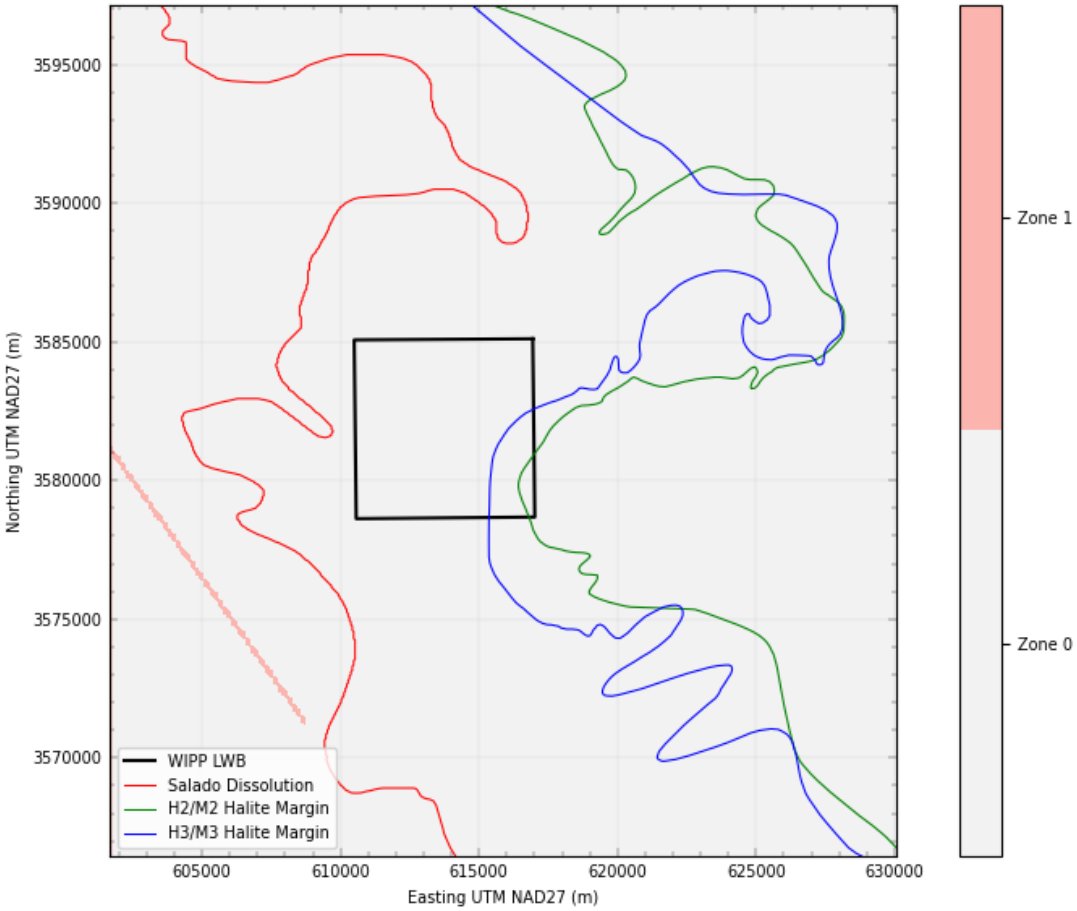


Figure TFIELD-18. Recharge Zones. Zone 1 consists of grid cells that intersect the Linear Feature Directed Southeast from the Center of the West Edge of the Model Domain. Zone 0 has No Recharge.

Table TFIELD-9. Summary Table of Recharge Parameters

Spatial Scale	Parameter Type	Description	Initial Value Recharge (m/s)	Lower Limit Recharge (m/s)	Upper Limit Recharge (m/s)
Zone 0	Direct	Applied directly to cells not in groundwater divide	1E-30	1E-30	1E-30
Zone 1	Direct	Applied directly to cells in groundwater divide	1E-15	1E-19	1E-10
Three cells in Zone 1	Direct	Applied to three cells in groundwater divide	1E-19	1E-19	1E-10

TFIELD-5.2.8 Model Initial and Boundary Conditions

This section describes the initial and boundary conditions used in the model. Section TFIELD-5.2.8.1 discusses the boundary conditions implemented prior to calibration. Section TFIELD-5.2.8.2 discusses the initial parameter values. Section TFIELD-5.2.8.3 discusses the assigned initial head surface.

TFIELD-5.2.8.1 Boundary Conditions

A constant head boundary is applied along the north-south and east-west edges of the model domain. A constant-head boundary stabilizes the model during transient calibration, ensuring that the drawdown caused by Mills Ranch pumping is reproduced realistically without forcing transmissivity or storativity to compensate for boundary uncertainty.

Figure TFIELD-19 depicts the constant head boundaries as solid green lines. The initial heads were generated from an extrapolated surface fitted to the observed potentiometric surface using the expression (Appendix A in Hart et al. 2009):

$$\boldsymbol{h(x,y) = a + b(y + d\,sin(y)\,|y|^{p}) + c(ex^{3} + fx^{2} - x)} \quad \text{Equation (TFIELD.10)}$$

In TFIELD.10, *h(x,y)* is the hydraulic head assigned to a model grid cell; *x* and *y* are normalized cell-center coordinates (−1 to +1); and *a, b, c, d, e, f,* and *p* are adjustable coefficients that control the shape of the fitted surface. The parameter estimation that generated the values in TFIELD-10 was performed prior to the calibration of the T-fields (Bowman et al. 2023). The extrapolated surface was fitted to freshwater heads from TFIELD-1. Table TFIELD-10 lists the seven coefficients derived by fitting the multivariate equation to the observed hydraulic heads. The initial head surface was compared to the observed steady-state freshwater heads at the 47 head targets. The surface-extracted heads yield an R^2 of 0.88, an RMSE of 3.2 m, and a mean error of approximately 0 m, with residuals ranging from −7.9 to +8.1 m.

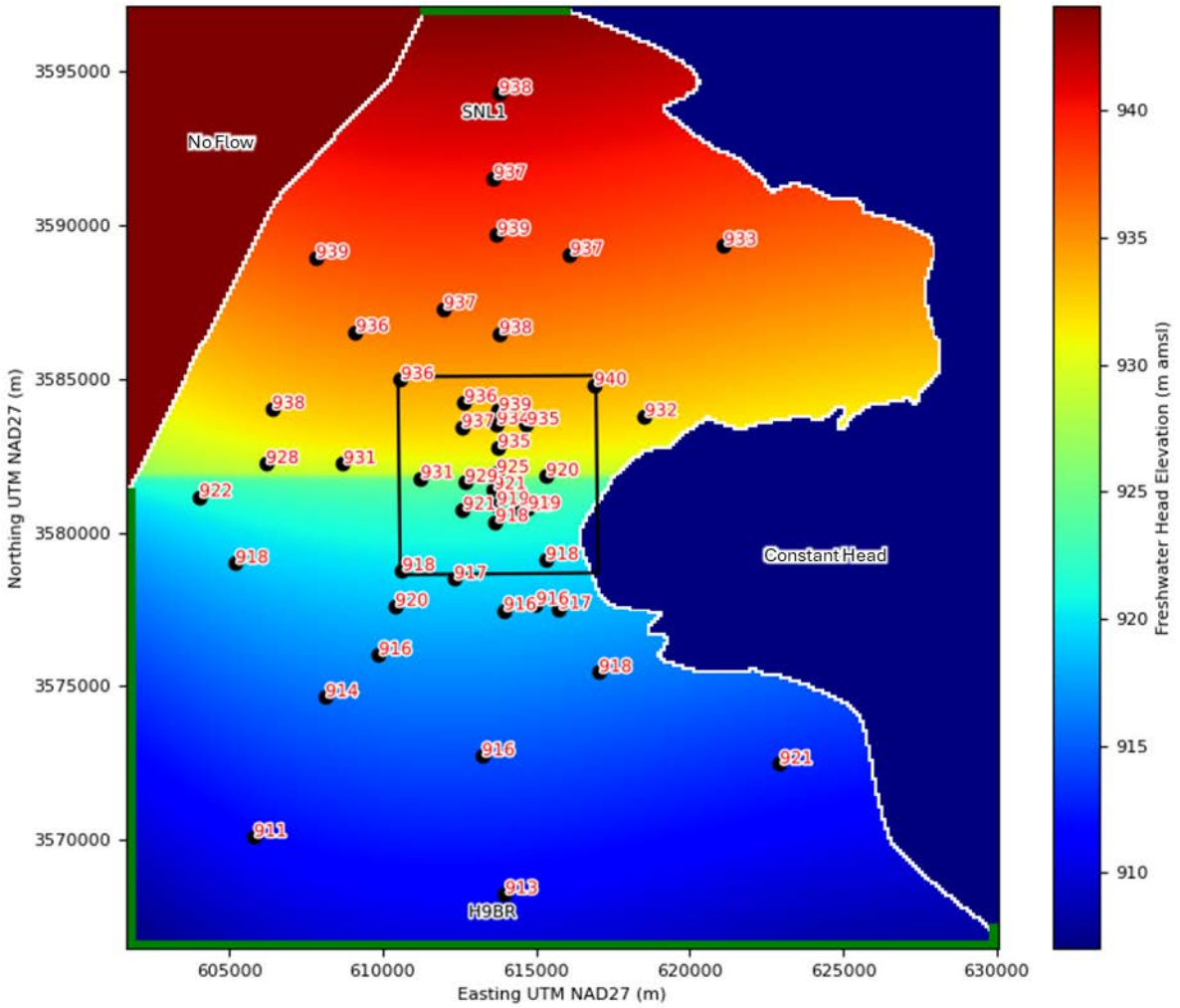


Figure TFIELD-19. Culebra Model Domain Showing Constant-Head Boundaries (Green Lines) and Initial Hydraulic Heads used in the Model Calibration. Hydraulic Heads are Assumed to Represent Steady-State Conditions during the Calibration. Red Numbers are Observed Hydraulic Heads.

Table TFIELD-10. Coefficients derived by fitting the multivariate equation (Equation TFIELD.10) to the observed hydraulic heads and to assign Boundary Conditions

Parameter	Value
a	926.804
b	8.412
c	1.636
d	1.040
e	1.305
f	-1.389
p	0.291

TFIELD-5.2.8.2 Initial Head

Initial heads are derived from equation TFIELD-10. Previous and current observations indicate that groundwater flow in the Culebra, is generally from north to south (Beauheim and Holt 1990; Davies 1989). Consistent with this general flow direction, the equation TFIELD-10 was formulated to keep the head value at the northern boundary above the measured head at SNL-1 and the head values at the southern boundary below the measured heads at well H-9bR.

Figure TFIELD-19 shows surface derived from the Equation (TFIELD.10). Equivalent freshwater heads derived from head measurements in 47 monitoring wells are labeled in red. The inactive zone, delineated by a no-flow boundary to the east is shown as brick-red cells. Constant head cells east of the halite margin (dark blue region) were instead set to land surface elevation.

TFIELD-5.2.9 Observations and Residuals

The observations (steady-state freshwater heads and pumping test drawdowns) used as calibration targets for PEST are summarized in Section TFIELD-5.1. Residuals are calculated as the difference between measured and model-generated freshwater heads or drawdowns by PEST. Two sets of residuals were calculated. Actual residuals are the differences between the simulated and observed value and measured residuals including noise representing measurement and model error, were calculated.

TFIELD-5.2.10 MODFLOW Numerical Model

With the parameter framework, initial conditions, and boundary conditions defined, the next step is to calibrate the T-fields to observed hydraulic responses. Calibration requires two components: (1) a forward model that simulates groundwater heads and drawdowns for a given set of hydraulic parameters, and (2) an inverse modeling tool that compares those

simulated values to observations and adjusts parameters to improve the match. For CRA-2026, the forward model is provided by MODFLOW 6 (MF6), the U.S. Geological Survey groundwater-flow code (Hughes et al., 2017). Both steady-state and transient Culebra flow models were developed using MF6, building directly on the MODFLOW-2000 models used for CRA-2019 (Bowman et al. 2023).

The inverse modeling component is performed by PEST (White et al. 2020). The PEST code iteratively adjusts the parameter sets and evaluates the resulting MF6 simulations against measured heads and drawdowns. The following sections describe the calibration procedures, data used, and resulting parameter estimates.

TFIELD-5.3 Calibration Process

The PEST calibration followed a process of using a forward model with adjustable parameters to fit observation data. The goodness of fit is based upon a measurement of model results against observation data to calculate an objective function that then iteratively update the adjustable parameters to minimize the objective function. During each iteration of the calibration, PEST perturbs the parameters to be estimated (as described in Section TFIELD 5.2) and then executes the MF6 forward model. Internally, MF6 iterates to convergence for both steady state and transient simulations. Once MF6 meets its specified convergence tolerance and produces a complete set of simulated heads, PEST compares those simulated values to the observed heads and drawdowns to evaluate the effect of the parameter perturbations. Each forward model execution includes a steady-state simulation and 11 transient simulations. The transient simulations were initialized with the heads from the steady-state model and drawdown was matched against observations. The steady-state simulation was run first, followed by all of the transient simulations.

The calibration consisted of three components:

- A steady state flow model, in which simulated steady state heads were compared to steady state equivalent freshwater heads,
- A transient model of the Mills Ranch pumping event, in which simulated drawdown was compared to the observed drawdown response, and
- Ten additional transient models representing the multi well pumping tests, in which simulated drawdowns were compared to the drawdown measurements collected during each test.

In each PEST iteration, the base T-field was perturbed from the prior distribution to produce a posterior T-field that minimized the difference between the simulated and observed hydraulic heads using a regularized least squares approach.

The T-Field calibration process was executed on 10 cluster nodes, each with 20 processors utilizing the Slurm Workload Manager (Yoo et al. 2003). Out of the 1,000 base T-field realizations, 973 were successfully calibrated compared to only 200 in the last recalibration. Of

the 1,000 realizations, 27 were removed during calibration by the PEST quality-control filter, leaving 973 in the final ensemble. All forward model runs completed successfully; the filter excludes realizations whose objective function exceeds the ensemble mean by more than five standard deviations, removing poorly performing outliers (Bowman et al. 2023).

Selecting the best-calibrated realizations for additional analyses consisted of two steps. First, selecting the final PEST iteration. Second, identifying the subset of best fields from the complete ensemble. Each PEST iteration involves running the model for each realization using the parameter set updated at that stage.

PEST minimizes the objective function, which improves the sum of squared difference between observations and simulated results. However, because the underlying groundwater flow model is an imperfect representation of the physical system, this fit cannot be the only metric by which the model is deemed "calibrated". Overfitting the model to observations may result in oversmoothed parameter fields and increased bias from fitting to noise or other intrinsic errors. In practice, the process is halted when the per-iteration change in the objective function reduces significantly.

Figures TFIELD-20 to TFIELD-22 illustrate how the total objective function, as well as the objective functions for the equivalent freshwater heads and pumping-test observations vary with each iteration. Figure TFIELD-20 shows that the mean objective function declines consistently in log space from iterations 2 to 5. Between iterations 5 and 6, the rate of improvement begins to flatten, with the inflection most evident in the freshwater heads observation group. This inflection is most pronounced in the objective function for only freshwater heads observation group. This diminishing improvement suggests that Iteration 5 represents a reasonable and defensible stopping point for the calibration.

The rationale for ending the PEST calibration prior to achieving the minimum total ϕ is to preserve variability in the ensemble of calibrated realizations. This is because the initial uncalibrated base T-fields represents the maximum plausible uncertainty in the hydraulic conductivity field. As calibration proceeds, assimilating head observations reduces this uncertainty. However, continuing the iterations too far can force the model to overfit the data, thereby introducing bias and suppressing variability in the resulting T-fields. Stopping calibration before achieving the minimum $\boldsymbol{\phi}$ is a balance between reducing uncertainty through data assimilation and maintaining sufficient ensemble variance to avoid overfitting a model that would not accurately replicate observed data.

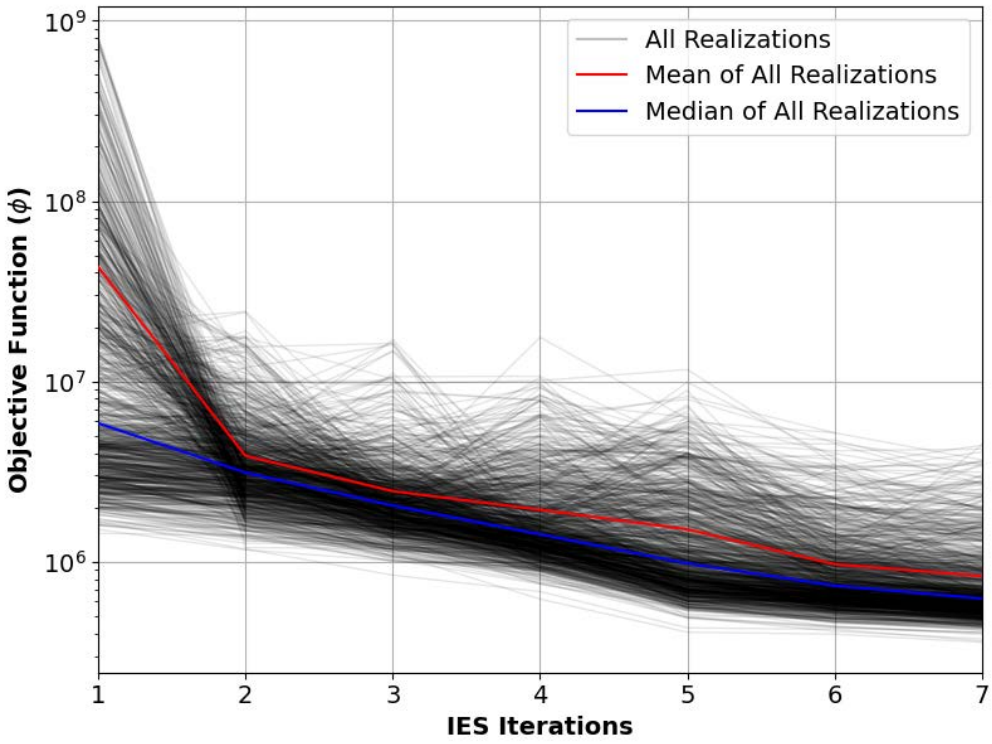


Figure TFIELD-20. Evolution of the Total Objective Function with IES Iteration for 973 Calibrations

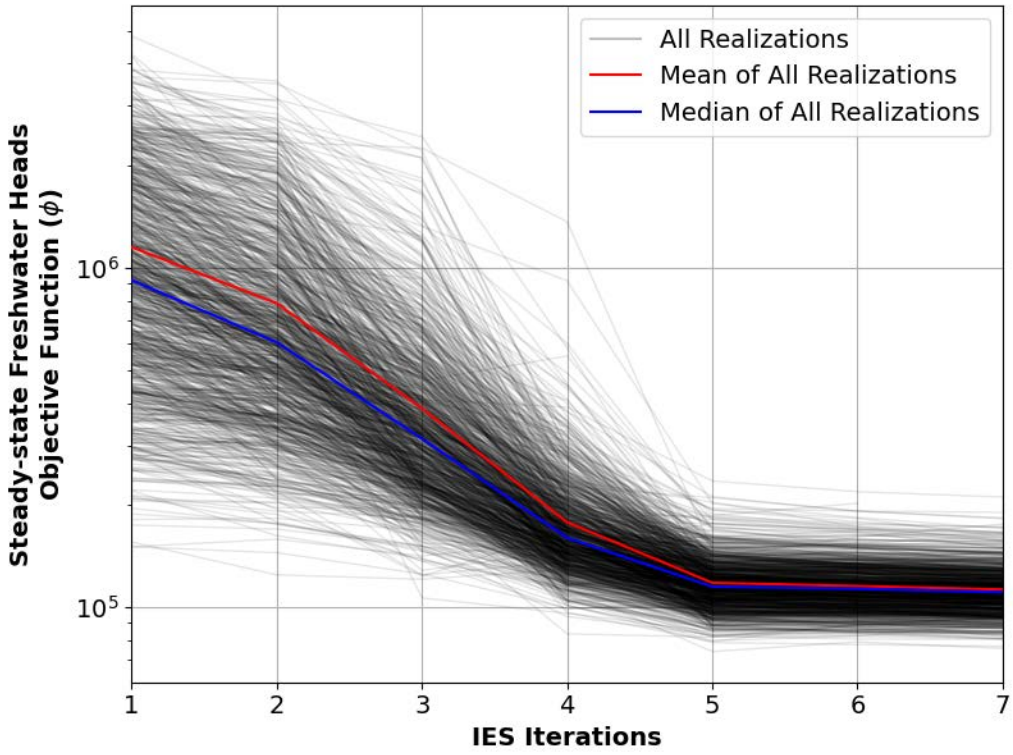


Figure TFIELD-21. Evolution of the Objective Function with IES Iteration for the Steady-state Freshwater Heads Observation Group for 973 Calibrations

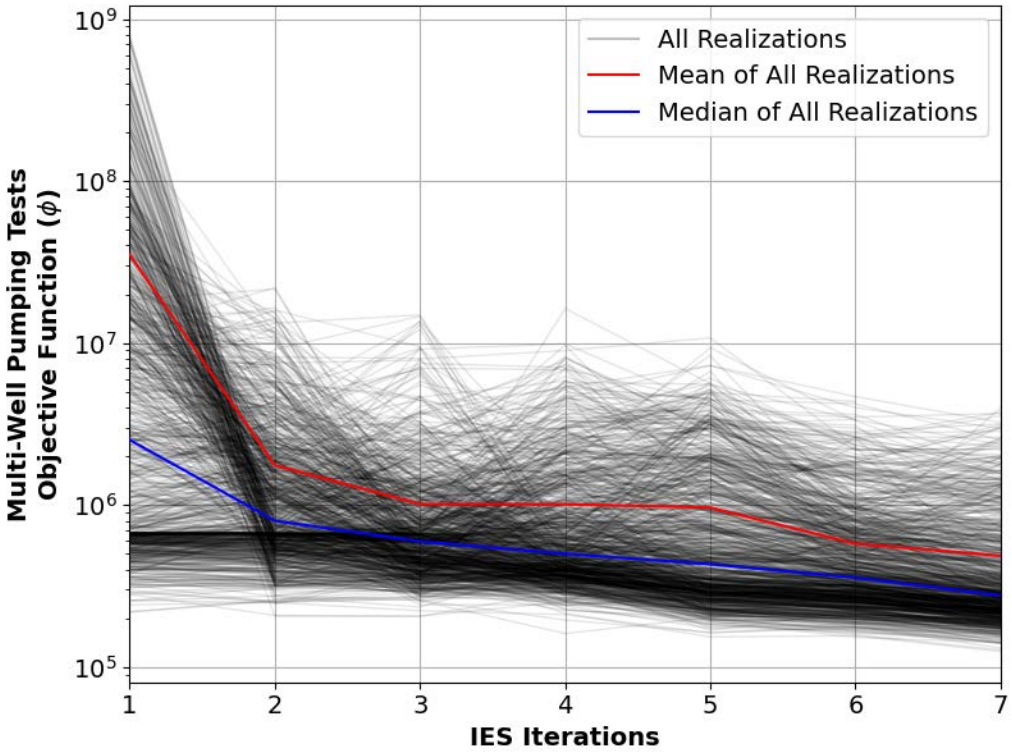


Figure TFIELD-22. Evolution of the Total Objective Function with IES Iteration for the Multi-Well Pumping Tests for 973 Calibrations

TFIELD-5.3.1 Selection of Best-Calibrated Fields

To support steady state flow and solute transport analyses in WIPP PA, the 100 best realizations were chosen by comparing the three general observation groups: steady-state freshwater heads, multi-well pumping tests, and the Mills Ranch pumping event. To identify the best realizations, the objective function for each observation group was normalized between 0 and 1 at each iteration. Normalization yielded a scaled value for each of the three general observation types for each realization. Each realization can therefore be represented as a point in a 3D space defined by the normalized objective function components. The 100 representative realizations were selected as with the smallest Euclidean distance to the origin (0, 0, 0), which corresponds to the lowest combined misfit across all three observation groups (Figure TFIELD-23). Figure TFIELD-24 shows un-normalized general observation groups for the normalized objective function. The gray results show the final 973 realization ensemble, while the blue results indicate the 100 selected best realizations. The final 100 selected realizations maintain the same identification number from the base T-fields and are listed in Table TFIELD-11. Figure TFIELD-24 shows that the selected realizations (blue points) consistently occupy the low-misfit regions of the objective-function space for all three observation groups. Across the scatterplots, the blue points cluster toward the lower-left portions of each axis pair, indicating simultaneously low misfit for paired observation types. The accompanying histograms show that the selected realizations fall within the lowest portions of the misfit distributions for all three groups. Taken together, these plots demonstrate that the 100 selected realizations

provide the best combined fit to steady-state heads, multi-well pumping-test responses, and the Mills Ranch pumping event.

Table TFIELD-11. 100 Selected T-Field Realizations

5	150	320	434	511	590	660	728	807	856
12	173	325	441	517	614	664	729	808	869
27	194	338	455	519	619	672	736	810	892
71	213	344	456	530	620	675	737	811	895
73	219	345	473	531	638	700	744	820	909
92	247	351	487	536	641	705	759	822	914
97	255	358	488	541	642	713	760	825	929
119	269	362	492	563	649	714	780	826	970
129	298	393	494	570	651	723	786	837	983
146	304	430	496	572	654	724	803	841	988

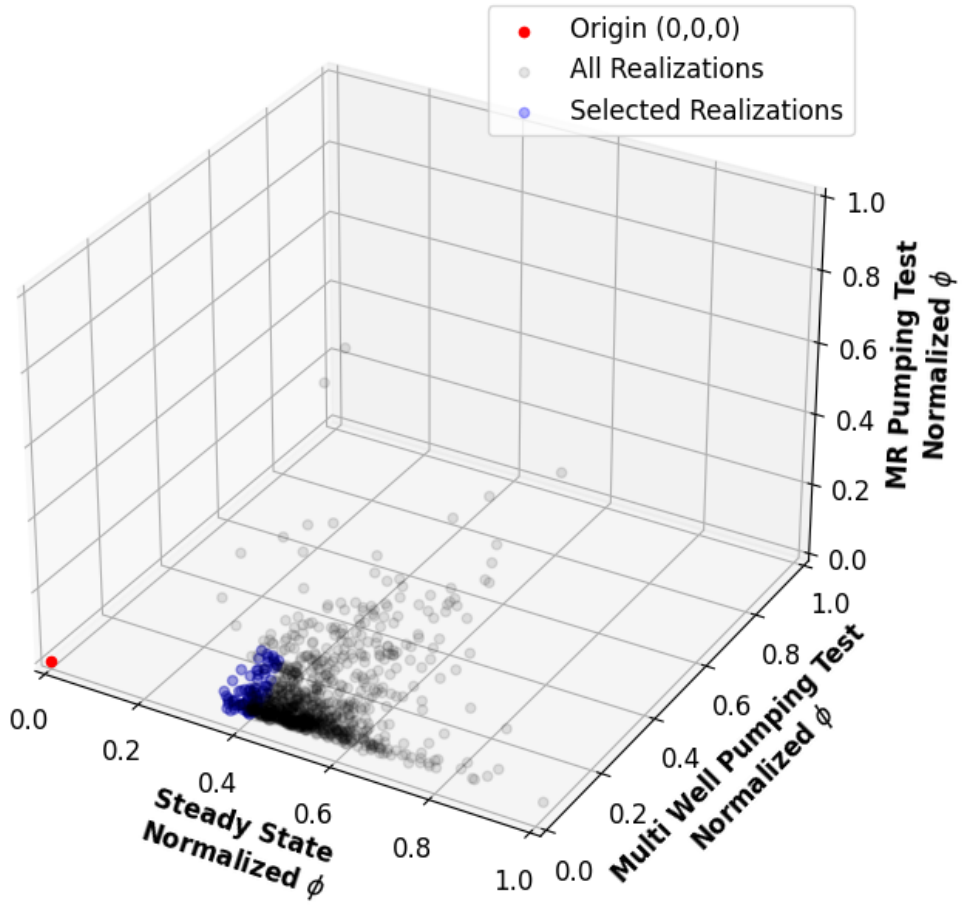


Figure TFIELD-23. Normalized Objective Function for 973 Observation Groups at Iteration 5

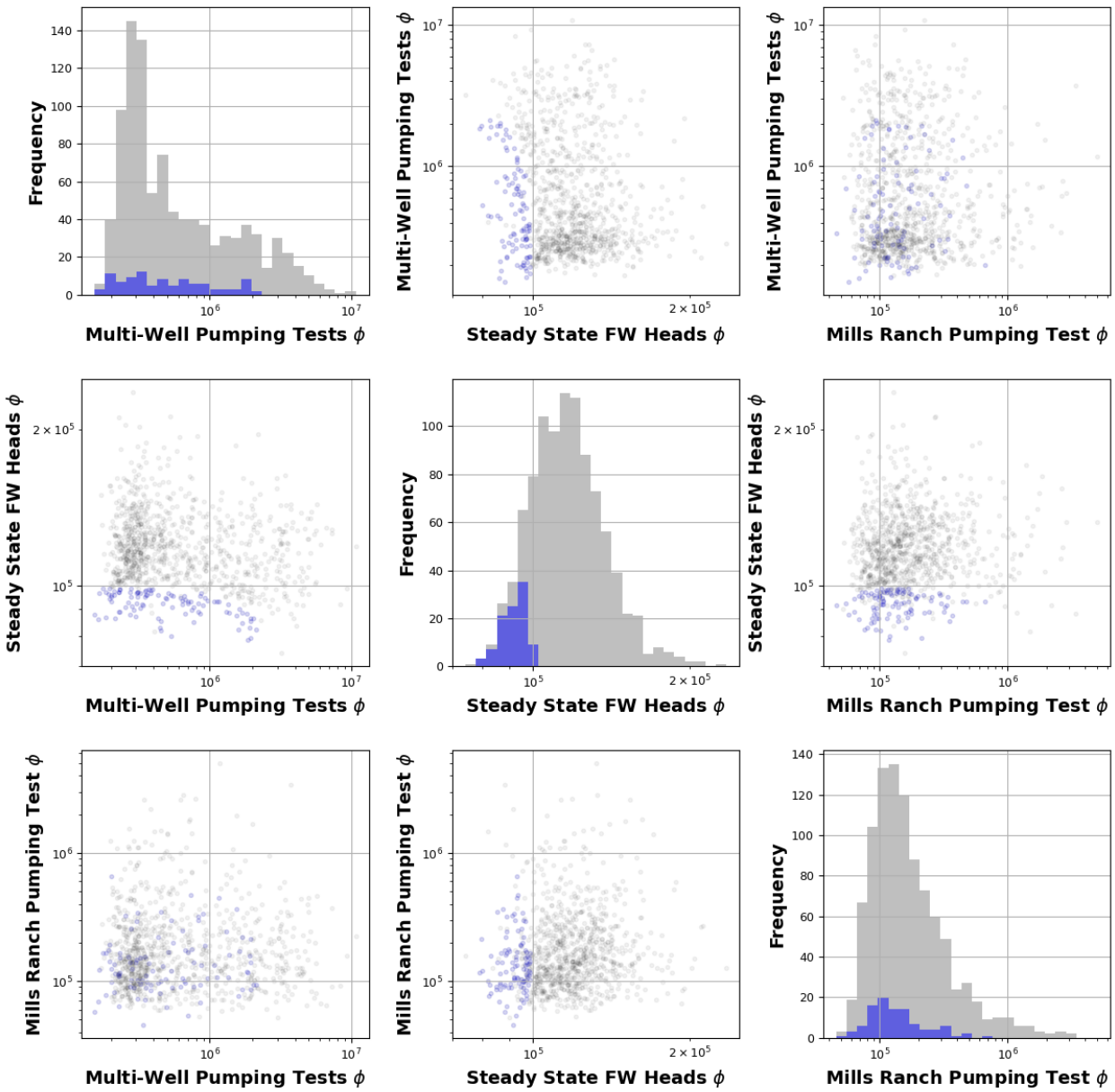


Figure TFIELD-24. Histograms and Scatter Plots of the Normalized Objective Function for Primary Observation Groups. Gray symbols are All Calibrated Realizations Plotted in Normalized Objective-Function Space, the Blue Symbols are the 100 Realizations Closest to (0,0,0), i.e., the Best Fit Across All Three Observation Groups, and the Red Symbol is the Origin, Representing the Ideal Perfect Fit.

TFIELD-5.4 Calibrated Results

The results of the modeling workflow described above demonstrate that the PEST calibration successfully assimilated the full range of steady-state equivalent freshwater heads and

transient drawdown responses from the 11 pumping tests (Figures TFIELD-23 and TFIELD-24). The assimilated data conditioned the initial T-field geostatistical realizations to yield the parameter fields that best reproduce the measured hydraulic responses. The results related to simulating each general observation type are discussed in detail below. Overall, the history-matching procedure produced coherent and geologically plausible parameter adjustments that enabled the flow models to reproduce the observed steady state heads and transient pumping test drawdowns with appropriate fidelity.

TFIELD-5.4.1 Steady-state Freshwater Heads

Overall, the calibrated steady-state equivalent freshwater heads show good agreement with observations. The best fits occur for wells located within or near the Land Withdrawal Boundary (LWB), where observational data are densest. Wells near the edges of the model domain exhibit somewhat larger residuals, likely a reflection of their proximity to boundary conditions and the reduced data constraints in those areas. Histograms of the simulated freshwater head distributions for each of the 47 monitoring wells, along with the noise applied to each observation are given in Bowman et al. (2023). Random measurement noise was taken from a normal distribution with the observed value as the mean of the distribution. The standard deviation of the observations was used as standard deviation of the measurement noise distribution. Figure TFIELD-25 shows the median steady-state head calculated from the 100 selected realizations, plotted as contours across the model domain, together with the observed steady-state freshwater heads (red numbers) at the monitoring wells (black symbols). The calibrated steady-state model reproduces the major structural features of the observed potentiometric surface in the Culebra. The median simulated steady-state head contours depict a regional gradient that declines from the northwest toward the southeast, consistent with the established hydrogeologic flow direction (Beauheim and Holt, 1990; Davies, 1989). Across most of the LWA boundary, the observed steady state freshwater heads (red labels) align closely with the simulated heads (black contours), indicating generally small residuals and good agreement between model and measurements. Overall, this result shows that the calibrated model captures both the magnitude and shape of the potentiometric surface with appropriate fidelity.

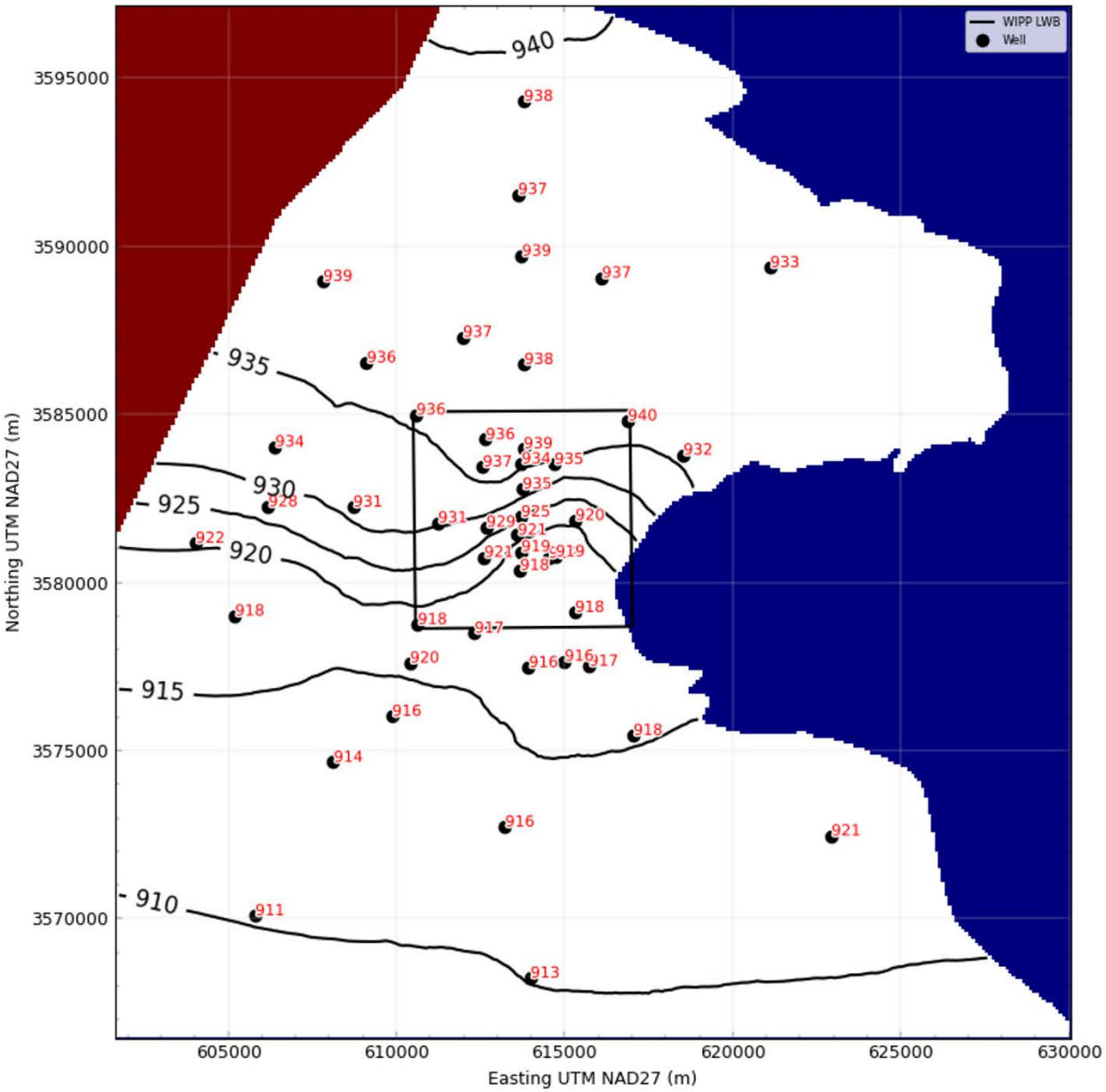


Figure TFIELD-25. Contour of Median Simulated Steady-state Freshwater Head (m-AMSL) in Black (5-m contour interval). Contours are Generated by Linear Interpolation Using Simulated Heads from the MF6 Regular Grid. Mean, Median, or Mode (Depending on Distribution) of Observed Steady-state Freshwater Heads for Each Well are in Red.

TFIELD-5.4.2 Simulated Multi-Well Pumping Tests

The 100 selected realizations generally reproduced the observed spatial and temporal drawdown patterns for each multi-well pumping test. Bowman et al. (2023) present detailed comparisons of observed and simulated drawdowns for the ten tests, illustrating the

distribution of simulated responses across the 100 selected realizations using violin plots. These comparisons demonstrate that the calibrated parameter fields capture the main features of the drawdown behavior recorded during each test. A violin plot shows the full distribution of simulated drawdowns across the 100 selected realizations, including the median, range, and the density of values, providing a clear visualization of uncertainty and variability.

TFIELD-5.4.3 Simulated Mills Ranch Pumping Event

As previously discussed, the Mills Ranch pumping event imposed a large hydraulic stress on the Culebra, producing a wide spatial distribution and large magnitude drawdown. Because of the strength and diagnostic value of this signal, the associated observations were assigned a relatively high weight in the objective function, ensuring an important role during history matching. Many numerical experiments were performed to explore the effect of varying the percentage contribution of each observation group to improve history-matching. This ultimately led to splitting the objective function evenly amongst the four general observation groups (25% each), which yielded results that best fit the conceptual understanding of the system and gave equal importance to each general observation type. The estimated groundwater-extraction rates derived from the calibration are consistent with prior expectations and within a hydraulically plausible range.

Figure TFIELD-26 is a violin plot showing the distribution of pumping rates for each pumping interval across the 100 selected realizations. The width of each violin represents the duration of the corresponding pumping interval. The results show that pumping rates before the winter 2015-2016 recovery period were, on average, higher than the pumping rates estimated for the post-recovery period.

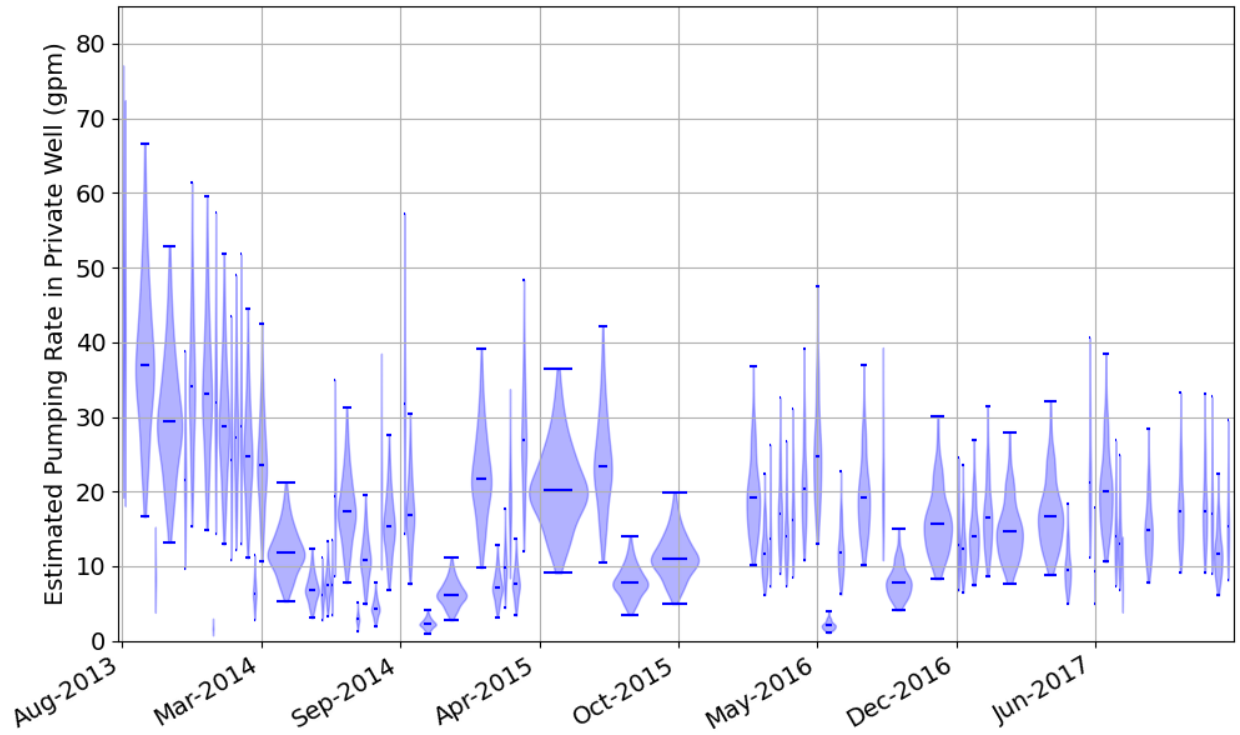


Figure TFIELD-26. Distributions of Estimated Mills Ranch Pumping Rates for each pumping Interval Across the 100 Selected Realizations, shown as Violin Plots. The Width of Each Violin Represents the Duration of the Pumping Interval, and the Vertical Spread Indicates the Variability in Estimated Pumping Rates (gpm).

TFIELD-5.4.4 Final Transmissivity Fields

In general, the estimated transmissivity fields for the 100 selected realizations present a spatially coherent and expected pattern of heterogeneity. Across the domain, the calibrated fields generally reproduce the single-well transmissivity estimates within the measurement noise caused by scaling effects associated with mapping well test values onto the model grid (see Appendix A section 7.5 in Bowman et al. 2023). The figures shown in this section describe transmissivity derived from the hydraulic conductivity (m/s) used by MF6. These representations provide a clear view of the calibrated spatial variability in transmissivity and its directional components across the Culebra.

Figure TFIELD-27 shows the mean transmissivity across the 100 selected realizations, whereas Figure TFIELD-28 presents the corresponding standard deviation. Areas where mean transmissivity is low and variability is also low indicate locations where the model consistently predicts low transmissivity with relatively high confidence. This pattern is evident in the eastern portion of the domain, where both the mean transmissivity and its variability are low. In contrast, the standard deviation map (Figure TFIELD-28) shows that Zone 1 exhibits the most variability overall, as expected given its broader range of plausible transmissivity values.

However, the southwestern portion of the LWA boundary stands out as an area reduced variability relative to rest of this zone. This decrease in variability is due to the larger number of observations in this area, where both steady-state heads and Mills Ranch drawdown responses provide strong constraints on transmissivity. Small “bullseyes” of low variability also show up in this figure; they coincide with areas where transmissivity is known (from aquifer testing) or there is data (hydraulic diffusivity, presence/absence of halite, presence/absence of gypsum) to constrain transmissivity values.

Figure TFIELD-29 and Figure TFIELD-30 show the number of high-T cells in iteration 0 and Iteration 5 for the 100 selected realizations. The cutoff value for "high-T" was set in Hart et al. (2009) to be the bulk transmissivity, which is the average $\log_{10}$ transmissivity values of all cells in a given zone or zones, value of the base fields of -5.41 $\log_{10}$ m^2/s. Figure TFIELD-31 shows the change from the number of high-T cells in the prior to low-T cells in Iteration 5, and Figure TFIELD-32 shows the reverse. This analysis was calculated for each cell.

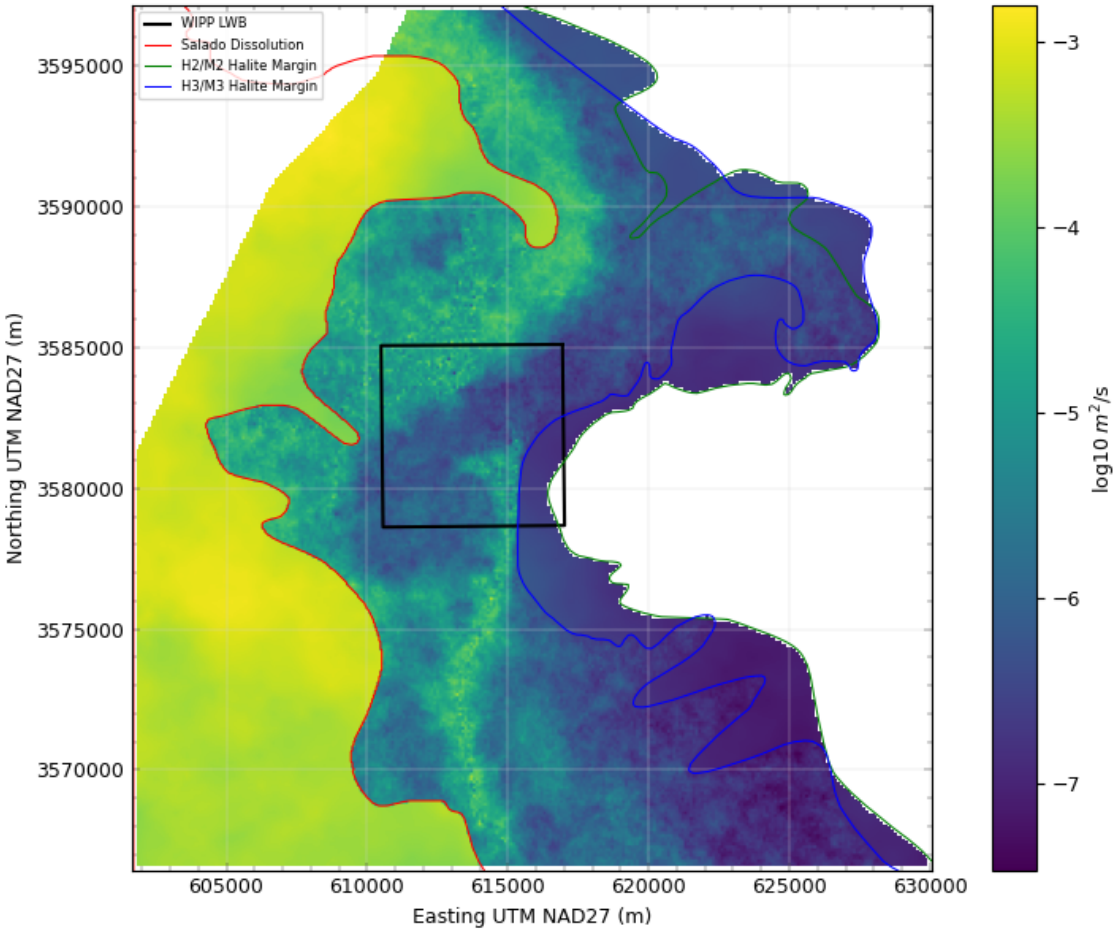


Figure TFIELD-27. Mean Transmissivity for 100 Selected Realizations at Calibration Iteration 5

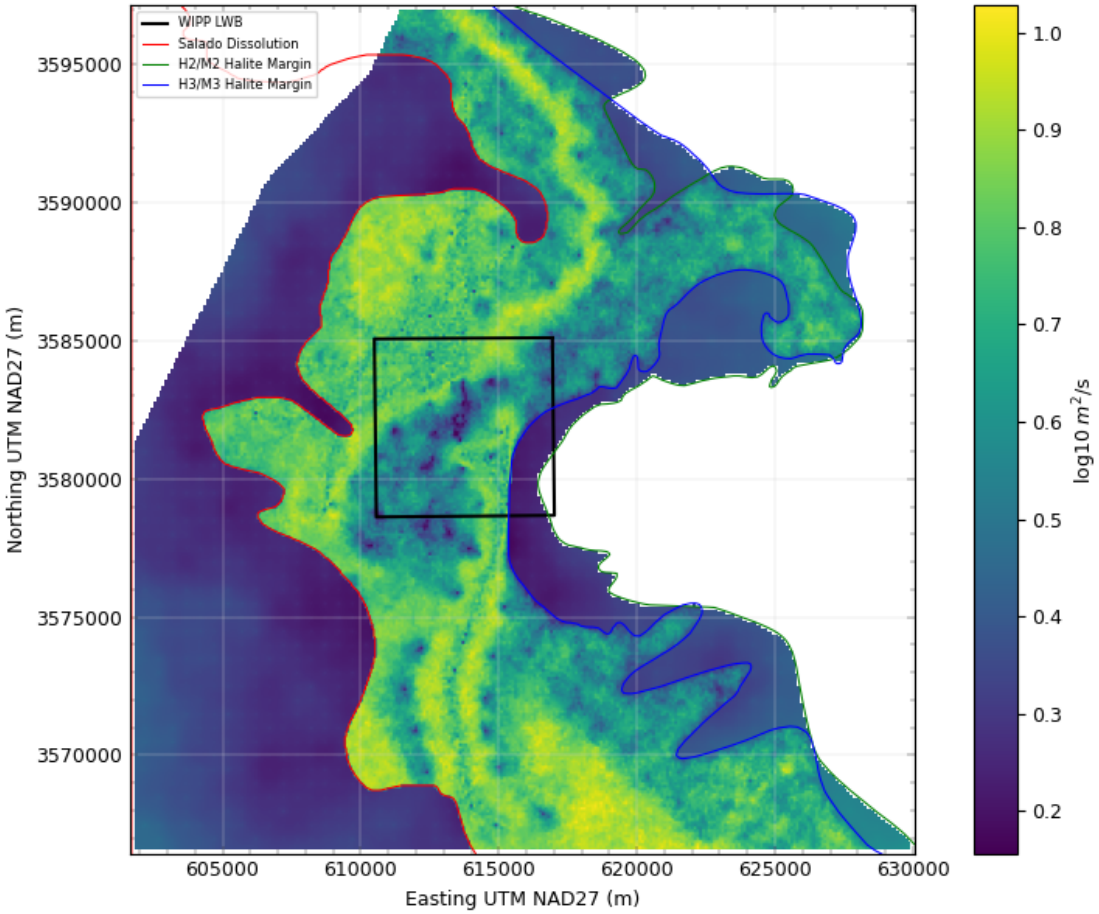


Figure TFIELD-28. Standard Deviation of Transmissivity Across 100 Selected Realizations at Calibration Iteration 5

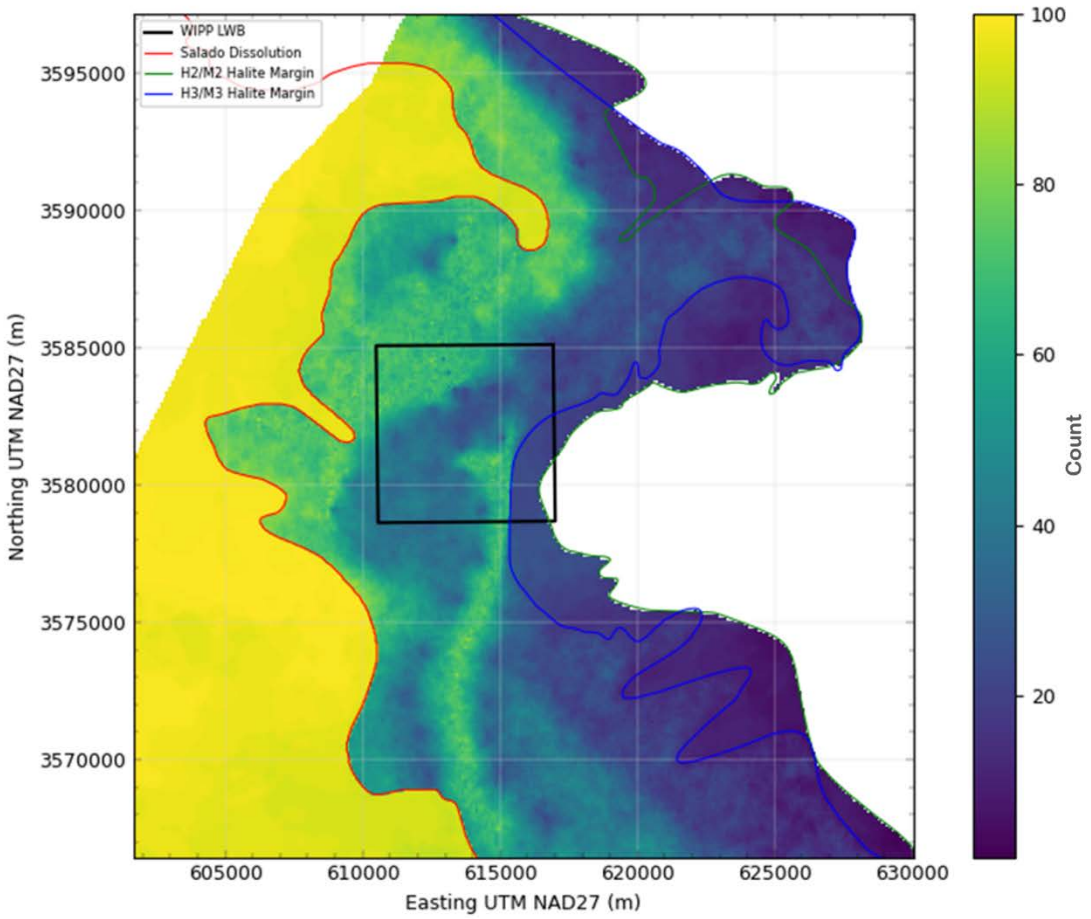


Figure TFIELD-29. Count of High-T Zone Membership at Calibration Iteration 0 (prior)

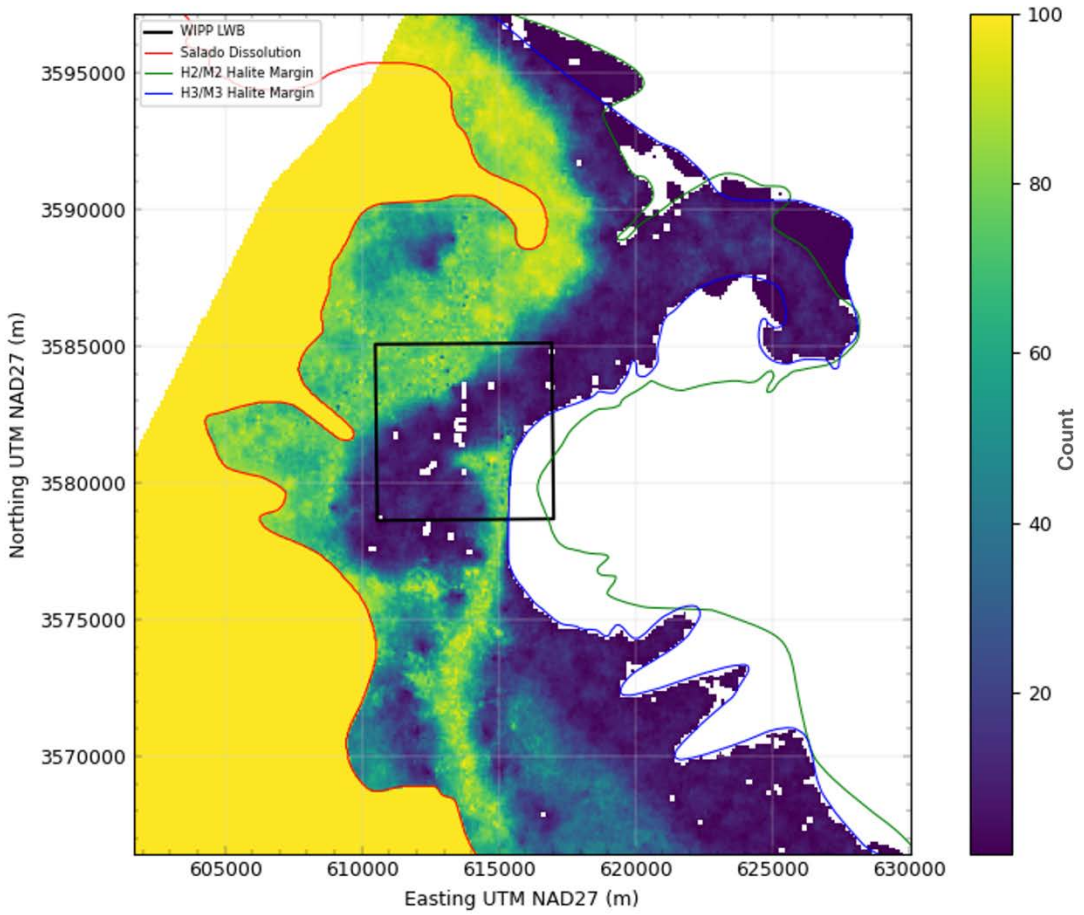


Figure TFIELD-30. Count of High-T Zone Membership at Calibration Iteration 5

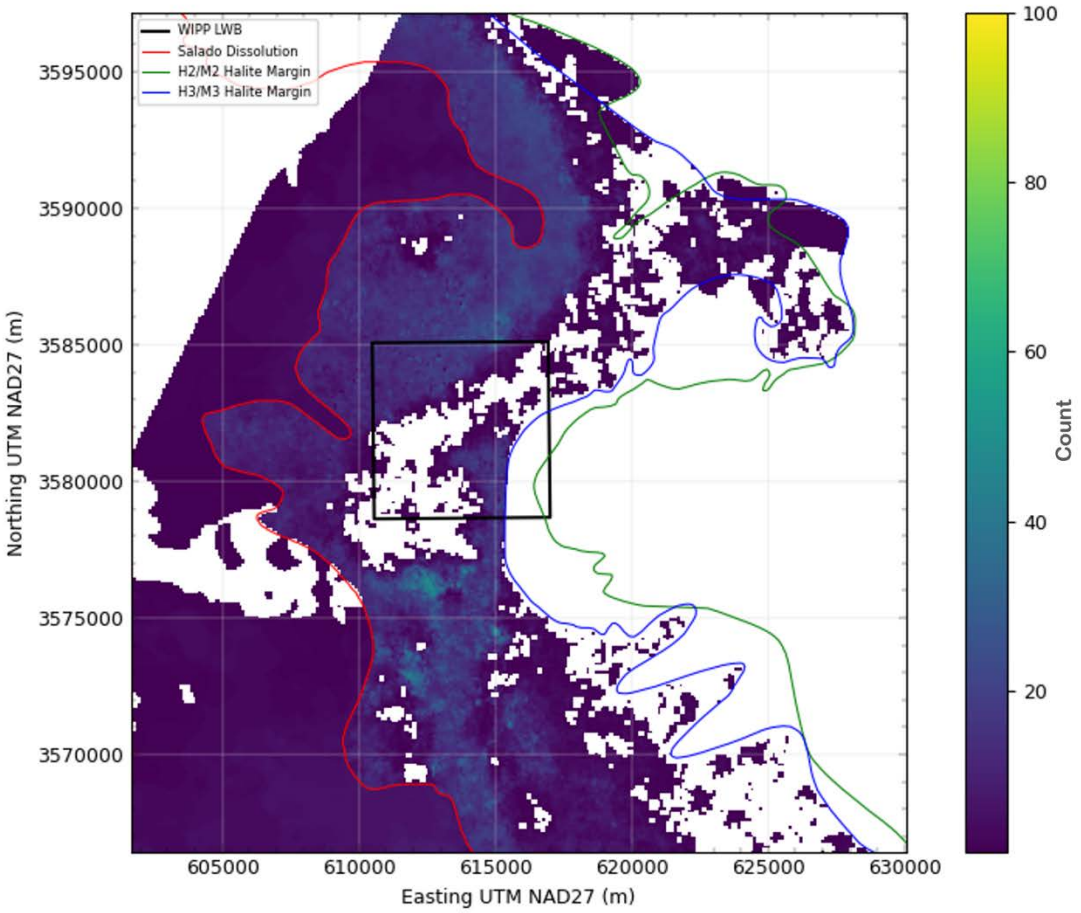


Figure TFIELD-31. Count of T Fields with Change from Low-T to High-T Between Calibration Iterations 0 to 5

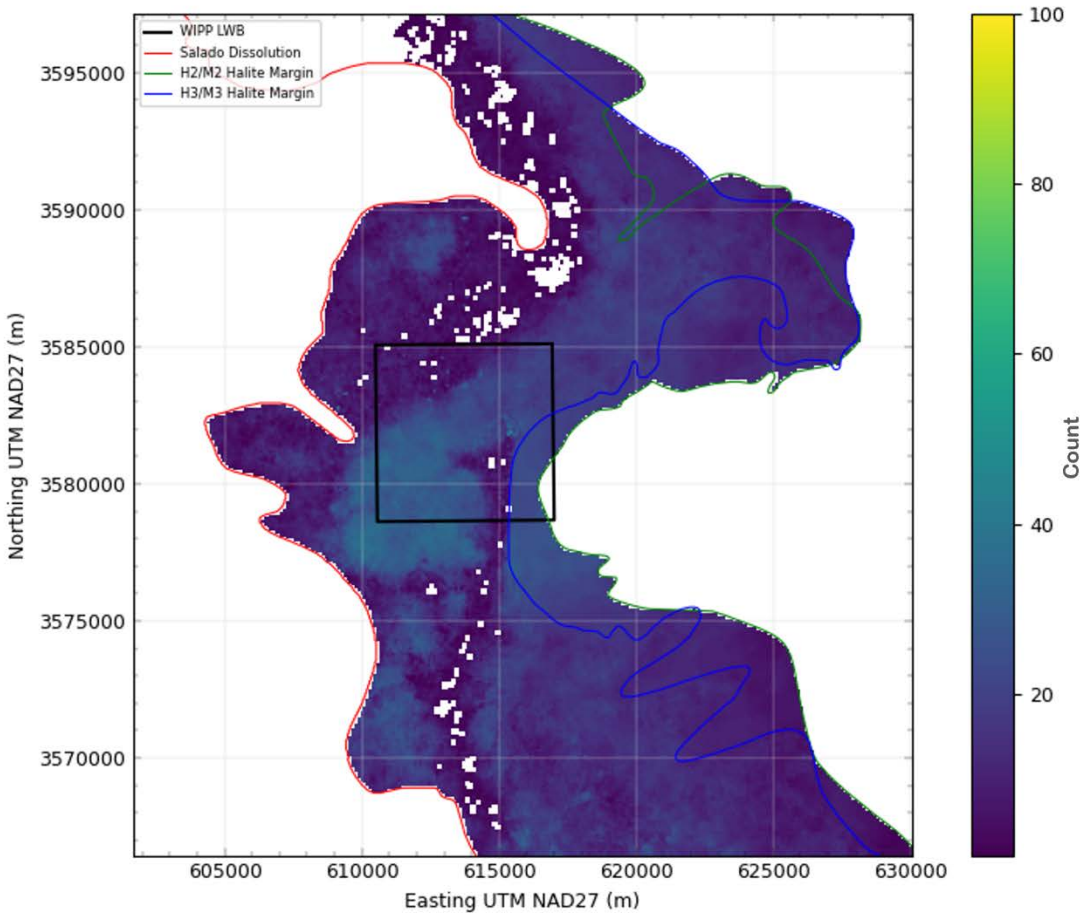


Figure TFIELD-32. Count of T Fields with Change from High-T to Low-T Between Calibration Iterations 0 to 5

TFIELD-5.4.5 Final Storativity Values

The mean and standard deviation of the 100 selected realizations for storativity are presented in Figure TFIELD-33 and Figure TFIELD-34, respectively. The mean storativity values indicate that the overall storativity values in the confined, transitional, and unconfined zones did not change much from the initial values (Figure TFIELD-33). The confinement transition zone shows the largest variability of storativity across the 100 realizations, while the confined portion maintains the smallest variability across realizations (Figure TFIELD-34).

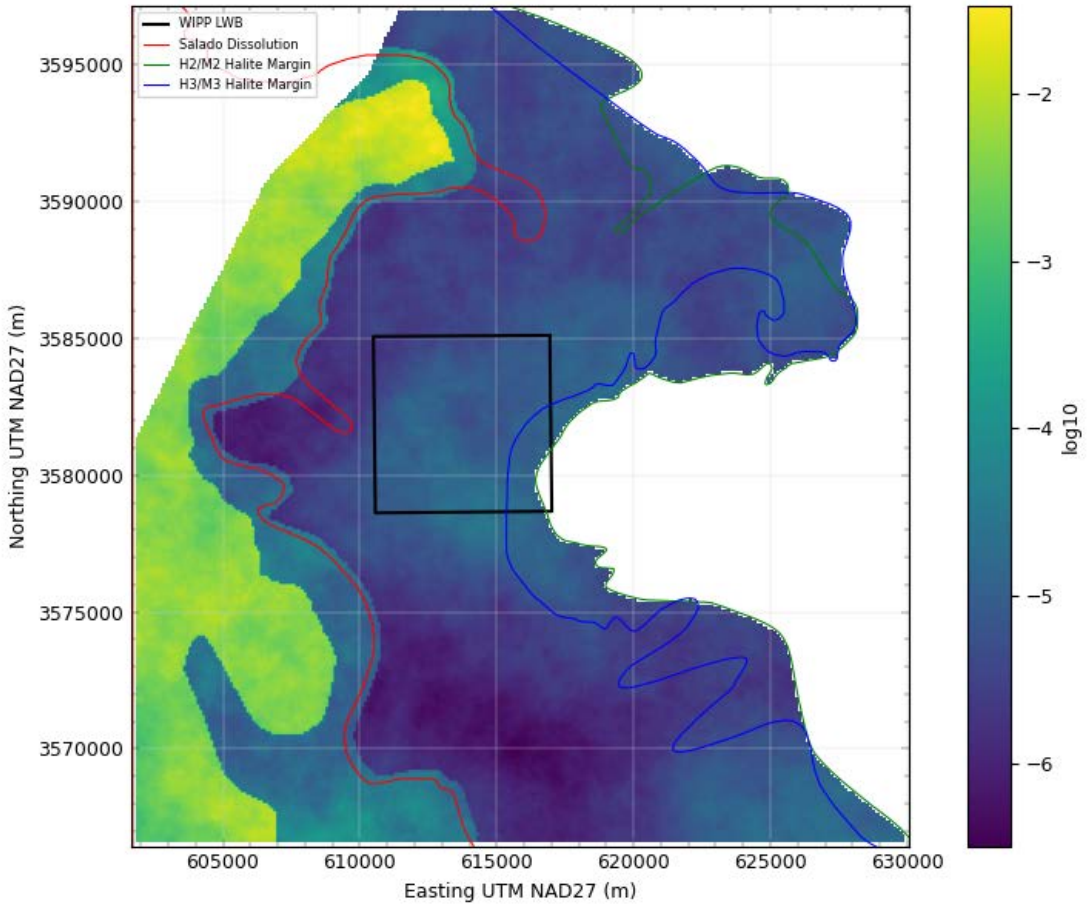


Figure TFIELD-33. Mean Storativity Values Across 100 Selected Realizations at Iteration 5

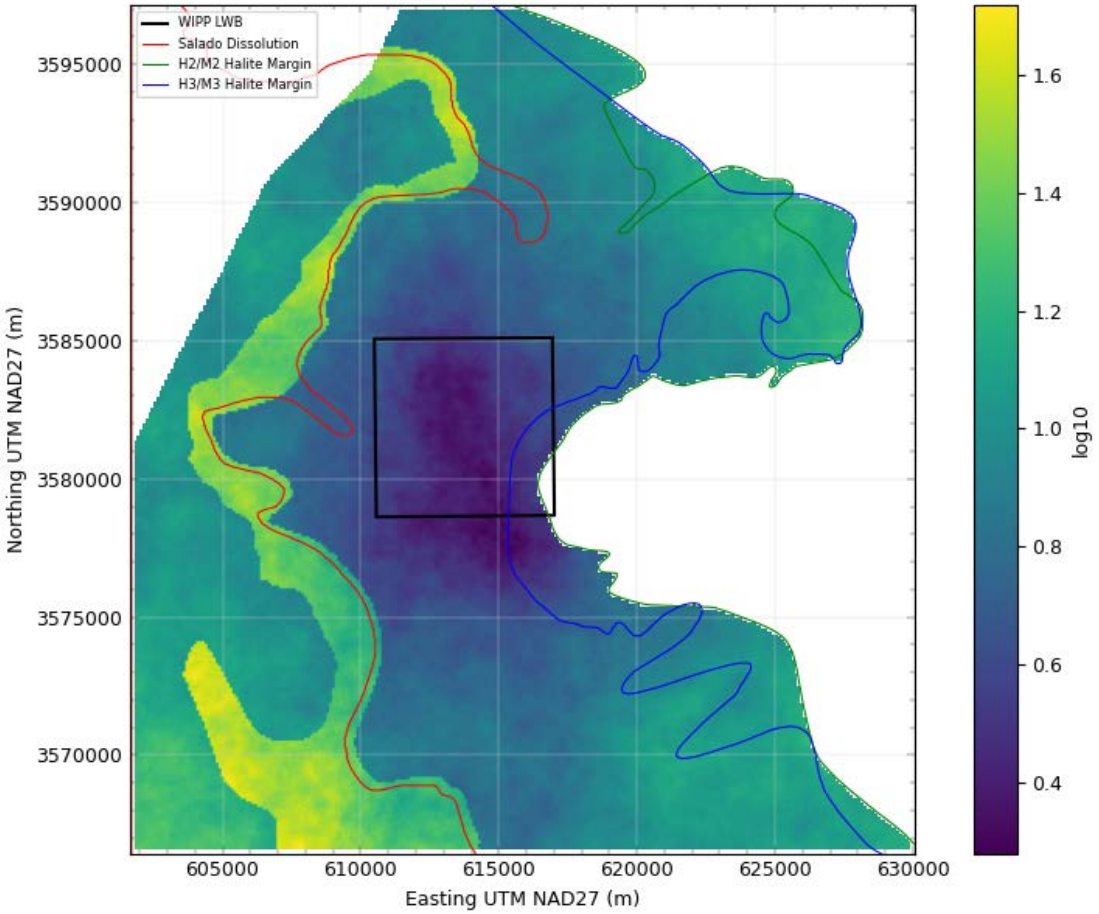


Figure TFIELD-34. Standard Deviation of Storativity Values Across 100 Selected Realizations at Iteration 5

TFIELD-5.4.6 Final Anisotropy Ratios

The mean and standard deviation of horizontal anisotropy ratio for the final 100 selected realizations are presented in Figure TFIELD-35 and Figure TFIELD-36, respectively. In general, positive $\log_{10}$ horizontal anisotropy ratios indicate a larger longitudinal (north-south) transmissivity, whereas negative $\log_{10}$ anisotropy ratios indicate larger transverse (east-west) transmissivity. Figure TFIELD-35 shows that in the high-T area (zone 1), there is generally a larger longitudinal transmissivity. Figure TFIELD-36 shows the lowest standard deviation values are produced inside the LWB.

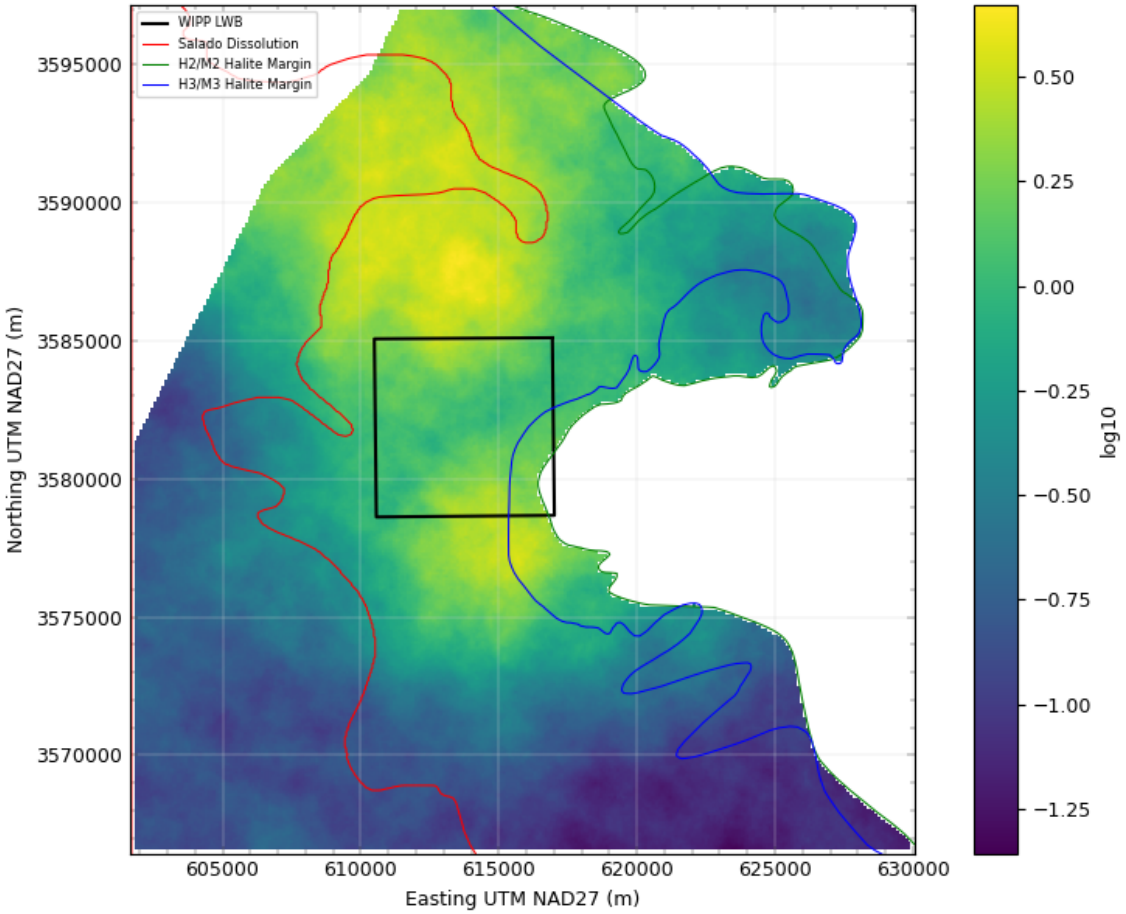


Figure TFIELD-35. Mean Anisotropy Values Across 100 Selected Realizations at Iteration 5

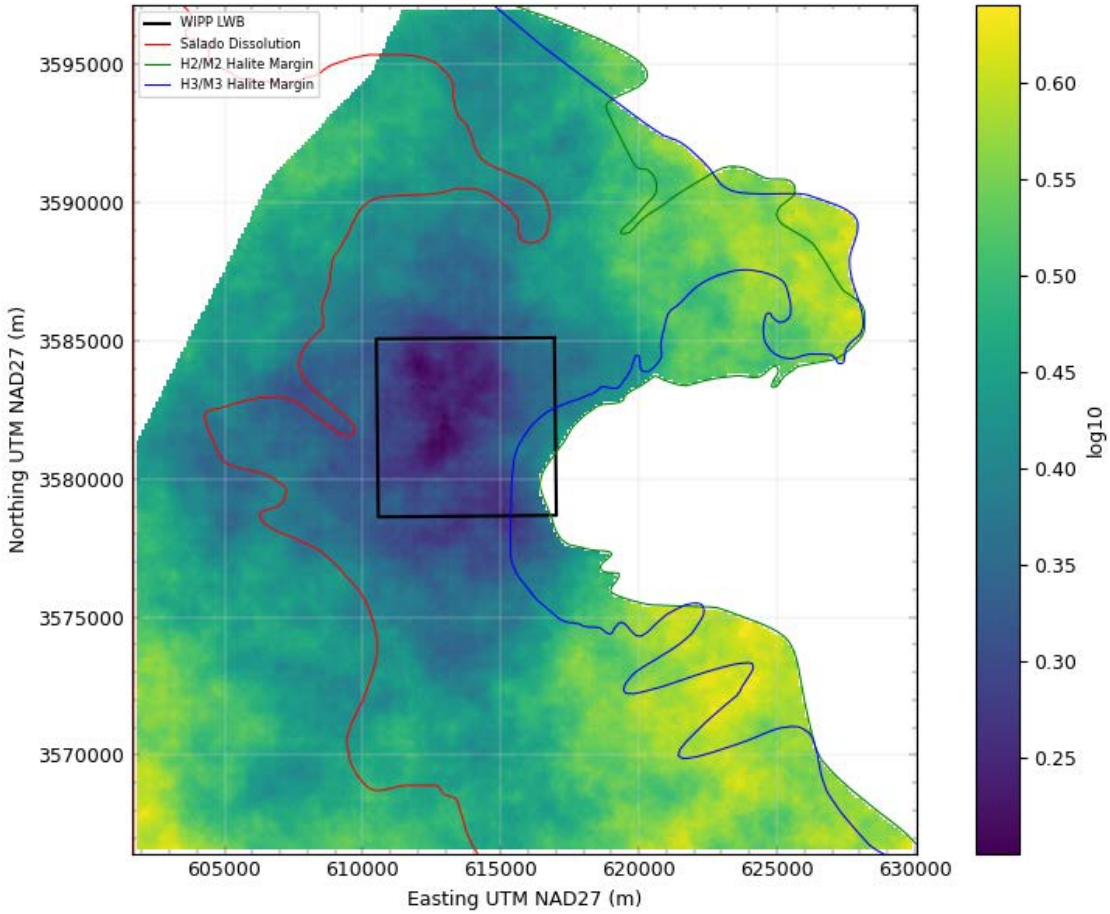


Figure TFIELD-36. Standard Deviation of Anisotropy Values Across 100 Selected Realizations at Iteration 5

TFIELD-5.4.7 Final Recharge Values

The final recharge values for the final 100 selected realizations had a maximum value of 10^{-10} m/s (3.2 millimeters per year [mm/yr]), as shown in Figure TFIELD-36. This is approximately 1% of the normal annual precipitation at the WIPP site (330.2 mm/yr), within the 0.1–5% of precipitation range reported for arid and semiarid regions (Scanlon et al. 2006). This maximum corresponds to the upper bound permitted during calibration and occurs only in cells along the groundwater divide line; recharge in all other model cells was fixed at effectively zero. Compared to other parameters, recharge was not allowed to vary as much (10^{-10} - 10^{-9} m/s), as there is minimal actual recharge to the Culebra. Figure TFIELD-37 shows maps of the maximum and standard deviation of recharge across the 100 selected realizations, where white cells represent no recharge. Recharge values are most constrained in the south of the line of recharge cells, further from the boundary of the model and a sparser density of data.

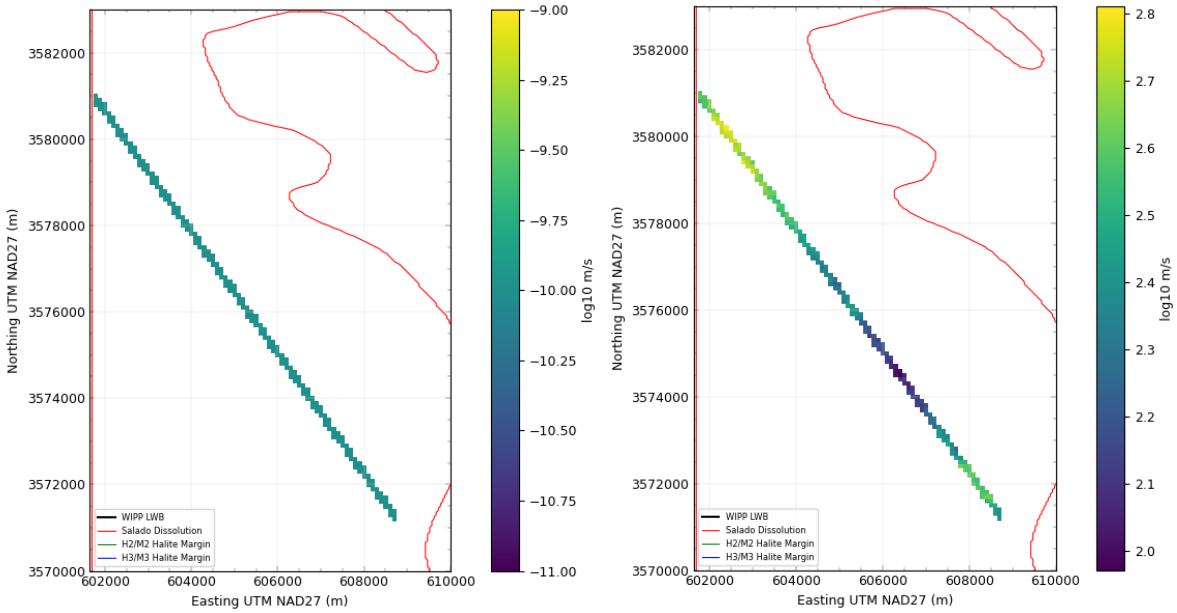


Figure TFIELD-37. Maximum Recharge (Left) and Standard Deviation (Right) Across 100 Selected Realizations at Iteration 5

TFIELD-5.4.8 Model Diagnostics

Three primary model diagnostic evaluations were conducted to assess the performance of the calibrated models: (1) steady-state head, matching, (2) transient pumping-test matching, and (3) comparison of estimated transmissivity to single-well test results. These diagnostics are illustrated for a representative well, H-19b0, which had both a steady state equivalent freshwater heads and participation in a multi-pad pumping test. Full diagnostic results for all model wells are provided in Bowman et al. (2023).

Figure TFIELD-38 presents a plot of the steady-state freshwater head distributions for well H-19b0 for the 100 selected realizations. Simulated heads were bi-linearly interpolated from the MF6 cell-center values to the well coordinates. For comparison, the observed head and the observation plus associated measurement noise are also shown. Figure TFILED-38 demonstrates that the posterior ensemble spans the observed values and is consistent with the expected observational uncertainty.

Figure TFIELD-39 presents a violin plot comparing the observed and simulated drawdown responses for the long-term multi-well pumping tests in which H-19b0 participated. Model-predicted drawdowns were bi-linearly interpolated in space and linearly interpolated in time to match the observation coordinates and time steps. The distribution of simulated responses reflects the variability across the calibrated realizations and illustrates the model's ability to capture the magnitude and timing of the observed drawdown signal.

Figure TFIELD-40 compares transmissivity values estimated from single-well formation performance tests at each observation well to the transmissivity predicted for the

corresponding MF6 grid cell. The 'observed' histogram represents samples drawn from a lognormal distribution with the mean at the best-estimate of transmissivity from the formation test and assuming a standard deviation of one-half log-cycle. The comparison demonstrates that the calibrated transmissivity fields are broadly consistent with the single-well test estimates while incorporating the expected measurement and scale uncertainty.

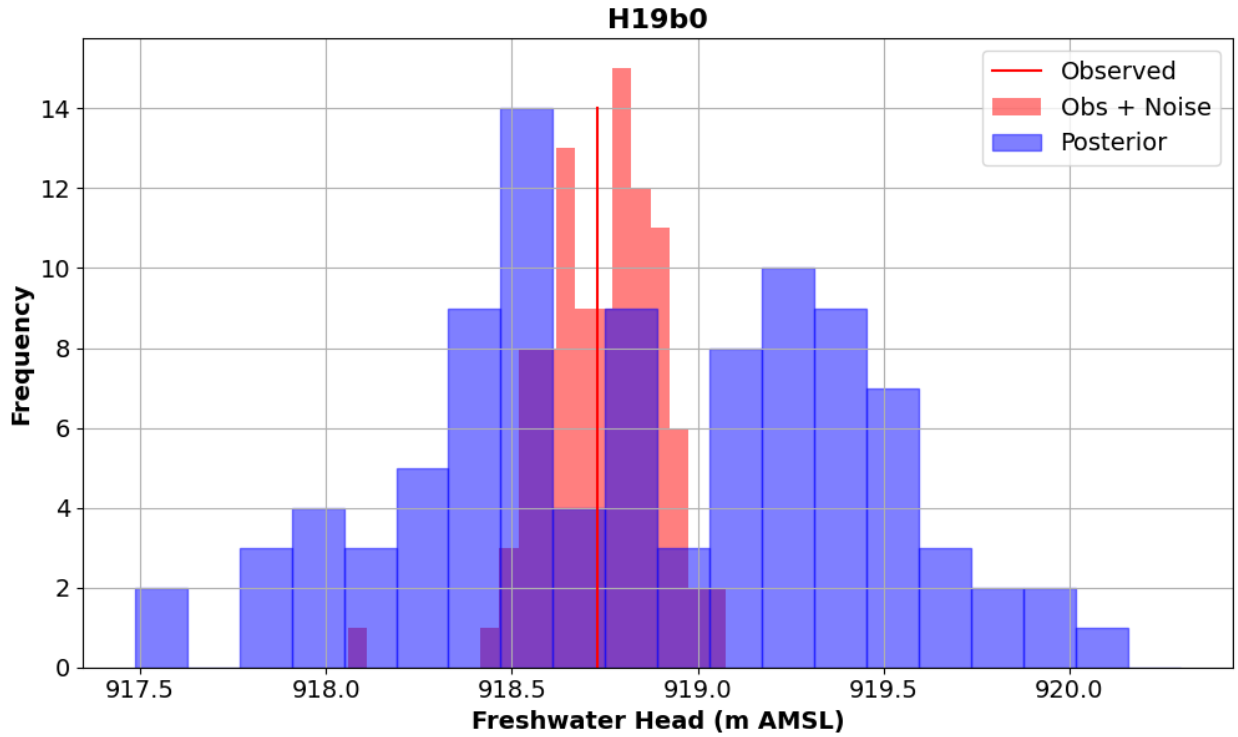


Figure TFIELD-38. Distributions of Observed and Model-Predicted Steady-state Freshwater Heads in H-19b0 for 100 Realizations at Iteration 5

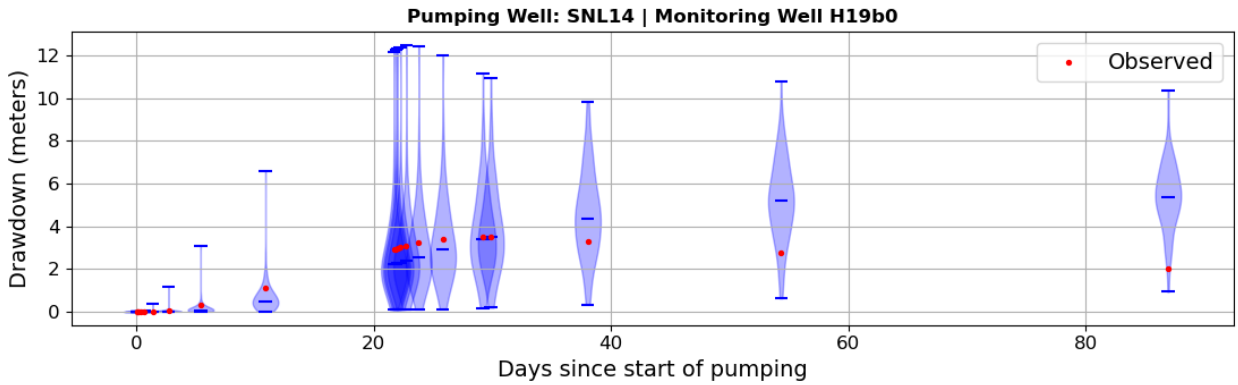


Figure TFIELD-39. Observed vs Simulated Drawdown at SNL-14 and H-19b0 Monitoring Locations for the SNL-14 Multi-Well Pumping Test

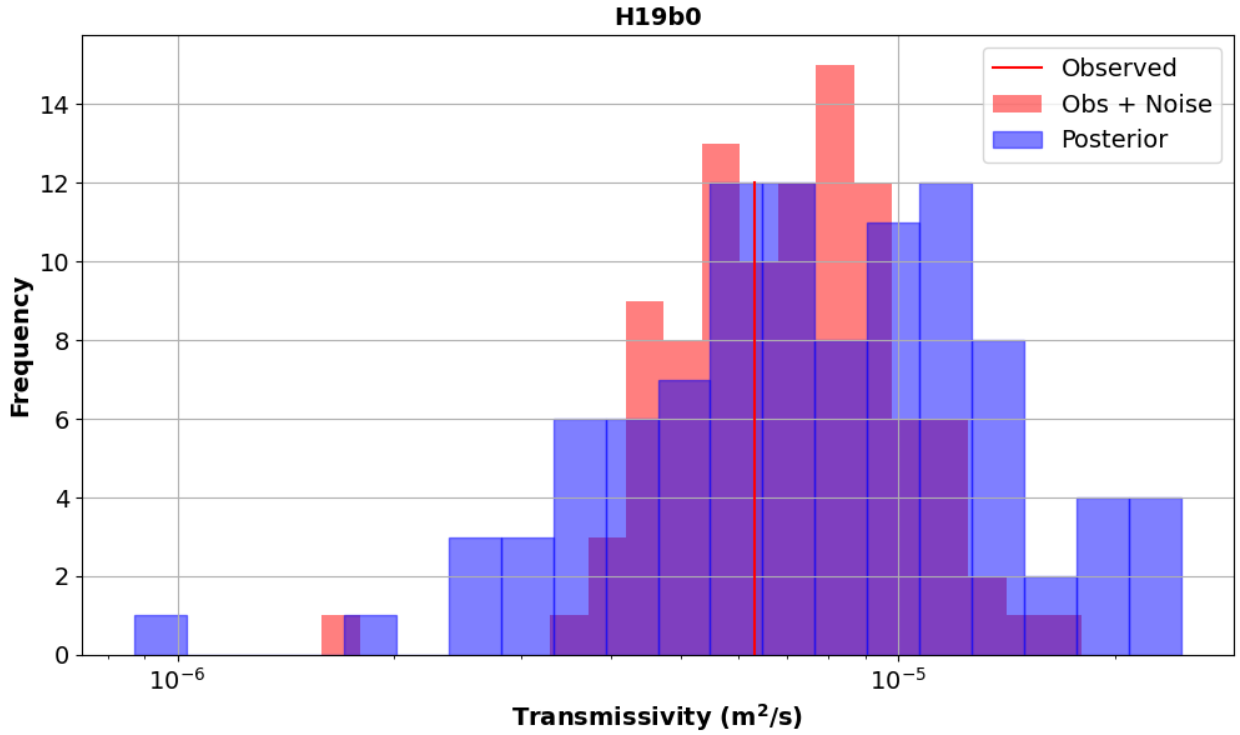


Figure TFIELD-40. Distribution of Single-Well Pumping Test Transmissivity Values in Model Element Containing H-19b0 for 100 Selected Realizations from Iteration 5

TFIELD-6.0 TFIELD Summary

Initial Culebra transmissivity fields were recalibrated to produce CRA-2026 T-fields. A linear-regression model for *T* provided an excellent match to equivalent freshwater heads. This model was used to create 973 stochastic realizations of the Culebra base T-fields in the vicinity of the WIPP site (Hart et al. 2009; DOE 2014), an improvement over the 200 developed for CRA-2014. A subset consisting of 100 optimal fields, of the 973 calibrated Culebra model realizations, were selected based on their ability to simulate these observed heads.

For the CRA-2026 T-fields recalibration, the same MF6 modeling domain used in CRA-2014 was used. This comprised a 30.7 kilometers (km) north-south by 28.4 km east-west domain, roughly centered on the WIPP site. The two-dimensional areal domain was discretized into 87,188 100 m x 100 m grid cells. An inactive portion at the northwest corner of the domain is delineated by a no-flow boundary along the axis of Nash Draw. The remaining boundaries are defined as constant head. The model uses a constant-head boundary along the low-permeability eastern edge of the domain. This condition represents the lithostatic pressure acting on the portion of the Culebra that is confined above and below by Rustler halite.

For CRA-2026, steady-state T-field recalibration was performed using probabilistic calibration targets derived from distributions of equivalent freshwater heads from 47 monitoring wells. This contrasts with CRA-2014, which used a single freshwater-head value for each well. Drawdown observations from 67 wells, generated by 10 planned pumping tests, served as

transient calibration targets. These include one more pumping test than was available for the CRA-2014 calibration. In addition to the planned pumping tests, the calibration included the opportunistic Mills Ranch pumping event. This event produced the strongest anthropogenic signal ever recorded in the Culebra monitoring network. Observations from 15 wells were used to form an additional transient calibration target.

The implementation of the transmissivity multiplier to represent potash mining impacts, along with the advective particle tracking analyses and subsequent radionuclide solute transport calculations, are presented and fully documented in Appendix PA of the CRA 2026.

TFIELD-7.0 References

(*Indicates a reference that has not been previously submitted.)

Beauheim, R. 1987a. Analysis of Pumping Tests of the Culebra Dolomite Conducted at the H-3 Hydropad at the Waste Isolation Pilot Plant (WIPP) Site, Carlsbad, NM: Sandia National Laboratories. SAND86-2311.

Beauheim, R. 1987b. Interpretation of the WIPP-13 Multipad Pumping Test of the Culebra Dolomite at the Waste Isolation Pilot Plant (WIPP) Site, Carlsbad, NM: Sandia National Laboratories. SAND87-2456.

Beauheim, R. and R. Holt. 1990. Geological and Hydrological Studies of Evaporites in the Northern Delaware Bains for the Waste Isolation Pilot Plant (WIPP). In D.W. Powers, R.M. Holt, R.L. Beauheim and N. Rempe, eds. Guidebook 14. Geological Society of America (Dallas Geological Society). pp.45-78.

Beauheim, R. 1989. Interpretation of H-11b4 Hydraulic Tests and the H-11 Multipad Pumping Test of the Culebra Dolomite at the Waste Isolation Pilot Plant (WIPP) Site, Carlsbad, NM: Sandia National Laboratories. SAND89-0536.

Beauheim, R. and G. Ruskauff. 1998. Analysis of Hydraulic Tests of the Culebra and Magenta Dolomites and Dewey Lake Redbeds Conducted at the Waste Isolation Pilot Plant Site, Carlsbad, NM: Sandia National Laboratories. SAND98-0049.

Bowman, D. 2014. Analysis of the H-9bR Pumping Test Conducted from 8/6/12 to 8/22/12, July 2, 2014, Carlsbad, NM: Sandia National Laboratories. ERMS 562291.*

Bowman, D. 2022. Analysis Plan for Evaluation and Recalibration of Culebra Transmissivity Fields, AP-203, Revision 0. December 6, 2022. Carlsbad, NM: Sandia National Laboratories. ERMS 578663.*

Bowman, D., R. Kushnereit, M. Pedrazas, P. Johnson, N. Deeds, and J. Pinkard. 2023. Analysis Report Documenting the Data, Generation, and Calibration of T-fields for CRA-2024. Carlsbad, NM: Sandia National Laboratories. ERMS 579507.*

Davies, P. 1989. Variable-Density Ground-Water Flow and Paleohydrology in the Waste Isolation Pilot Plant (WIPP) Region, Southeastern New Mexico. Open-File Report 88-490. Albuquerque: U.S. Geological Survey. ERMS 238854.

Doherty, J., 2025. Calibration and Uncertainty Analysis for Complex Environmental Models. Second Edition. Watermark Numerical Computing, Brisbane, Australia. ISBN:978-0-9943786-1-3.*

Farinacci, M. and D. Bowman. 2022. Analysis Report Documenting Water Level Analysis, Revision 1, Analysis Report for AP-150, Analysis Plan for the Analysis of Observed Water Level Fluctuations. September 2022, Carlsbad, NM: Sandia National Laboratories. ERMS 578343.*

Hart, D., R. Holt, and S. McKenna. 2008. Analysis report for Task 5 of AP-114: Generation of revised base transmissivity fields (pp. 122). Carlsbad, NM: Sandia National Laboratories. ERMS 549597.

Hart, D., Beauheim, R., and McKenna, S. 2009, Analysis report for Task 7 of AP-114: Calibration of Culebra transmissivity fields (pp. 187). Carlsbad, NM: Sandia National Laboratories. ERMS 552391.

Holt, R. 1997. Conceptual Model for Transport Processes in the Culebra Dolomite Member, Rustler Formation, Albuquerque, NM: Sandia National Laboratories. SAND97-0194.

Holt, R. and D. Powers. 1988. Facies Variability and Post-Depositional Alteration within the Rustler Formation in the Vicinity of the Waste Isolation Pilot Plant, Southeastern New Mexico. Carlsbad, NM: Department of Energy. WIPP-DOE-88-004.

Hughes, J., C. Langevin, and E. Banta. 2017. Documentation for the MODFLOW 6 framework: U.S. Geological Survey Techniques and Methods, book 6, chap. A57, 40 p., https://doi.org/10.3133/tm6A57.*

Jones, C. 1978. Test Drilling for Potash Resources: Waste Isolation Pilot Plant Site, Eddy County, New Mexico, Vols. 1 and 2, Open-File Report 78-592, U.S. Geological Survey, Denver, Colorado.

Kuhlman, K., and T. Corbet. 2017. WIPP Milestone Report: 2016 Culebra Groundwater Level Fluctuations. 2017. Sandia National Laboratories. ERMS 568172.*

Lang, W. 1935. Upper Permian formation of Delaware Basin of Texas and New Mexico. American Association of Petroleum Geologists Bulletin, Vol. 19, pp. 262-276.

Langevin, C., J. Hughes, E. Banta, R. Niswonger, S. Panday, and A. Provost. 2017. Documentation for the MODFLOW 6 Groundwater Flow Model. U.S. Geological Survey. Reston, VA. https://doi.org/10.3133/tm6A55.*

Mercer, J. 1983. Geohydrology of the Proposed Waste Isolation Pilot Plant Site, Los Medonos Area, Southeastern New Mexico. U.S. Geological Survey, Water-Resources Investigations Report 83-4016.

Powers, D. 2002a. Analysis report Task 1 of AP-088, Construction of geologic contour maps. Carlsbad, NM: Sandia National Laboratories. ERMS 522085.

Powers, D. 2002b. Addendum to Analysis Report, Task 1 of AP-088, Construction of Geologic Contour Maps. Carlsbad, NM: Sandia National Laboratories. ERMS 523886.

Powers, D. 2003. Addendum 2 to Analysis report Task 1 of AP-088, Construction of geologic contour maps. Carlsbad, NM: Sandia National Laboratories. ERMS 522085.

Powers, D. 2006. Analysis Report Task 1B of AP-114: Identify possible area of recharge to the Culebra west and south of WIPP. Carlsbad, NM: Sandia National Laboratories. ERMS 547094.

Powers, D. 2007. Analysis Report for Task 1A of AP-114: Refinement of Rustler Halite Margins Within the Culebra Modeling Domain. Carlsbad, NM: Sandia National Laboratories. ERMS 547559.

Powers, D. and R. Holt. 1995. Regional geological processes affecting Rustler hydrogeology. IT Corporation for Westinghouse Electric Corporation.

Powers, D. and R. Holt. 1999. The Los Medanos Member of the Permian Rustler Formation. New Mexico Geology. 21(4), pp.97-103.

Powers, D. and R. Holt. 2000. The salt that wasn't there: mudflat facies equivalents to halite of the Permian Rustler Formation, southeastern New Mexico. Journal of Sedimentary Research, 70(1), pp.29-36.

Powers, D., R. Holt, R. Beauheim, and S. McKenna. 2003. Geologic factors related to the transmissivity of the Culebra Dolomite Member, Permian Rustler Formation, Delaware Basin, southeastern New Mexico. In K.S. Johnson and J.T. Neal, eds. Evaporite Karst and engineering/environmental problems in the United States. 109th ed. Oklahoma Geological Survey. pp.211-18.

Powers, D., R. Holt, R. Beauheim, and R. Richardson. 2006, Advances in depositional models of the Permian Rustler Formation, southeastern New Mexico. In L. Land, V. W. Lueth, W. Raatz, P. Boston, & D. W. Love (Eds.), New Mexico geological society guidebook, 57th field conference, caves and karst of southeastern New Mexico. Albuquerque, NM: New Mexico Geological Society, pp. 267–276.

Powers, D. and D. Owsley. 2003. A Field Survey of Evaporite Karst Along NM 128 Realignment Routes. In K. Johnson and J. Neal, eds. Evaporite Karst and Engineering / Environmental Problems in the United States. 109th ed. Oklahoma Geological Survey. pp.233-40.

Roberts, R. 2006. Analysis Report for AP-070, Analysis of Culebra Pumping Tests Performed Between December 2003 and August 2005, Carlsbad, NM: Sandia National Laboratories. ERMS# 543901.

Roberts, R. 2007. Analysis Report for AP-070, Analysis of Culebra Hydraulic Tests Performed Between June 2006 and September 2007, Carlsbad, NM: Sandia National Laboratories. ERMS# 543901.

Scanlon, B., K. Keese, A. Flint, L. Flint, C. Gaye, W. Edmunds, and Il Simmers. 2006. Global synthesis of groundwater recharge in semiarid and arid regions: Hydrological Processes, v. 20, no. 15, p. 3335-3370, https://doi.org/10.1002/hyp.6335.

Theis, C. 1935. The relation between the lowering of the piezometric surface and the rate and duration of discharge of a well using groundwater storage, Am. Geophys. Union Trans., vol. 16, pp. 519-524.*

Thomas, M., K. Kuhlman, and A. Ward. 2017. Anthropogenic influences on groundwater in the vicinity of a long-lived radioactive waste repository. Hydrological Processes, 31(41):2637–2647.*

Toll, N. and P. Johnson. 2006a. Routine Calculations Report in Support of Task 6 of AP-114, SNL-14 August 2005 Pumping Test Observation Well Data Processing, Summary of Files, Carlsbad, NM: Sandia National Laboratories. ERMS# 543371.

Toll, N. and P. Johnson. 2006b. Routine Calculations Report in Support of Task 6 of AP-114, WIPP-11 February 2005 Pumping Test Observation Well Data Processing – Summary of Files, Carlsbad, NM: Sandia National Laboratories. ERMS# 543651.

Trabucchi, M., J. Carrera, and D. Fernàndez-Garcia. 2018. Generalizing Agarwal's method for the interpretation of recovery tests under non-ideal conditions. Water Resources Research, 54, 6393–6407. https://doi.org/10.1029/2018WR022684.*

U.S. Department of Energy (DOE). 2014. Title 40 CFR Part 191 Subparts B and C Compliance Recertification Application 2014 for the Waste Isolation Pilot Plant. Appendix TFIELD-2014, Transmissivity Fields. Carlsbad, NM: US Department of Energy Carlsbad Field Office.*

White, J. 2018. A model-independent iterative ensemble smoother for efficient history-matching and uncertainty quantification in very high dimensions. Environmental Modelling & Software, 109, 191-201.*

White, J., R. Hunt, M. Fienen, and J. Doherty. 2020. Approaches to Highly Parameterized Inversion: PEST++ Version 5, a Software Suite for Parameter Estimation, Uncertainty Analysis, Management Optimization and Sensitivity Analysis: U.S. Geological Survey Techniques and Methods 7C26, 52 p.*

Yoo, A., M. Jette, and M. Grondona. 2003. SLURM: Simple Linux Utility for Resource Management. In Job Scheduling Strategies for Parallel Processing (LNCS 2862, pp. 44–60). Springer. DOI: $\mathbf{10.1007/10968987_3}$.*